MASARYK UNIVERSITY
FACULTY OF SCIENCE
DEPARTMENT OF CONDENSED MATTER PHYSICS

INSTITUTE OF PHYSICS OF MATERIALS
ACADEMY OF SCIENCES
OF THE CZECH REPUBLIC

PH.D. DISSERATION:

DISLOCATION MOTION IN THREE-DIMENSIONAL PRECIPITATED CRYSTALS

TOMÁŠ ZÁLEŽÁK

BRNO, 2012

SUPERVISOR: ANTONÍN DLOUHÝ

Bibliographic Entry

Author	Mgr. Tomáš Záležák Faculty of Science, Masaryk University Department of Condensed Matter Physics
Title of Disseration	Motion of dislocations in a 3D crystal with precipitates
Degree Programme	Physics
Field of Study	Condensed Matter Physics
Supervisor	prof. RNDr. Antonín Dlouhý, CSc. Academy of Sciences of the Czech Republic Institute of Physics of Materials
Academic Year	2008/2012
Number of Pages	140
Keywords	discrete dislocation dynamics, high temperature plasticity

Bibliografický záznam

Autor	Mgr. Tomáš Záležák Přírodovědecká fakulta, Masarykova univerzita Ústav fyziky kondenzovaných látek
Název práce	Pohyb dislokací v třírozměrném krystalu s precipitáty
Studijní program	Fyzika
Studijní obor	Fyzika kondenzovaných látek
Školitel	prof. RNDr. Antonín Dlouhý, CSc. Akademie věd České republiky Ústav fyziky materiálů
Akademický rok	2008/2012
Počet stran	140
Klíčová slova	diskrétní dislokační dynamika, vysokoteplotní deformace

Abstract

This Ph.D. dissertation presents a 3D discrete dislocation dynamics model (DDD). The model describes a dislocation motion in crystalline materials containing secondary phases (precipitates) at high temperatures.

The model is based upon the linear theory of elasticity, which is used to calculate internal stress fields produced by the dislocation structure, which is represented by a set of short straight segments. This approach simplifies the calculation of the internal stress. Together with externally applied stresses, the internal stress gives rise to Peach-Koehler (driving) forces, which cause the displacement of the dislocations. The equations of the dislocation velocity account for the crystallography of the material. The model also comprehends an interaction between dislocations and incoherent rigid spherical precipitates.

The work briefly reviews mechanisms of high temperature plasticity and the role of crystal defects during plastic deformation. Further is discussed the knowledge of the theory of elasticity and the theory of dislocations necessary for the introduction of the 3D DDD model. The description of the model includes several techniques for time integration, relations between the driving forces and dislocation velocities, dynamic adjustment of the discretisation, discrete representation of the annihilation of smooth dislocation curves and symmetry optimizations. The function of the model is demonstrated on several benchmark systems: dislocation loop contraction and expansion with precipitates (2D), Frank-Read dislocation source (2D) and a contracting or expanding set of coaxial dislocation loops in a field of precipitates (3D).

Finally, the 3D DDD model is used to study an evolution of a low-angle tilt boundary (LATB) and its interaction with a field of rigid spherical precipitates under the action of applied shear stress. The simulation is carried out with different velocity equations and the results are compared. The results suggest that the motion of the LATB may be completely stopped by the precipitates, which thus strengthen the material. Further a parametric study is calculated to determine the critical applied shear stress necessary for the LATB to pass through the precipitate field. The calculation is done for varying misorientation angles of the LATB and also for a wide range of applied shear stresses. The results suggest that the critical applied shear stress is approximately inverse proportional to initial line spacing in the LATB, i.e. it is proportional to the misorientation angle. The resulting critical applied shear stress is also several times lower than the Orowan stress for matching particle diameters and interparticle spacings.

The results of the 3D DDD study of the LATB are compared with available results from creep tests of precipitate strengthened alloys. These experiments indicate existence of critical stresses of comparable magnitude for corresponding misorientation angles. Also the critical stresses obtained from the experiments are significantly lower than appropriate Orowan stress.

Abstrakt

Tato disertační práce popisuje 3D model diskrétní dislokační dynamiky (DDD). Model popisuje pohyb dislokací za vysokých teplot v krystalických materiálech obsahujících sekundární fáze (precipitáty).

Model je založen na lineární teorii elasticity, jež umožňuje vypočítat vnitřní napěťová pole vytvořená dislokační strukturou vyjádřenou pomocí souboru krátkých úseček. Tento postup zjednodušuje výpočet vnitřního napětí. Vnitřní a vnější aplikovaná napětí vyvolávají hnací (Peach-Koehlerovy) síly, které zapříčiňují pohyb dislokací. Rovnice popisující rychlost dislokací zahrnují krystalografii materiálu. Součástí modelu je též působení mezi dislokacemi a nekoherentními tuhými kulovými precipitáty.

Práce ve stručnosti shrnuje mechanismy vysokoteplotní deformace a úlohu krystalových poruch při plastické deformaci. Dále jsou rozebrány poznatky z teorie elasticity a teorie dislokací potřebné k zavedení 3D modelu DDD. Popis modelu zahrnuje různé způsoby časové integrace, vztahy mezi hnacími silami a rychlostmi dislokací, průběžnou úpravu diskretizace, diskrétní vyjádření anihilace hladkých dislokačních křivek a optimalizace založené na souměrnosti. Činnost modelu je předvedena na několika zkušebních soustavách: smršťující se a rozpínající se dislokační smyčka s precipitáty (2D), Frankův-Readův zdroj dislokací (2D) a smršťující se či rozpínající se řada souosých dislokačních smyček v poli precipitátů (3D).

Nakonec je s využitím 3D modelu DDD zkoumán vývoj maloúhlové sklonové hranice a její interakce s polem tuhých kulových precipitátů při aplikaci smykového napětí. Simulace je provedena s různými rovnicemi pro rychlost dislokací, jednotlivé výsledky jsou porovnány. Výsledky ukazují, že pohyb hranice mohou precipitáty zcela zastavit, čímž zpevňují materiál. Dále byla provedena parametrická studie určující kritické aplikované smykové napětí potřebné k tomu, aby hranice překonala pole precipitátů. Výpočet je proveden pro různé misorientační úhly sklonové hranice, jakož i pro široké rozpětí aplikovaných smykových napětí. Výsledky ukazují, že kritické aplikované smykové napětí je nepřímo úměrné počátečním rozestupům mezi dislokacemi tvořícími hranici, tj. je úměrné úhlu misorientace. Výsledné kritické aplikované smykové napětí je rovněž několikrát nižší než Orowanovo napětí odpovídající zvolené velikosti precipitátů a jejich rozestupům.

Výsledky 3D DDD studie maloúhlové sklonové hranice jsou porovnány s dostupnými výsledky creepových zkoušek precipitačně zpevněných slitin. Tyto zkoušky vykazují kritické napětí obdobné velikosti při obdobných úhlech misorientace. Rovněž kritické napětí při zkouškách je podstatně nižší než odpovídající Orowanovo napětí.

Acknowledgement

I would like to acknowledge prof. RNDr. Antonín Dlouhý, CSc., for a plenty of suggestions, advices and recommendations during my work, as well as for inspiring comments to the final text of this dissertation.

Tomáš Záležák

I declare that I have elaboreted this work on my own and that I have used only the literature listed on pages 125–128.

Tomáš Záležák

CONTENTS

I. INTRODUCTION

Many materials with a potential for industrial applications have a crystalline structure and most of them are metals and their alloys. A research focused on a relation between material structure and properties is very important for contemporary industry. A particularly important field of the materials science is an investigation of material behaviour at extreme conditions, such as mechanical loadings at high temperatures. These conditions activate high temperature plastic deformation, e.g. *creep* [1, 2], which is one of the important processes with a great impact on the lifetime of industrial structures. The creep behaviour of various metallic materials is thus being investigated over decades [3–5].

Plastic deformations of metals have been studied since the 19th century [6]. Many of their properties were not understood, such as a critical strength of a perfect crystal [6]. A concept of dislocations explained a discrepancy between a theoretical prediction of critical shear stresses and experimental measurements. Among other crystal imperfections, the dislocations are known to be responsible for many aspects of plastic deformation [1, 6]. With the progress of computer technology in last decades, the research in materials science is supported also by numerical calculations like discrete dislocation dynamics (DDD), which is a central topic of this work.

I.1 High temperature deformation

A solid responses to an externally applied force by its deformation. The deformation can be elastic, anelastic or plastic. The elastic deformation is reversible and does not depend on time. It is described by a linear theory of elasticity [7, 8]. The anelastic deformation is also reversible, but time-dependent [1]. Finally, the plastic deformation is irreversible and generally depends on time. The plastic deformation can be decomposed into a time-independent part and a time-dependent part, which is creep [1, 2].

The deformation can be recorded during a high temperature loading. A plot of the deformation vs. time for a creep process is known as a *creep curve*. A schematic creep curve is shown in Fig. I.1. The first part of creep deformation is a *primary creep*. The strain rate decreases during the primary creep, until it approaches a constant value. For low homologous temperatures[1], only the primary creep occurs. Higher homologous temperatures activate recovery processes which relax the strain hardening and help establishing the *secondary creep*. The secondary creep features a constant strain rate, so the creep curve is linear. Finally, a *tertiary creep* may follow, which exhibits an increase of strain rate with time. This may be caused by an increase of the applied stress or by changes in the material structure. The tertiary creep is terminated by a fracture of the material [1, 2].

In a typical creep experiment, a specimen is inserted in a creep machine, which may be pulling or compressing the gauge length region of the specimen. The test is performed at constant temperature. The specimen loading regime may be either the constant load (i. e. the force acting upon the specimen is constant), or the constant applied stress ($\sigma = \text{const.}$) when the acting force changes according to the changing specimen

[1] A homologous temperature T/T_m is a ratio of a thermodynamic temperature T and a temperature of melting T_m.

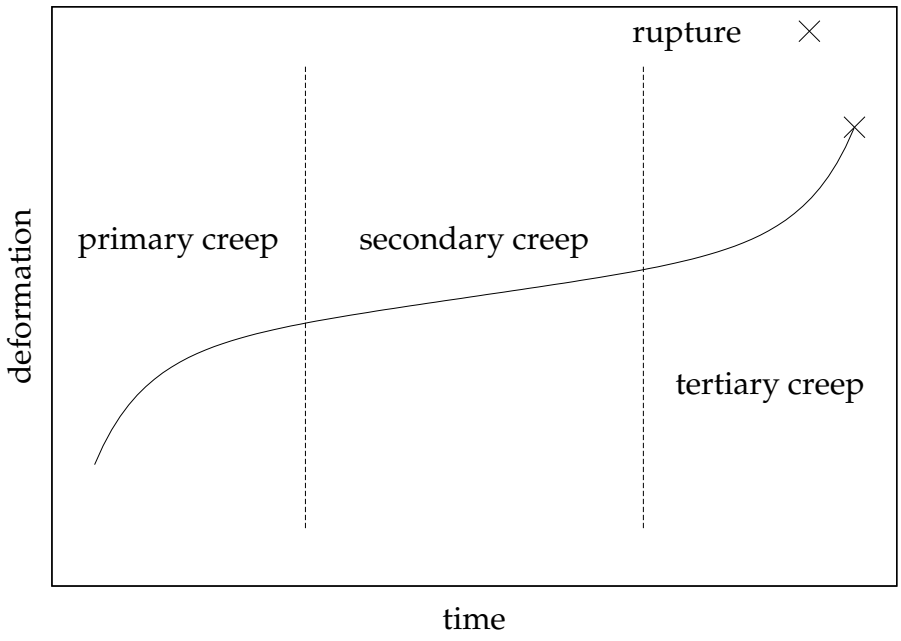

Figure I.1: A schematic creep curve represented as strain vs. time plot, see also [1].

cross-section. The deformation of the specimen is recorded during the test. As an example, results of a creep test of an austenitic steel $16\text{Cr} - 12\text{Ni} - 2.5\text{Mo}$ at a temperature $T = 873$ K are presented in Fig. I.2.

As the cross-section of the specimen decreases, a constant load applied upon the sample raises the stress, which leads to an increase of the strain rate, and finally to a crack of the material. On the other hand, a test with a constant stress may take very long time till fracture (see Fig. I.2 – curve b).

I.1.1 Microstructural mechanisms

The rate of high temperature deformation is strongly sensitive to temperature. One of the most important mechanisms involved in plastic deformation is a motion of dislocations. A thermal activation of dislocation motion can be represented using a framework of the rate of chemical reactions, so a similar thermodynamic description can be adopted [9, 10]. The dislocation motion is impeded by obstacles, which either produce a long-range stress field, such as other dislocations, precipitates etc., or produce a short-range stress field. A critical stress $\sigma_{\text{crit.}}$ needed to move the dislocations during the plastic deformation can be decomposed into a long-range part σ_{LR} and a short-range part σ_{SR}:

$$\sigma_{\text{crit.}} = \sigma_{\text{LR}} + \sigma_{\text{SR}}. \tag{I.1}$$

While the long-range contribution σ_{LR} does not much depend on the temperature (considering that e.g. the shear modulus μ is just slightly temperature dependent) [11], the short-range interaction between dislocations and obstacles located in the slip plane characterized by σ_{SR} may be influenced by a lattice thermal energy [12,13]. If there is enough energy from a local thermal fluctuation, the local stress supported by the thermal activation may release a dislocation segment from local obstacles [14, 15]. Calculations based

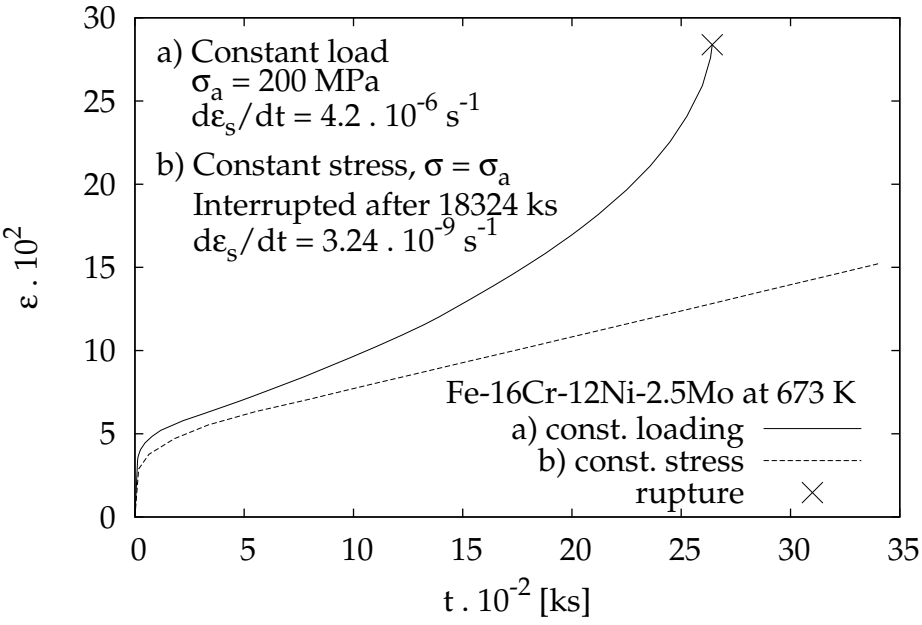

Figure I.2: A comparison of creep curves of an austenitic steel $16\mathrm{Cr} - 12\mathrm{Ni} - 2.5\mathrm{Mo}$ at a temperature $T = 873$ K for a) a constant loading with initial stress $\sigma_a = 200$ MPa and b) for a constant stress $\sigma = \sigma_a$. The plot comes from [1].

on thermodynamics suggest that the local stress field contributing to the release of the dislocation segment comes only from a portion of the externally applied stress – an *effective stress* σ^*, whereas the rest of the applied stress counterbalances the local stresses originating outside of the subsystem formed by the dislocation segment and a short-range obstacle. This part of the applied stress has been called *internal stress* σ_i by Seeger et al. [9]. The linear elasticity allows to sum all long-range stress fields (from other dislocations, coherent particles etc. [10]) and thus get internal stress at a certain position in the microstructure. Apart from the internal and effective stress, the analysis of a thermally activated dislocation motion gave rise to other thermodynamic and kinetic quantities of the process, i.e. the *activation volume* V^*, the *energy barrier* ΔG_0 connected with the short-range obstacle at zero effective stress and the *mobile dislocation density* ρ_m [14].

The mobility of dislocations may also depend on processes modifying a dislocation core [16, 17]. Some crystalline materials thus show a non-monotonous dependence of the flow stress on temperature for homologous temperatures from 0.3 to 0.5 [18]. A very weak temperature dependence of the flow stress leads to an athermal flow [18], which may be explained by the temperature dependence of the elastic constants. This is either due to the complicated structure of the dislocation core, which can split into non-planar configurations [17], or due to the short-range diffusion enriching the dislocation core by impurity atoms, which markedly change the dislocation mobility [19, 20]. A bulk diffusion controls processes that dominate at homologous temperatures above 0.4, where the high temperature creep sets in [1]. A vacancy diffusion, which controls the dislocation climb, can result in a recovery and annihilation of dislocations fast enough to balance hardening processes. This balance may result in a steady rate of the macroscopic deformation [1]. The internal stress distribution during the steady state creep has been discussed thoroughly in the literature (e. g. [1]).

I.1.2 Phenomenological description

The strain rate during the creep deformation is a function of temperature T and the applied stress σ [1,2,11].

$$\dot{\varepsilon} = f(\sigma, T). \tag{I.2}$$

The experiments suggest, that the minimum strain rate $\dot{\varepsilon}_{\min}$, which corresponds to the secondary creep stage [1], may be approximated by a Norton's law [2,21]:

$$\dot{\varepsilon}_{\min} = B(T)\sigma^n, \tag{I.3}$$

where $B(T)$ is a temperature-dependent parameter and n is a stress exponent. Parameters B and n are material characteristics.

The influence of the temperature on the creep process is very strong. The creep rate and its dependence on temperature can be described by the Arrhenius law [1]:

$$\dot{\varepsilon} = \dot{\varepsilon}_0 \exp\left(-\frac{Q_c}{RT}\right), \tag{I.4}$$

where $\dot{\varepsilon}_0$ is a frequency factor, Q_c is the apparent activation energy of creep and R is a gas constant. To fulfil both equations (I.3) and (I.4), the prefactor $B(T)$ must be determined by the exponential function of the creep activation energy and the temperature:

$$B(T) = B_0 \exp\left(-\frac{Q_c}{RT}\right). \tag{I.5}$$

I.1.3 Sensitivity to the applied stress

According to [1], we may introduce the sensitivity parameter of the creep rate to the applied stress (stress sensitivity parameter) as:

$$n = \left.\frac{\partial \log \dot{\varepsilon}_{\min}}{\partial \log \sigma}\right|_T. \tag{I.6}$$

For a case of a diffusion creep of pure metals, the stress exponent is $n = 1$, whereas for the dislocation creep of pure metals and class II alloys is $n = 5$ [1,2]. The class I alloys usually exhibit $n = 3$ [2,22]. On the other hand, precipitation strengthened alloys, such as $\mathrm{Ni} - 20\mathrm{Cr} - 2\mathrm{ThO_2}$ [4], may be characterised by much higher value of the sensitivity parameter ($n > 10$, or even $n > 20$). The experimental results suggest, that there is a threshold stress σ_t, which has to be exceeded to activate the creep process in certain type of particle strengthened materials. As indicated by TEM micrographs [3], the precipitates are holding the dislocations and preventing them from further propagation. The dislocations are thus driven by an effective force proportional to $\sigma - \sigma_t$ [4], which is very low just above the threshold stress. This causes the high values of the stress sensitivity parameter n.

I.1.4 Activation processes

As it was already mentioned in the section I.1.1, the local obstacles are overcome with a help of a thermal energy. This is called a *thermally activated motion of dislocations*, which, under certain circumstances, may control the whole deformation process [11]. A typical set of elementary deformation processes than can be thermally activated consists of:

1. *Intersecting the dislocation forest.* Dislocations intersecting the active slip plane are called a *dislocation forest*. The activation volume depends on the density of the dislocation forest. Increasing the dislocation forest density increases the σ_{SR} and decreases the activation volume.
2. *An interaction between dislocations and point defects.* The activation volume depends on the concentration of point defects (including the impurity atoms).
3. *Climbing of edge dislocations.* The activation volume is approximately b^3 (b is the length of the Burgers vector, see sections I.2 and IV.1) and the activation energy is determined by the activation energy of self-diffusion.
4. *A cross-slip* of screw dislocations.
5. *Overcoming the Peirls-Nabarro stress.*
6. *Non-conservative motion of screw dislocations with jogs.*

I.2 Crystal defects

Most crystalline materials are not perfect single crystals, neither are they polycrystals consisting of perfect single crystalline grains. The crystal lattice in vast majority of cases contains many different defects. These defects have a considerable impact on various properties of the material, such as the thermal and electric conductivity or mechanical properties. Depending on the dimension, the crystal defects can be divided into four categories: *point*, *line*, *planar* and *bulk* defects. The defects are thoroughly described in the literature [11, 23], here only a short overview is presented.

I.2.1 Point defects

Several examples of point defects in a simple cubic lattice are displayed in a 2D projection in Fig. I.3. The lattice site may be unoccupied (*vacancy* – Fig. I.3a) or occupied by an impurity atom (*substitution* – Fig. I.3c). If there is an atom outside of a lattice site, it is an *interstitial* (Fig. I.3b), or, in a case of an impurity atom, an *interstitial impurity* (Fig. I.3d). A more complex types are formed by the combinations of the former, such as a *Frenkel pair* (vacancy + interstitial, Fig. I.3e), vacancy + substitution with impurity atom (Fig. I.3f) or multiple adjacent vacancies (not displayed).

The impurity atoms occupy a different volume than the atoms of the host crystal lattice, which leads to interaction with dislocations by a local modulation of stress field (section I.3.1). The interstitials and vacancies also take part in diffusion, especially at elevated temperatures (sections I.3.4 and IV.5).

I.2.2 Line defects

The most important line defects are *dislocations*. This means that the crystal lattice is misaligned along a continuous line within a short distance (up to several interatomic distances). On the other hand, the dislocation length may even be comparable to the size of the crystal.

An example of a dislocation is in Fig. I.4. The Fig. I.4a shows a cut through simple cubic lattice without any defect, which is represented by a perfect 2D lattice. If there is a

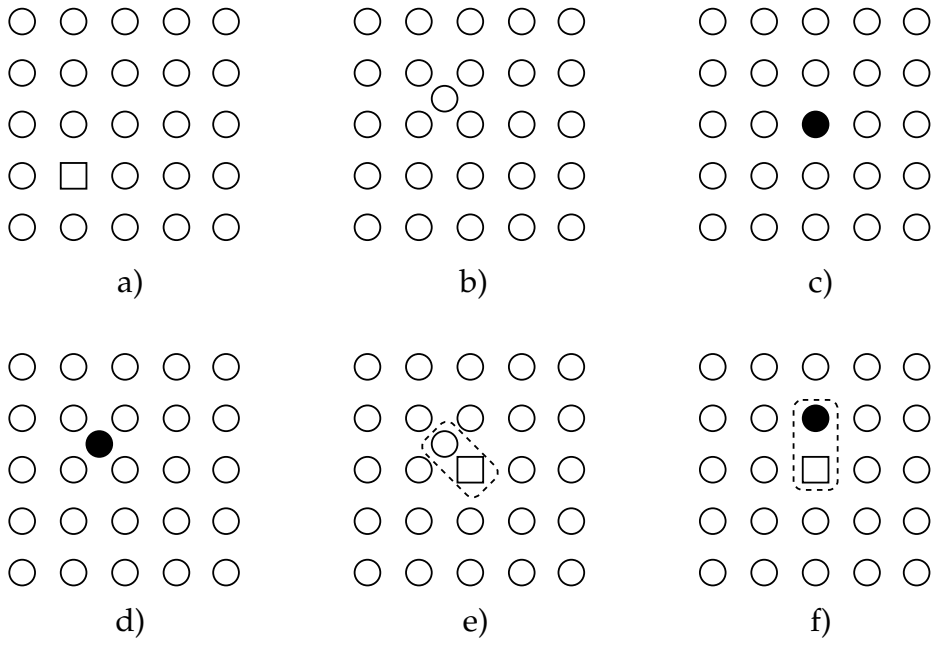

Figure I.3: Point defects in a simple cubic lattice: a) vacancy, b) interstitial, c) substitution impurity atom, d) interstitial impurity, e) Frenkel pair, f) vacancy + impurity.

half plane inserted to or removed from the crystal, the local lattice structure substantially changes. Near the edge of the plane, the crystal lattice is strongly misaligned. In the upper region, where the plane is inserted, the atoms are compressed to each other, while in the lower region the atoms move apart from each other. This kind of defect is called an *edge dislocation*, which is actually the edge of the half plane inserted into the crystal. The edge dislocation is schematically depicted as a T-like symbol: $\perp\top\vdash\dashv$, where the T stem denotes the inserted plane and the T bar the glide plane. To characterize a dislocation, we introduce two parameters, the *Burgers vector* $\boldsymbol{b}$ and a unit vector $\boldsymbol{\xi}$, which, in a given point, is tangential to the dislocation line. In Fig. I.4, we choose the direction vector $\boldsymbol{\xi}$ along the Z axis (pointing into the paper).

In order to define the Burgers vector, we start with a crystal containing an edge dislocation (Fig. I.5a). We take a circuit about the edge dislocation in a right hand sense, the thumb points in the dislocation direction vector $\boldsymbol{\xi}$ and the fingers show the circuit orientation. We start at the position S and proceed through the positions 1, 2 and 3 to the final position F, which, in the deformed crystal, coincides with the starting position S. If we take the circuit only through the lattice sites, we can represent the circuit $S123F$ as a sequence of steps: $\uparrow\uparrow\uparrow\uparrow\rightarrow\rightarrow\rightarrow\rightarrow\downarrow\downarrow\downarrow\downarrow\leftarrow\leftarrow\leftarrow$. Now we follow these steps in the perfect lattice of the same crystal (Fig. I.5b). As we can see, the circuit does not close, as the points F and S do not overlap. In order to close the circuit, we need additional step $\leftarrow$ – the *true Burgers vector* $\boldsymbol{b}$ pointing from the endpoint point F to the starting point S. This definition of the Burgers vector is called *finish-start right-hand* convention (FS/RH) [6]. This definition of $\boldsymbol{b}$ is adopted throughout this thesis. In the literature, sometimes, a different definition is used, where the Burgers vector points from S to F, from the start to finish (SF/RH), which obviously results in an opposite direction of the Burgers vector. From the FS/RH definition also follows, that the choice of the direction of the vector $\boldsymbol{\xi}$

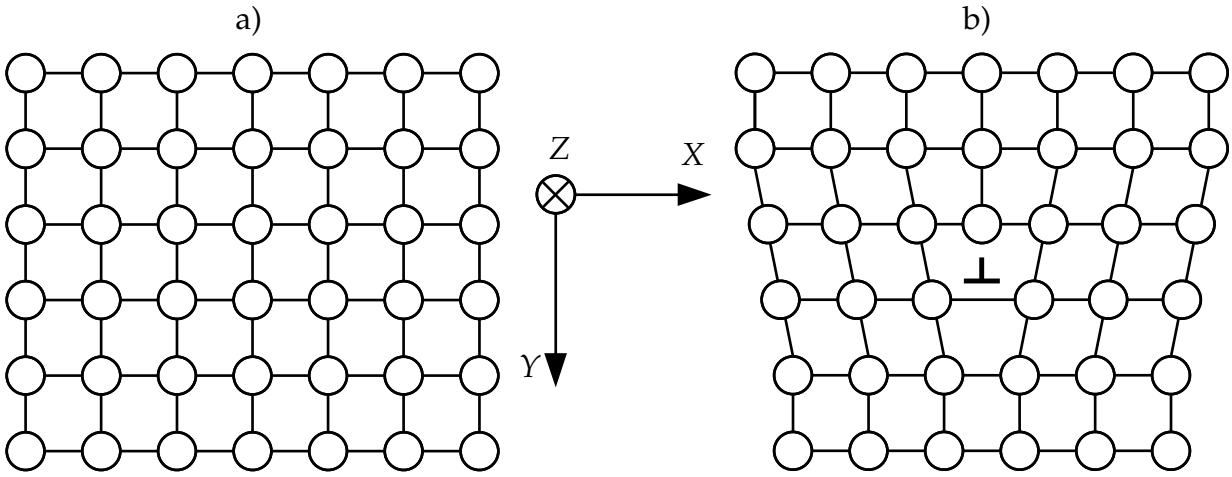

Figure I.4: A cut through a simple cubic lattice: a) without any defect, b) with an edge dislocation.

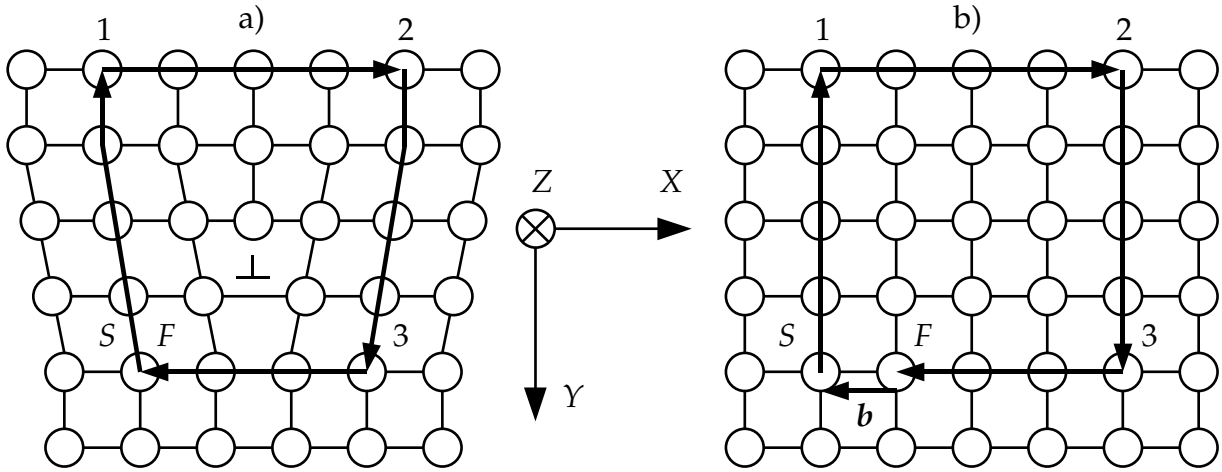

Figure I.5: Definition of the true Burgers vector (FS/RH convention).

determines the circuit sense. An inversion of $\boldsymbol{\xi}$ thus inverts also the Burgers vector $\boldsymbol{b}$.

A complementary type of dislocation is a screw dislocation. In the case of screw dislocation, there is no inserted plane in the crystal, instead, the crystal is cut a half way through by a plane and sheared parallel to the cut edge by at least one atomic distance. The situation is depicted in Fig. I.6. Again, the dislocation direction is along the Z axis. If we apply the FS/RH scheme, we get a circuit $S12345F$, whose steps are $\downarrow\leftarrow\leftarrow\leftarrow\uparrow\uparrow\rightarrow\rightarrow\rightarrow\downarrow\ \odot$. Again, if we undergo the same steps in a perfect crystal, the circuit will be closed by adding one more step $\otimes$. The Burgers vector $\boldsymbol{b}$ has a positive Z direction, which is the same direction as the dislocation line direction $\boldsymbol{\xi}$. The screw dislocations are depicted by symbols $\odot$ or $\otimes$.

The edge dislocations thus have the Burgers vector perpendicular to their direction ($\boldsymbol{b}\ \perp\ \boldsymbol{\xi}$), whereas the screw dislocations have the Burgers vector parallel to their direction ($\boldsymbol{b}\ \parallel\ \boldsymbol{\xi}$). There are also dislocations with a mixed character, which have an edge component and a screw component and the angle between the $\boldsymbol{b}$ and $\boldsymbol{\xi}$ vectors falls into a range $(0, \pi/2)$.

The dislocations are very important for explaining the material properties of crys-

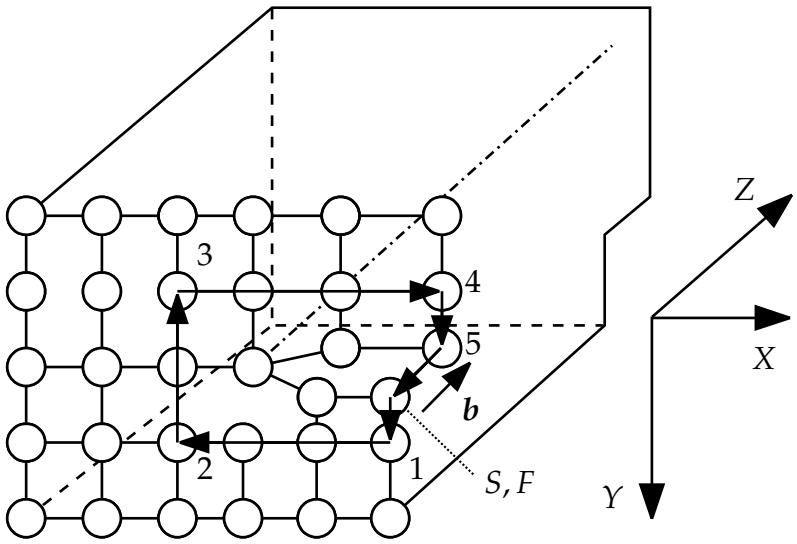

Figure I.6: A simple cubic crystal with a screw dislocation.

talline materials [6]. For example, the theoretical shear stress necessary to initiate plastic flow in the crystal was estimated as

$$\sigma_{\text{theor.}} = \frac{\mu b}{2\pi d} \simeq \frac{\mu}{5}, \tag{I.7}$$

where $b = |\boldsymbol{b}|$ is the magnitude of the Burgers vector and d is the interplanar spacing [6]. However, the experimentally obtained values were from a range from 10^{-4} to $10^{-5}\mu$ for many materials (the μ denotes a shear modulus). While the theoretical values correspond to experimental results obtained for perfect whisker crystals, the results for other materials were finally explained by the dislocation motion [6]. The dislocations can move due to driving forces coming from the stress field in the material. The stress field generally consists of a contribution from the dislocation itself and from other sources external to the dislocation, like other dislocations in the crystal and an external stress applied on the material.

I.2.3 Planar defects

The planar defects are grain and subgrain boundaries. A special case of the latter is a low angle dislocation boundary (LADB), which we will discuss at first.

Low-angle dislocation boundary

A LADB separates two regions of a material, a crystal lattices of which are only slightly misoriented. The slight misorientation is formed by a row of dislocations forming together a wall structure. An example of such structure is in Fig. I.7a, which depicts a *tilt boundary*, consisting of edge dislocations. In both regions adjacent to the boundary, the crystal lattice is tilted by angle $\Theta/2$. This angle Θ can be estimated by a ratio of the length of the Burgers vector b and the inter-dislocation distance h:

$$\frac{b}{h} = 2\sin\frac{\Theta}{2} \approx \Theta. \tag{I.8}$$

These LADBs were experimentally observed in many materials including precipitation hardened alloys [3, 24]. The low-angle dislocation boundaries migrate during a high temperature loading [25].

If the two subgrains are twisted with respect to each other, the dislocations forming the boundary are of a screw character and form a *twist boundary*. This structure has also been described in literature [11].

Grain boundary

If the misorientation between the two adjacent crystal lattices is above approx. 20 to 25°, the overall structure is far from a perfect crystal and a description different from discrete dislocations must be adopted for its characterization [6]. Methods based on *coincidence site lattices* model are applied [11]. An example of such structure is shown in Fig. I.7b.

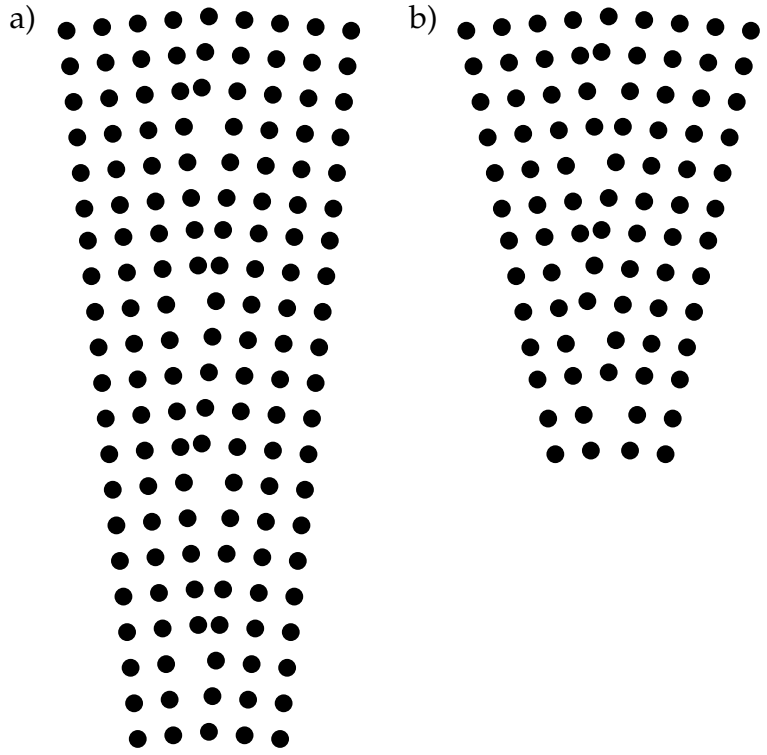

Figure I.7: Tilt boundaries with misorientation angle approx. a) 11.5° and b) 23°.

I.2.4 Bulk defects

An example of such a defect is a large cluster (relative to the atomic scale, i.e. microscopic) of vacancies, which is called a *void*. Another case is a *precipitate* or *particle of secondary phase*, which differs by its structure and chemical composition from the rest of the bulk material. It can be described as a large cluster of impurity atoms.

I.3 Dislocation structures at high temperatures

The dislocation structures in alloys and composite materials subjected to loadings at high temperatures undergo complex interactions with impurity atoms, grain boundaries and secondary phases. These interactions have a considerable impact on the high temperature strength of the material.

I.3.1 Impurity atoms

Impurity atoms (solute) may have a different size than the atoms forming the primary phase (solvent). In the case of edge dislocations, the crystal lattice near the dislocation consists of a compressed region (where an extra half-plane of atoms is inserted) and a dilated region (under the inserted half-plane). Depending on the atomic radius, the impurity atoms may diffuse into the compressed (for smaller atoms) or dilated (for larger atoms) regions.

Even the impurity atoms having the same size as the atoms of the solvent phase affect the dislocations. These atoms may have stronger or weaker chemical bonds with the neighbouring atoms, making thus the crystal locally harder or softer. These local variations of mechanic properties affect the dislocation interactions, specially the forces needed for dislocations to pass through the affected region [11].

I.3.2 Grain hardening

The material strength depends also on the grain size. In contrast to monocrystals, the motion of dislocations in polycrystals is considerably limited by grain boundaries. A boundary between two grains with almost the same orientation (misorientation about 1°) is formed by a dislocation wall consisting of a row of dislocations. Higher misorientation angles lead to a considerably different boundary structure; the grain boundary is then formed by several atomic layers exhibiting less regular distribution of atoms. In both cases, the boundary is an obstacle for the moving dislocations, which may form pileups at the boundaries.

The study performed with bicrystals showed that the grain boundary orientation strongly influences the flow stress [11]. For a boundary orientation parallel to the loading direction, the flow stress is determined by the grain misorientation. Particularly, greater misorientation angles increase the flow stress [11].

In polycrystals with grain boundaries perpendicular to the loading direction, the deformation starts in grains with the most suitable orientation of the slip systems with respect to the loading direction, but the dislocation activity is not observed near the grain boundaries [11].

The macroscopic plastic deformation of a polycrystalline material starts only when the dislocation pileups at a grain boundary activate dislocation sources in the neighbouring grains by their stress fields. [11].

I.3.3 Precipitation hardening

An addition of impurity atoms generally increases the flow stress. Moreover, in a supersaturated solid solution precipitation of secondary phases may occur. Depending on

the lattice parameters of the precipitate and the matrix, the precipitates may be *coherent*, *semicoherent* or *incoherent*.

The coherent precipitates increase the flow stress due to a) exertion of forces caused by a lattice constant difference, b) formation of an antiphase boundary, c) a difference between stacking fault energies in the precipitate and in the matrix, d) an increase of the surface of the precipitate after being cut by a migrating dislocation.

If the coherent precipitates make the flow stress too high, or if the precipitates are incoherent, the dislocations cannot pass through the particle volume. However, a further motion of the dislocations is possible due to an *Orowan mechanism* and climb past particles [26, 27]. The dislocations are initially pinned by the precipitates and bow out between the precipitates due to the applied stress. The rising curvature in the bow-out produces a stress with an opposite sign. If the applied loading is high enough, the bow-out may grow up to a critical configuration from which on the bow out proceeds by self-expansion. This process allows the side sections of the dislocation to annihilate, leaving a dislocation loop on the precipitate. This is called the *Orowan mechanism* and it is analogous to the mechanism of the Frank-Read source [11]. The critical stress necessary to overcome the precipitates depends on the distance between the particle centres λ and the particle diameter d

$$\sigma_{\text{Orowan}} = \Gamma \frac{\mu b}{\lambda - d}, \tag{I.9}$$

where the factor Γ is either predicted by a model ($\Gamma = \ln(d/R_0)/(2\pi)$ for edge dislocations, $\Gamma = \ln(d/R_0)/[2\pi(1-\nu)]$ for screw dislocations, [11]) or fitted from experimental data ($\Gamma = 0.8$, [28]).

I.3.4 Dynamic recovery

Dynamic recovery is a process, which compensates the strain hardening of the material, especially the increase of the dislocation density. If dislocations are produced by Frank-Read-type sources, the edge components of the loops, which originally move in distinct slip planes, undergo a diffusion controlled climb, which allows them to propagate into different slip planes. Dislocations of an opposite sign may thus climb to a common slip plane and annihilate. This process decreases the dislocation density. The screw components can move to a common slip plane either by a thermally activated cross-slip, or by a conservative motion of the dislocation jogs formed by climbing of the edge components of the loop [1].

Thus the dislocation density can reach a steady value given by an equilibrium between the generation and annihilation of dislocations. A consequence of the steady dislocation density is a steady deformation regime observed during the secondary creep, which exhibits a linear increase of the strain with time (Fig. I.1).

I.3.5 Formation of a dynamic equilibrium structure

The dislocations in an annealed crystal form mostly a 3D Frank network and partially also 2D networks consisting of low-angle dislocation boundaries. In the 3D networks, dislocations are connected in junctions – dislocation nodes. The stability condition of a node is that the sum of Burgers vectors of dislocations coming to and out of the junction

is zero. The condition allowing a formation of low-angle boundaries is a local outbalance of dislocations of one sign. The low-angle boundaries can be either tilt boundaries formed by climb and glide of edge dislocations or twist boundaries, which are formed by a glide of two systems of screw dislocations [1].

In annealed polycrystals, the dislocation structure is influenced also by the grain size and grain orientation. A multiaxial stress state in one particular grain may promote the activity of more slip systems. In some alloys the 2D networks may not be present at all, if there is a low stacking fault energy, which hinders the dislocation climb and cross slip [1].

The dislocation system formed immediately after an application of external stress usually has a cell structure, even after a deformation at room temperatures.

At the beginning of the primary creep, the dislocation structure becomes more heterogenous and the subgrains are gradually formed (in class II materials mainly). At the beginning of the secondary creep, the structure is partially homogenized and the mean subgrain size and the subgrain misorientation do not change much during subsequent stages of creep [1].

The development of the dislocation structure during primary creep is strongly dependent on the stacking fault energy. The system of subgrain boundaries weakens with lower stacking fault energies and may completely disappear. The subgrain structure is not preferred in class I materials.

Initially, during the primary creep with a high creep rate, deformation and kink bands are created, at whose the tilt boundaries are forming. Pure tilt boundaries are perpendicular to the slip plane and also the slip direction. Also twist boundaries are formed. These are formed by coplanar systems of screw dislocations and are parallel to their slip plane.

The heterogenous structure produced during the primary creep consists of small parallel subgrains and also large subgrains. During the ongoing deformation, the smaller subgrains are growing and the larger subgrains are shrinking. These processes make the structure more homogeneous. As the smaller subgrains are merging, the boundaries are either decomposed, or these can join after encountering each other. Free dislocations, which are not a part of any of the dislocation boundaries, remain in a 3D network even during the stationary creep.

The organisation of the cell structure formed by dislocation boundaries has been studied by Holt [29]. According to his work, the homogeneous distribution of screw dislocations is unstable, as the elastic energy of such configuration is high. This allows the dislocation structure to be rearranged to an inhomogeneous modulated distribution with a wavelength equal to the mean subgrain size.

The formation of the cell structure affects also the free dislocation density (i.e. the density of the dislocations not lying in the subgrain boundaries). Initially, the dislocation density quickly increases with the onset of the primary creep. However, these dislocations readily form the subgrain boundaries. This process leads to a decrease of the density of free dislocations. On the other hand, the total dislocation density grows monotonically up to the stationary creep regime [1]. Experimental data on the evolution of dislocation densities with creep strain for $\alpha - \mathrm{Fe}$ creep tested at temperature 873 K and applied stress 75 MPa are shown in Fig. I.8.

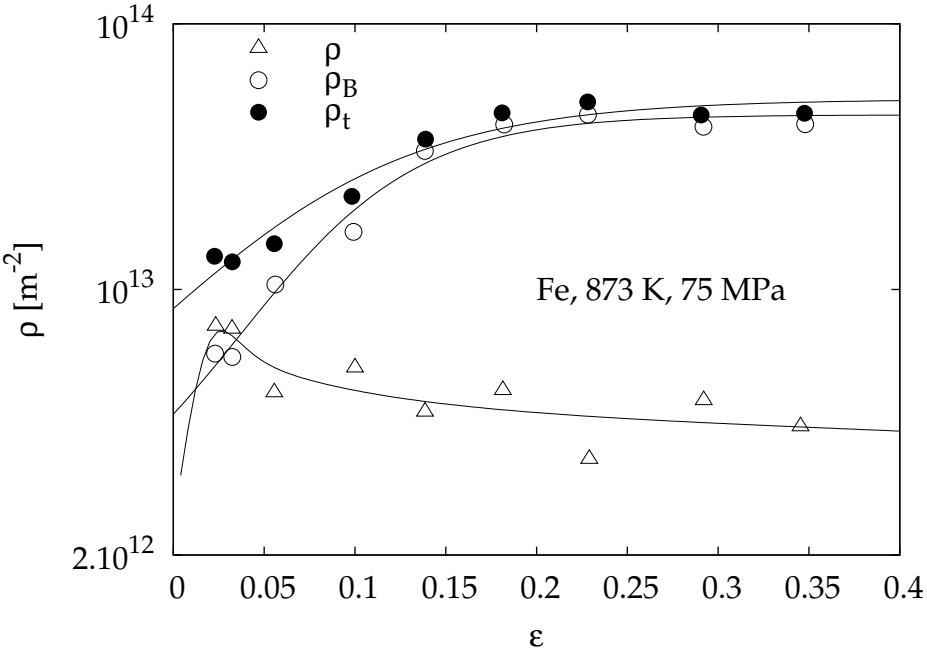

Figure I.8: Change of total dislocation density ρ_t, density of free dislocations ρ and dislocations inside the subgrain boundaries ρ_B with the creep strain ε for $\alpha -$ Fe crept at 873 K and 75 MPa. The plot is taken from [1].

I.4 Discrete dislocation dynamics

The discrete dislocation dynamics (DDD) is a method designed to investigate evolution of dislocation structures using numerical simulations. This method addresses a collective motion of many dislocations. The DDD simulations mimic fairly well real processes in crystalline materials [30–42]. The spatial scale of the simulation is on the order of microns (the grain size). The time scale usually covers the range of seconds (like in the in-situ TEM experiments) or minutes (fast creep tests).

Like in the in-situ TEM experiments, the simulation focuses on individual dislocations, whose response to the stress and temperature conditions in the material is studied. Apart from real experiments, the simulation offers a fine control of the simulation conditions (temperature, applied stress) and the material properties (elastic moduli, crystallography, initial dislocation structure). A realistic DDD model is thus expected to provide an important insight into the fundamental processes concerning the crystal plasticity, especially at high temperatures.

The DDD methods are targeted at dislocation systems consisting of individual dislocation lines, where every dislocation line does interact with each other. A driving force for dislocation motion is described by Peach-Koehler (P-K) force [6]. The DDD methods can be roughly divided according to the representation of the dislocation structure.

I.4.1 2D DDD methods

The two-dimensional methods are focused on a special case, where the dislocation structure consists only of straight dislocations of infinite length. The real 3D system can thus be represented by a 2D plane, where the dislocations are represented with their

intersections with the plane. The models consider usually both the conservative (glide) and non-conservative (climb) motion, allowing thus to cover thermally activated processes including diffusion, which control deformation at high temperatures (section I.3). Some models also include interactions with secondary phases (precipitates) of various shapes [43, 44].

Although such models do not use a realistic representation of the dislocation structure, they have provided valuable results concerning e.g. the particle strengthening of a composite material [43, 44]. The major advantage of such models is a straightforward calculation of the dislocation-dislocation interaction, which simplifies the numerical implementation and increases the computational speed.

I.4.2 3D DDD methods

I.4.3 Segment representation

A realistic representation of the dislocation structure requires a 3D approach. Dislocations with arbitrary shapes may be incorporated into a 3D model. The dislocation lines are usually represented by discrete short straight segments. The piece-wise discretisation either follows the smooth and continuous dislocation lines with segments of suitable, but unconstrained direction [30, 34, 39, 45], where the segments may have a mixed, edge and screw character (Fig. I.9a), or uses pure edge and straight segments (Fig. I.9b) [33, 46–48]. It is also possible to use curved segments represented by, e.g, cubic or quintic splines, but this approach is not very common (see e.g. a parametric dislocation dynamics work by Ghoniem [49, 50]).

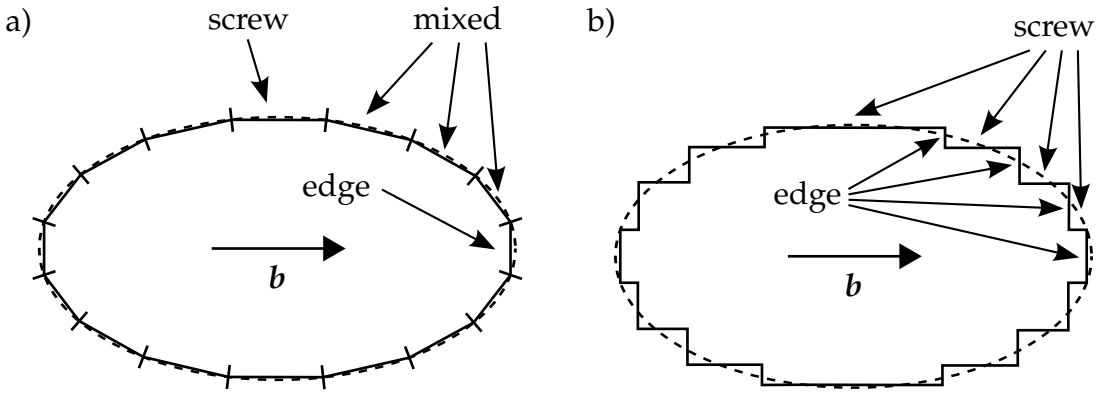

Figure I.9: A smooth elliptic dislocation loop (dashed line) in two distinct straight segment representations (solid line): a) arbitrary polygon with segments of a mixed character, b) pure edge and screw segments only.

The approach of straight segments with arbitrary direction will be further worked on in this thesis. As can be seen from the Fig. I.9, this representation offers a better approximation for a curved dislocation line with a given number of segments. This specially applies to (even straight) lines of a mixed character, where the pure edge and screw segment approach would need an excessive number of segments for a fine representation of the line.

I.4.4 Models with and without climb

The 3D DDD methods bring a more complex representation of the dislocation system. In some models, the dislocation mobility is constrained to a particular slip system, allowing thus only a conservative motion of the dislocations [30,48]. This approach is justified for low temperature processes, where the diffusion does not significantly contribute to the dislocation motion. On the other hand, the models based on common segments, which take the diffusion into account, are only two-dimensional. One example of a 3D DDD model with diffusion is an extension of an existing 3D model with the pure edge and screw segment representation [33] by Mordehai [51].

II. Objectives of the work

The present work addresses evolution of dislocation structures at high temperatures in crystals strengthened by secondary phases. The evolution is to be approximated by discrete dislocation dynamics using a 3D representation of the system. The aim of the work is to construct a numerical model able to simulate collective motion of dislocations in crystalline materials at high temperatures.

The model should implement following features:

- The dislocation structure should be represented by short straight segments, which form polygonal chains representing the individual dislocation lines.
- The calculation of the stress field in the dislocation structure should be based upon the linear theory of elasticity.
- The dislocation motion should include conservative motion – glide in crystallographic slip planes, non-compact glide and non-conservative motion – diffusion-controlled climb.
- The model should address geometrical constraint imposed on dislocation motion by rigid precipitates of secondary phases.

The model should be applied to following situations:

- Evolution of planar systems – dislocation loops, Frank-Read sources.
- Evolution of 3D benchmark systems – coaxial dislocation loops.
- Motion of a low-angle dislocation boundary (LADB) under an applied stress.
- Quantitative analysis of plastic deformation associated with the motion of the LADB.

III. Selected chapters of the theory of elasticity

III.1 The strain tensor

If a solid body, which is considered as a continuum, undergoes a deformation, the volume and the shape of the body changes. The deformation can be described in the following way. If a point $\boldsymbol{r} = (x_1, x_2, x_3)$ is displaced during the deformation to a position $r' = (x_1', x_2', x_3')$, the distance between the positions is described by the *displacement* $\boldsymbol{u}$:

$$\boldsymbol{u} = \boldsymbol{r}' - \boldsymbol{r}, \quad u_i = x_i' - x_i. \tag{III.1}$$

The distances between the points in the body change during the deformation. If we consider two points in an infinite distance $\mathrm{d}x_i$, the change of their distance during the deformation is described by a vector $\mathrm{d}x_i' = \mathrm{d}x_i + \mathrm{d}u_i$. The distance is $\mathrm{d}l^2 = \sum_{i=1}^3 \mathrm{d}x_i^2$ and changes to $\mathrm{d}l'^2 = \sum_{i=1}^3 \mathrm{d}x_i'^2 = \sum_{i=1}^3 (\mathrm{d}x_i + \mathrm{d}u_i)^2$. Rewriting $\mathrm{d}u_i = (\partial u_i/\partial x_j)\mathrm{d}x_j$ gives[1]

$$\mathrm{d}l'^2 = \mathrm{d}l^2 + 2\frac{\partial u_i}{\partial x_j}\mathrm{d}x_i\mathrm{d}x_j + \frac{\partial u_i}{\partial x_j}\frac{\partial u_i}{\partial x_k}\mathrm{d}x_j\mathrm{d}x_k = \mathrm{d}l^2 + \left(\frac{\partial u_i}{\partial x_j} + \frac{\partial u_j}{\partial x_i} + \frac{\partial u_k}{\partial x_j}\frac{\partial u_k}{\partial x_i}\right)\mathrm{d}x_i\mathrm{d}x_j. \tag{III.2}$$

If we introduce a tensor ε_{ij} defined as

$$\varepsilon_{ij} = \frac{1}{2}\left(\frac{\partial u_i}{\partial x_j} + \frac{\partial u_j}{\partial x_i} + \frac{\partial u_k}{\partial x_i}\frac{\partial u_k}{\partial x_j}\right), \tag{III.3}$$

we may rewrite the equation (III.2) as

$$\mathrm{d}l'^2 = \mathrm{d}l^2 + 2\varepsilon_{ij}\mathrm{d}x_i\mathrm{d}x_j. \tag{III.4}$$

The ε_{ij} is a *strain tensor*, which is symmetric by definition ($\varepsilon_{ij} = \varepsilon_{ji}$). For the further discussion we assume that the deformation is small, and we keep only the first-order terms in (III.2), so we get

$$\varepsilon_{ij} = \frac{1}{2}\left(\frac{\partial u_i}{\partial x_j} + \frac{\partial u_j}{\partial x_i}\right). \tag{III.5}$$

III.2 The stress tensor

When external forces are applied upon a solid body, the body is deformed, which induces not only strain but also internal stresses in the body. Let us consider a force $\boldsymbol{f}$ per

[1] Unless specified otherwise, repeated indices in the formulas mean a summation, so we write $\mathrm{d}u_i = \sum_{j=1}^3 (\partial u_i/\partial x_j)\mathrm{d}x_j = (\partial u_i/\partial x_j)\mathrm{d}x_j$.

unit volume in the body. The total force acting upon a volume V is determined by a volume integral $\int \boldsymbol{f}\,\mathrm{d}V$.

The force $\boldsymbol{f} = (f_1, f_2, f_3)$ per unit volume fulfils a relation of force equilibrium

$$f_i = \frac{\partial \sigma_{ij}}{\partial x_j}. \tag{III.6}$$

The force acting upon a volume V closed by surface A is

$$\int_V f_i \,\mathrm{d}V = \int_V \frac{\partial \sigma_{ij}}{\partial x_j}\,\mathrm{d}V = \oint_A \sigma_{ij}\,\mathrm{d}A_j, \tag{III.7}$$

where $\mathrm{d}A_j$ is an area of the surface element multiplied by a local normal vector to the surface.

III.2.1 The thermodynamics of the deformation

Now we focus on the work per unit volume $\delta w = f_i \delta u_i$ done by the body forces per unit volume f_i, when the displacement u_i changes by δu_i:

$$\int_V \delta w\,\mathrm{d}V = \int_V \frac{\partial \sigma_{ij}}{\partial x_j}\delta u_i\,\mathrm{d}V = \int_V \left[\frac{\partial(\sigma_{ij}\delta u_i)}{\partial x_j} - \sigma_{ij}\frac{\partial \delta u_i}{\partial x_j}\right]\mathrm{d}V = \oint_S \sigma_{ij}\delta u_i \mathrm{d}A_j - \int_V \sigma_{ij}\frac{\partial \delta u_i}{\partial x_j}\,\mathrm{d}V. \tag{III.8}$$

The formula (III.8) is modified by the integration by parts and the Stokes' theorem. If we extend the integration surface to infinity, there is no deformation on the surface. Thus the first integral in (III.8) vanishes. As the stress tensor σ_{ij} is symmetric, we may substitute $\sigma_{ij} \to (\sigma_{ij} + \sigma_{ji})/2$ and (III.5) to the second integral in (III.8), which leads to

$$\delta w = -\sigma_{ij}\delta\varepsilon_{ij}. \tag{III.9}$$

Now we introduce the internal energy E per unit volume. An infinitesimal change of the internal energy due to external work is specified as (see [8])

$$\mathrm{d}E = T\mathrm{d}s - \mathrm{d}w, \tag{III.10}$$

where T is the temperature, s is the entropy per unit volume and δw is determined by the relation (III.9). We assume a slow deformation process, which keeps thermodynamic equilibrium. Now we introduce the free energy $F = E - Ts$. Differentiating of the free energy gives

$$\mathrm{d}F = -s\mathrm{d}T - \mathrm{d}w = -s\mathrm{d}T + \sigma_{ij}\delta\varepsilon_{ij}. \tag{III.11}$$

The free energy is suitable for expressing the stress tensor at a constant temperature:

$$\sigma_{ij} = \left.\frac{\partial F}{\partial \varepsilon_{ij}}\right|_{T=\text{const.}}. \tag{III.12}$$

III.3 Hooke's law

Let us now expand the free energy in terms of the strain tensor to the second order. For a deformed body at a constant temperature T, the undeformed state corresponds to a state with no acting external forces at the temperature T. Then both ε_{ij} and σ_{ij} are equal to zero. According to (III.12), the first-order (linear) term vanishes. Thus the expansion of F to the second order will be

$$F = F_0 + \frac{1}{2}\lambda\left(\sum_{i=1}^{3}\varepsilon_{ii}\right)^2 + \mu\sum_{i=1}^{3}\sum_{j=1}^{3}\varepsilon_{ij}^2. \tag{III.13}$$

This relation is valid for a free energy of a deformed isotropic body [8]. The factors λ and μ are called *Lamé coefficients*. It is convenient to separate the trace of the strain tensor, which corresponds to changes in the body volume [8]. The trace of the strain tensor is zero for a case of a *pure shear*. On the other hand, if only the trace of the strain tensor is nonzero, it is a *hydrostatic compression*. We may decompose the strain to a sum of a pure shear and a hydrostatic compression:

$$\varepsilon_{ij} = \left(\varepsilon_{ij} - \frac{1}{3}\delta_{ij}\varepsilon_{kk}\right) + \frac{1}{3}\delta_{ij}\varepsilon_{ll}. \tag{III.14}$$

This allows to rewrite the free energy:

$$F = F_0 + \mu\sum_{i=1}^{3}\sum_{j=1}^{3}\left(\varepsilon_{ij} - \frac{1}{3}\delta_{ij}\varepsilon_{kk}\right)^2 + \frac{1}{2}K\varepsilon_{ll}^2, \tag{III.15}$$

where K is the *bulk modulus*. The coefficient μ is a *shear modulus*, as it is connected with the shear component of the strain.

The bulk modulus can be expressed in terms of the Lamé coefficients as

$$K = \lambda + \frac{2}{3}\mu. \tag{III.16}$$

The free energy has a minimum value in a thermodynamic equilibrium, if no external forces are acting upon the continuum. This means $F(\varepsilon_{ij}) = 0$ for $\varepsilon_{ij} = 0$, which can be satisfied by a positive quadratic form, which requires that K and μ are positive, i. e. $K > 0$ and $\mu > 0$.

If we differentiate (III.15), we get

$$\begin{aligned} \mathrm{d}F &= 2\mu\sum_{i=1}^{3}\sum_{j=1}^{3}\left(\varepsilon_{ij} - \frac{1}{3}\delta_{ij}\varepsilon_{kk}\right)\mathrm{d}\left(\varepsilon_{ij} - \frac{1}{3}\delta_{ij}\varepsilon_{kk}\right) + K\varepsilon_{ll}\mathrm{d}\varepsilon_{ll} = \\ &= 2\mu\sum_{i=1}^{3}\sum_{j=1}^{3}\left(\varepsilon_{ij} - \frac{1}{3}\delta_{ij}\varepsilon_{kk}\right)\mathrm{d}\varepsilon_{ij} + K\varepsilon_{ll}\mathrm{d}\varepsilon_{ll}. \end{aligned} \tag{III.17}$$

Rewriting the trace of the strain tensor leads to

$$\mathrm{d}F = \sum_{i=1}^{3}\sum_{j=1}^{3}\left[2\mu\left(\varepsilon_{ij} - \frac{1}{3}\delta_{ij}\varepsilon_{kk}\right) + K\delta_{ij}\varepsilon_{ll}\right]\mathrm{d}\varepsilon_{ij}. \tag{III.18}$$

Substituting (III.18) to (III.12) gives a relation

$$\sigma_{ij} = 2\mu \left(\varepsilon_{ij} - \frac{1}{3}\delta_{ij}\varepsilon_{kk} \right) + K\delta_{ij}\varepsilon_{ll}. \tag{III.19}$$

The trace of the stress tensor is

$$\sigma_{ii} = 3K\varepsilon_{ll}, \tag{III.20}$$

as the sum of the diagonal of the first term in (III.19) is identically zero. Substituting this back to the (III.19) gives

$$\varepsilon_{ij} = \frac{1}{2\mu} \left(\sigma_{ij} - \frac{1}{3}\delta_{ij}\sigma_{kk} \right) + \frac{1}{9K}\delta_{ij}\sigma_{ll}, \tag{III.21}$$

which is the Hooke's law for the isotropic continuum.

Substituting the expression for the bulk modulus (III.16) into (III.19) leads to

$$\sigma_{ij} = 2\mu\varepsilon_{ij} + \lambda\delta_{ij}\varepsilon_{kk}, \tag{III.22}$$

$$\text{where} \quad \lambda = \frac{2\nu\mu}{1-2\nu}. \tag{III.23}$$

Now we introduce elastic constants c_{ijkl}, which express a relation between the stress tensor and the strain tensor:

$$\sigma_{ij} = c_{ijkl}\varepsilon_{kl}. \tag{III.24}$$

Substituting the formula (III.5) into (III.24) gives a relation between the stress tensor and the displacement:

$$\sigma_{ij} = c_{ijkl}\frac{\partial u_k}{\partial x_l} \tag{III.25}$$

Comparing (III.25) with (III.22) gives elastic constants for an isotropic continuum:

$$c_{ijkl} = \mu(\delta_{ik}\delta_{jl} + \delta_{il}\delta_{jk}) + \lambda\delta_{ij}\delta_{kl}. \tag{III.26}$$

III.3.1 Finding the displacement by the Green function method

The following derivations follows ideas from [6]. We start with the equation for the force equilibrium (III.6). We substitute (III.25):

$$f_i = c_{ijkl}\frac{\partial^2 u_k}{\partial x_j \partial x_l}. \tag{III.27}$$

Substituting (III.26) for an isotropic case, we have

$$f_i = (\lambda+\mu)\frac{\partial}{\partial x_i}\frac{\partial u_j}{\partial x_j} + \mu\frac{\partial^2 u_i}{\partial x_l \partial x_l}, \quad \boldsymbol{f} = (\lambda+\mu)\boldsymbol{\nabla}(\boldsymbol{\nabla}\cdot\boldsymbol{u}) + \mu\Delta\boldsymbol{u}. \tag{III.28}$$

The vector field $\boldsymbol{u}$ may be represented by a combination of a scalar potential ϕ and a vector potential $\boldsymbol{A}$:

$$\boldsymbol{u} = \boldsymbol{\nabla}\phi + \boldsymbol{\nabla}\times\boldsymbol{A}, \quad u_i = \frac{\partial\phi}{\partial x_i} + \epsilon_{ijk}\frac{\partial A_k}{\partial x_j}. \tag{III.29}$$

Substituting (III.29) into (III.28) leads to

$$f_i = (\lambda + 2\mu)\Delta\frac{\partial\phi}{\partial x_i} + \mu\Delta\epsilon_{ijk}\frac{\partial A_k}{\partial x_j}. \tag{III.30}$$

For a particular choice of ϕ and $\boldsymbol{A}$, the equation (III.28) is equivalent to a biharmonic equation. We choose following scalar potential ϕ and vector potential $\boldsymbol{A}$:

$$\phi = \frac{\tilde{f}_j}{8\pi(\lambda+2\mu)}\frac{\partial r}{\partial x_j}, \quad A_i = \epsilon_{ijk}\frac{\tilde{f}_j}{8\pi\mu}\frac{\partial r}{\partial x_k}. \tag{III.31}$$

This choice of potentials gives a biharmonic equation:

$$\begin{aligned} f_i &= \frac{\tilde{f}_m}{8\pi}\frac{\partial^2}{\partial x_m\partial x_i}\Delta r + \frac{\tilde{f}_m}{8\pi}\epsilon_{ijk}\epsilon_{kmn}\frac{\partial^2}{\partial x_n\partial x_j}\Delta r = \left|\epsilon_{ijk}\epsilon_{kmn} = \delta_{im}\delta_{jn} - \delta_{in}\delta_{jm}\right| = \\ &= \frac{\tilde{f}_m}{8\pi}\frac{\partial^2}{\partial x_m\partial x_i}\Delta r + \frac{1}{8\pi}\left(\tilde{f}_i\frac{\partial^2}{\partial x_j\partial x_j} - \tilde{f}_j\frac{\partial^2}{\partial x_i\partial x_j}\right)\Delta r = \frac{\tilde{f}_i}{8\pi}\Delta\Delta r. \end{aligned} \tag{III.32}$$

For a case of a point force $\tilde{f}_i = -f_i\delta(\boldsymbol{r})$, the biharmonic equation[2] takes the following form:

$$\Delta\Delta|\boldsymbol{r}| = -8\pi\delta(\boldsymbol{r}). \tag{III.34}$$

Inserting this into the relation for the displacement (III.29) leads to

$$\begin{aligned} u_i &= \frac{\tilde{f}_j}{8\pi(\lambda+2\mu)}\frac{\partial^2}{\partial x_j\partial x_i} + \epsilon_{ijk}\epsilon_{kmn}\frac{\tilde{f}_m}{8\pi\mu}\frac{\partial^2 r}{\partial x_j\partial x_m} = \left|\epsilon_{ijk}\epsilon_{kmn} = \delta_{im}\delta_{jn} - \delta_{in}\delta_{jm}\right| = \\ &= \frac{\tilde{f}_j}{8\pi(\lambda+2\mu)}\frac{\partial^2}{\partial x_j\partial x_i} + \frac{1}{8\pi\mu}\left[\tilde{f}_i\frac{\partial^2 r}{\partial x_j\partial x_j} - \tilde{f}_j\frac{\partial^2 r}{\partial x_j\partial x_i}\right] = \\ &= \frac{1}{8\pi\mu}\left[\tilde{f}_i\Delta r - \tilde{f}_j\frac{\lambda+\mu}{\lambda+2\mu}\frac{\partial^2 r}{\partial x_j\partial x_i}\right]. \end{aligned} \tag{III.35}$$

The displacement can be also expressed as $u_i = \tilde{f}_j u_{ij}$, where

$$u_{ij} = \frac{1}{8\pi\mu}\left[\delta_{ij}\Delta r - \frac{\lambda+\mu}{\lambda+2\mu}\frac{\partial^2 r}{\partial x_j\partial x_i}\right]. \tag{III.36}$$

A displacement caused by a continuous distribution of forces $f_j(\boldsymbol{r})$ in an elastic continuum is then given by

$$u_i(\boldsymbol{r}) = \int u_{ij}(\boldsymbol{r}-\boldsymbol{r}')f_j(\boldsymbol{r}')\mathrm{d}V'. \tag{III.37}$$

[2]The relation (IV.11c) has been used: $\Delta|\boldsymbol{r}| = 2/|\boldsymbol{r}|$.
The equation (III.34) is analogic to an electrostatic potential problem.
An electrostatic potential fulfils the Poisson equation:

$$\Delta V(\boldsymbol{r}) = -4\pi\rho(\boldsymbol{r}), \tag{III.33}$$

where $V(\boldsymbol{r})$ is an electrostatic potential and $\rho(\boldsymbol{r})$ is a charge density.

IV. Basics of dislocation theory

IV.1 Dislocations and deformation

IV.1.1 Burgers vector in terms of the theory of elasticity

The dislocations are line defects in a crystalline material. They have a defined direction (unit vector $\boldsymbol{\xi}$) and a Burgers vector $\boldsymbol{b}$, which measures the strength of the dislocation defect. As mentioned in section I.2.2, the Burgers vector is defined by a closed circuit in the damaged crystal, which is transferred to the perfect crystal and closed by the Burgers vector (FS/RH convention). Now we introduce the *local Burgers vector* (Fig. IV.1).

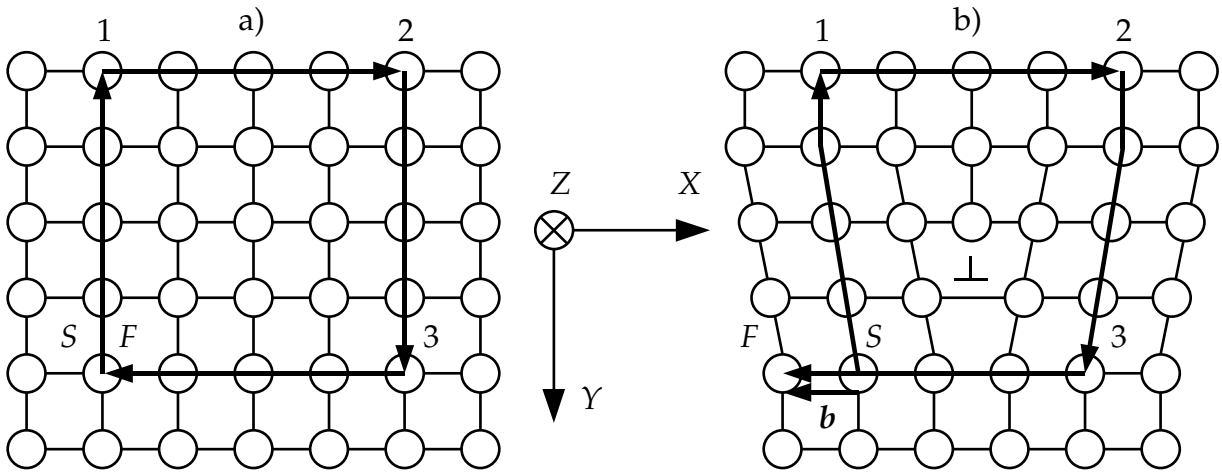

Figure IV.1: The local Burgers vector (SF/RH convention).

The difference is that the local Burgers vector is not affected by elastic strains and thermal vibrations [6]. The circuit is made at first in the perfect crystal, then it is transposed to the crystal with the dislocation. Again, the circuit has the right-hand sense (section I.2.2). As in the definition of the true Burgers vector, the transposed circuit is not closed. To make the local Burgers vector consistent with the true Burgers vector, we connect the starting point S with the ending point F. This is a SF/RH convention. Actually, these two definitions coincide, when we take a limit of the circuit becoming large enough to lie in a perfect crystal.

An alternative definition of the local Burgers vector is possible with the displacement field $\boldsymbol{u}$ in the theory of elasticity. Let us take a contour integral about a dislocation line along an arbitrary contour $\mathcal{C}$, called a *Burgers circuit*, which encircles the dislocation in an undamaged material:

$$\boldsymbol{b} = \oint_{\mathcal{C}} \frac{\partial \boldsymbol{u}}{\partial l}\,\mathrm{d}l. \tag{IV.1}$$

The situation is illustrated in Fig. IV.2. A dislocation line is a boundary of an area subjected to slip displacement. Because of this, dislocation lines cannot end in a point

inside the crystal, unless it meets another dislocation, free surface, grain boundary or another defect (e.g. a precipitate).

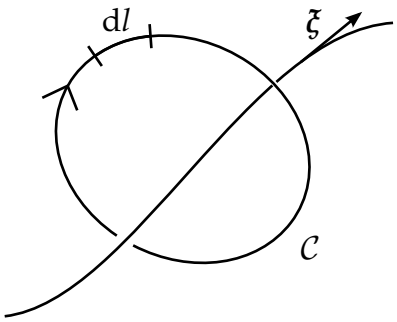

Figure IV.2: Definition of the Burgers vector in a continuum theory.

IV.1.2 Conservation of the Burgers vector

The Burgers vector is computed by the contour integral along a Burgers circuit (equation (IV.1). The result of the integral does not change, if we reshape the circuit, as long as it remains in an undamaged crystal. If there are three or more dislocations meeting at a particular point (a *junction*), we can pull the Burgers circuit of one of the dislocation over the junction. It will encircle the remaining dislocations coming to the point (Fig. IV.3).

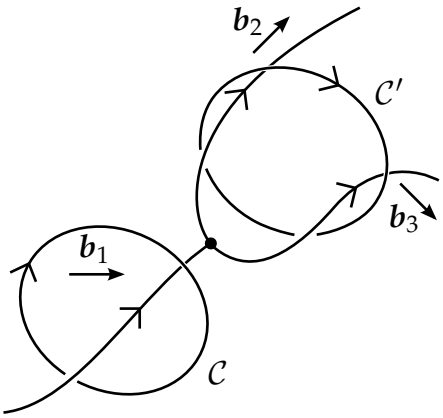

Figure IV.3: Transformation of the Burgers circuit $\mathcal{C}$ to $\mathcal{C}'$.

As the condition of the contour lying in the undamaged material is satisfied, the result of the integral is the same. If the first dislocation has a Burgers vector $\boldsymbol{b}_1$, while the other have $\boldsymbol{b}_2, \boldsymbol{b}_3, \ldots$, we have:

$$\boldsymbol{b}_1 = \sum_{i=2}^{n} \boldsymbol{b}_i \tag{IV.2}$$

for n dislocations. If we invert the sense ξ of the first dislocation, so that all of them are coming out of the junction, the relation changes to

$$\sum_{i=1}^{n} \boldsymbol{b}_i = \boldsymbol{0}. \tag{IV.3}$$

IV.2 Theory of curved dislocations

IV.2.1 Displacement vector field

In the following paragraphs, a displacement connected with a particular dislocation loop will be derived, following the steps from [6]. When a dislocation is created, a displacement at $\boldsymbol{r}$ is determined by the displacement vector field $\boldsymbol{u}(\boldsymbol{r})$. A point force $\boldsymbol{F}$ acting during the creation of the dislocation at the point $\boldsymbol{r}$ does work

$$W = \boldsymbol{F} \cdot \boldsymbol{u}(\boldsymbol{r}) = F_m u_m(\boldsymbol{r}), \tag{IV.4}$$

where $\boldsymbol{F} = \{F_m\}$, $\boldsymbol{u}(\boldsymbol{r}) = \{u_m(\boldsymbol{r})\}$, $m \in \{1,2,3\}$. Let us assume that the creation of the dislocation (the building of the displacement field $\boldsymbol{u}(\boldsymbol{r})$) relieves the point force $\boldsymbol{F}$. Then an energy of the system decreases by an mount W, the interaction energy. However, the contributions to the elastic energy from the stress field of dislocation and the stress field produced by the force $\boldsymbol{F}$ are independent, i.e. have no cross terms [6]. Also the dislocation line is not a sink of interaction energy. Therefore, the interaction energy W must be consumed during the creation of the $\boldsymbol{u}(\boldsymbol{r})$ field.

We apply these principles to a case of a dislocation loop in an infinite material (Fig. IV.4). Here, the energy W is spent as the work done on the surface A during the creation of the dislocation loop $\mathcal{C}$:

$$W = -\int_A \mathrm{d}A_j \, b_i F_m \sigma_{ij_m}(\boldsymbol{r}' - \boldsymbol{r}), \tag{IV.5}$$

where $F_m\sigma_{ij_m}(\boldsymbol{r}' - \boldsymbol{r})$ is the stress σ_{ij} at $\boldsymbol{r}'$ due to the point force $\boldsymbol{F}_m$ at $\boldsymbol{r}$. The Burgers vector b is specified by its components b_i and the surface element $\mathrm{d}\boldsymbol{A}$ by $\mathrm{d}A_j$.

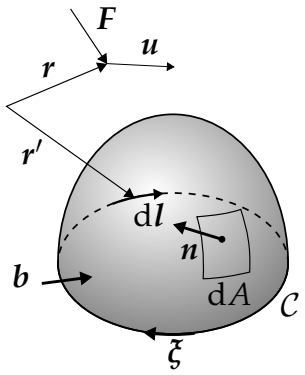

Figure IV.4: A point force $\boldsymbol{F}$ acting within an infinite elastic material containing a dislocation loop.

Using the Hooke's law (III.25), the relation (IV.5) turns into

$$W = -\int_A \mathrm{d}A_j \, b_i c_{ijkl} \frac{\partial F_m u_{mk}(\boldsymbol{r}' - \boldsymbol{r})}{\partial x_l'}, \tag{IV.6}$$

where $u_{mk}(\boldsymbol{r}' - \boldsymbol{r})$ is the Green's function of elastic displacements (III.36). We choose F_m with only one nonzero component $m' \in \{1,2,3\}$ ($F_m = F_m'\delta_{mm'}$) and substitute it into equations (IV.4) and (IV.6). Furthermore, we recall the argument related to the balance

of the interaction energy W and the work spent on the surface A and equate the (IV.4) and (IV.6), which yields

$$u_m(\boldsymbol{r}) = -\int_A \mathrm{d}A_j\, b_i c_{ijkl} \frac{\partial u_{mk}(\boldsymbol{r}'-\boldsymbol{r})}{\partial x'_l}. \tag{IV.7}$$

The relation (IV.7) applies generally to anisotropic material. In further derivations, an isotropic material is assumed.

Substituting (III.26) for the elastic constants for an isotropic material, the relation (IV.7) changes to

$$\begin{aligned} u_m(\boldsymbol{r}) &= -\int_A \mathrm{d}A_j\, b_i \left[\mu(\delta_{ik}\delta_{jl}+\delta_{il}\delta_{jk})+\lambda\delta_{ij}\delta_{kl}\right] \frac{\partial u_{mk}}{\partial x'_l} = \\ &= -\lambda\int_A \mathrm{d}A_i\, b_i \frac{\partial u_{mk}}{\partial x'_l} - \mu\int_A \mathrm{d}A_j\, b_i \frac{\partial u_{mi}}{\partial x'_j} - \mu\int_A \mathrm{d}A_j\, b_i \frac{\partial u_{mj}}{\partial x'_i}. \end{aligned} \tag{IV.8}$$

As a next step, the Green's function (III.36) is substituted. The following relations adopt substitutions $\boldsymbol{q} = \boldsymbol{r}' - \boldsymbol{r}$ and $q = |\boldsymbol{q}|$, where $\boldsymbol{r} = (x_1, x_2, x_3)$ and $\boldsymbol{r}' = (x'_1, x'_2, x'_3)$. A straightforward calculation leads to a relation for partial differentials of q:

$$\frac{\partial q}{\partial x'_i} = -\frac{\partial q}{\partial x_i}. \tag{IV.9}$$

For vector notation we use

$$[\boldsymbol{\nabla}\phi]_i = \frac{\partial\phi}{\partial x_i}, \quad [\boldsymbol{\nabla}'\phi]_i = \frac{\partial\phi}{\partial x'_i}, \quad \Delta\phi = \sum_i \frac{\partial^2}{\partial x_i^2}\phi, \quad \Delta'\phi = \sum_i \frac{\partial^2}{\partial x_i'^2}\phi, \tag{IV.10}$$

where ϕ is a scalar function. Following identities will be frequently used:

$$\begin{aligned} a)\ \boldsymbol{\nabla}' q &= \frac{\boldsymbol{q}}{q}, \\ b)\ \boldsymbol{\nabla}' \frac{1}{q} &= -\frac{\boldsymbol{q}}{q^3} \\ c)\ \Delta' q &= \frac{2}{q}. \end{aligned} \tag{IV.11}$$

The relation for the displacement field then changes to

$$\begin{aligned} u_m(\boldsymbol{r}) &= -\frac{1}{8\pi\mu}\left[\int_A \mathrm{d}A_i\, b_i\lambda\left(\frac{\partial\Delta' q}{\partial x' m} - \frac{\lambda+\mu}{\lambda+2\mu}\frac{\partial^3 q}{\partial x'_m \partial x'^2_k}\right) + \mu\int_A \mathrm{d}A_j\, b_m \frac{\partial\Delta' q}{\partial x'_j} - \right. \\ &- \mu\int_A \mathrm{d}A_j\, b_i \frac{\lambda+\mu}{\lambda+2\mu}\frac{\partial^3 q}{\partial x'_m \partial x'_i \partial x'_j} + \mu\int_A \mathrm{d}A_m\, b_i \frac{\partial\Delta' q}{\partial x'_i} - \mu\int_A \mathrm{d}A_j\, b_i \frac{\lambda+\mu}{\lambda+2\mu}\frac{\partial^3 q}{\partial x'_m \partial x'_j \partial x'_i}\Bigg] = \\ &= \frac{1}{8\pi}\left(1-2\frac{\lambda+\mu}{\lambda+2\mu}\right)\int_A b_i \frac{\partial\Delta' q}{\partial x'_m}\,\mathrm{d}A_i - \frac{1}{8\pi}\int_A b_m \frac{\partial\Delta' q}{\partial x_j}\,\mathrm{d}A_j - \\ &- \frac{1}{8\pi}\int_A b_i \frac{\partial\Delta' q}{\partial x_i}\,\mathrm{d}A_m + \frac{1}{4\pi}\frac{\lambda+\mu}{\lambda+2\mu}\int_A b_i \frac{\partial^3 q}{\partial x'_m \partial x'_i \partial x'_j}\,\mathrm{d}A_j \end{aligned} \tag{IV.12}$$

The relation can be further rearranged by expanding $\Delta' q = \partial^2 q / \partial x_j'^2$ in the first term, allowing it to be combined with the third and fourth term. This makes the equation more symmetric:

$$\begin{aligned} u_m(\boldsymbol{r}) &= -\frac{1}{8\mu}\int_A b_m \frac{\partial \Delta' q}{\partial x_j'}, \mathrm{d}A_j - \frac{1}{8\pi}\int_A \left(b_i \frac{\partial \Delta' q}{\partial x_i'}\,\mathrm{d}A_m - b_i \frac{\partial \Delta' q}{\partial x_m'}\,\mathrm{d}A_i \right) + \\ &+ \frac{1}{4\pi}\frac{\lambda+\mu}{\lambda+2\mu}\int_A \left(b_i \frac{\partial}{\partial x_i'}\frac{\partial^2 q}{\partial x_m' \partial x_j'}\mathrm{d}A_j - b_i \frac{\partial}{\partial x_j'}\frac{\partial^2 q}{\partial x_m' \partial x_j'}\mathrm{d}A_i \right). \end{aligned} \tag{IV.13}$$

Here we make use of the Stokes' theorem:

$$\int_A (\boldsymbol{\nabla} \times \boldsymbol{B})\,\mathrm{d}\boldsymbol{A} = \oint_{\mathcal{C}} \boldsymbol{B} \cdot \mathrm{d}\boldsymbol{l}, \quad \int_A \epsilon_{ijk} \frac{\partial B_k}{\partial x_j}\,\mathrm{d}\boldsymbol{A}_i = \oint_{\mathcal{C}} \boldsymbol{B}_l \mathrm{d}l_l. \tag{IV.14}$$

If we insert $\boldsymbol{B} = \phi \boldsymbol{e}_k$ and $\mathrm{d}l = \mathrm{d}x_i \boldsymbol{e}_i$ and multiply the result with ϵ_{kmn} and then change the indices $\{m, n\} \to \{i, j\}$, we have

$$\int_A \left(\frac{\partial \phi}{\partial x_j}\mathrm{d}A_i - \frac{\partial \phi}{\partial x_i}\mathrm{d}A_j \right) = \epsilon_{ijk} \oint_{\mathcal{C}} \phi\,\mathrm{d}x_k, \tag{IV.15}$$

which corresponds to the second term of (IV.13) with $\phi = \Delta' q$ and the third term with $\phi = \partial^2 q / (\partial x_m' \partial x_j')$.

Using the Stokes' theorem transforms the relation for the displacement vector field of an isotropic crystal to

$$u_m(\boldsymbol{r}) = -\frac{1}{8\pi}\int_A b_m \frac{\partial \Delta' q}{\partial x_j'}\,\mathrm{d}A_j - \frac{1}{8\pi}\oint_{\mathcal{C}} b_i \epsilon_{mik} \Delta' q\,\mathrm{d}x_k' - \frac{1}{8\pi(1-\nu)}\oint_{\mathcal{C}} b_i \epsilon_{ijk} \frac{\partial^2 q}{\partial x_m' \partial x_j'}\,\mathrm{d}x_k'. \tag{IV.16}$$

The relation (IV.16) can be rewritten to a vector notation. Using (IV.11c) followed by (IV.11b), we may express the first integral in (IV.16) as

$$\Omega = -\int_A \frac{\boldsymbol{q} \cdot \mathrm{d}\boldsymbol{A}}{q^3}, \tag{IV.17}$$

which is the solid angle corresponding to the area A from a position $\boldsymbol{r}$. The second term just makes use of (IV.11c), leading to

$$-\frac{1}{4\pi}\oint_{\mathcal{C}} \frac{\boldsymbol{b} \times \mathrm{d}\boldsymbol{l}}{q}. \tag{IV.18}$$

The third term is rearranged by putting the derivative $\partial / \partial x_m'$ (gradient) before the integral and using (IV.11a) for $\partial / \partial x_j'$:

$$-\frac{1}{8\pi(1-\nu)}\boldsymbol{\nabla}' \oint_{\mathcal{C}} \frac{(\boldsymbol{b} \times \boldsymbol{q}) \cdot \mathrm{d}\boldsymbol{l}'}{q}. \tag{IV.19}$$

Combining (IV.17) + (IV.18) + (IV.19) gives

$$\boldsymbol{u}(\boldsymbol{r}) = -\frac{\boldsymbol{b}}{4\pi}\Omega - \frac{1}{4\pi}\oint_{\mathcal{C}} \frac{\boldsymbol{b} \times \mathrm{d}\boldsymbol{l}'}{q} + \frac{1}{8\pi(1-\nu)})\boldsymbol{\nabla} \oint_{\mathcal{C}} \frac{(\boldsymbol{b} \times \boldsymbol{q}) \cdot \mathrm{d}\boldsymbol{l}}{q}. \tag{IV.20}$$

IV.2.2 Stress field due to a curved dislocation

Having the vector field of displacement, it is possible to compute the stress field from the Hooke's law applied to the strain determined by the differentiation of the displacement field (IV.16) or its vector form (IV.20). At first we differentiate the solid angle Ω:

$$\frac{\partial \Omega}{\partial x_j} = \oint_{\mathcal{C}} \frac{\boldsymbol{q} \cdot (\boldsymbol{e}_j \times \mathrm{d}\boldsymbol{l})}{q^3}, \tag{IV.21}$$

which can be written also as

$$\frac{\partial \Omega}{\partial x_j} = -\frac{1}{2} \oint_{\mathcal{C}} \epsilon_{ijk} \frac{\partial \Delta' q}{\partial x'_i} \, \mathrm{d}x'_k. \tag{IV.22}$$

The relation (IV.22) is substituted into the derivative:

$$\frac{\partial u_m(\boldsymbol{r})}{\partial x_l} = \overbrace{\frac{b_m}{8\pi} \oint_{\mathcal{C}} \epsilon_{ilk} \frac{\partial \Delta' q}{\partial x'_i} \, \mathrm{d}x'_k - \frac{1}{8\pi} \oint_{\mathcal{C}} b_i \epsilon_{mik} \frac{\partial \Delta' q}{\partial x_l} \, \mathrm{d}x'_k}^{U_1} \overbrace{- \frac{1}{8\pi(1-\nu)} \oint_{\mathcal{C}} b_i \epsilon_{ijk} \frac{\partial^3 q}{\partial x_l \partial x'_m \partial x'_j} \, \mathrm{d}x'_k}^{U_2}. \tag{IV.23}$$

The formulation of the the Hooke's law as a function of the displacement field is (III.25). Inserting the elastic constants for isotropic continuum (III.26) leads to

$$\sigma_{\alpha\beta} = \frac{\partial u_m}{\partial x_l} [\overbrace{\mu(\delta_{\alpha m}\delta_{\beta l} + \delta_{\alpha l}\delta_{\beta m})}^{\mu} + \overbrace{\lambda \delta_{\alpha\beta}\delta_{ml}}^{\lambda}]. \tag{IV.24}$$

The rearrangement using (IV.9) and changing of indices yields:

$$\begin{aligned}
\mu\,U_1 &= \frac{\mu}{8\pi} \oint_{\mathcal{C}} \mathrm{d}x'_k \left[(b_m \epsilon_{ilk} \delta_{\alpha m} \delta_{\beta l} + b_m \epsilon_{ilk} \delta_{\alpha l} \delta_{\beta m}) \frac{\partial \Delta' q}{\partial x'_i} \right] + \\
&+ \frac{\mu}{8\pi} \oint_{\mathcal{C}} \mathrm{d}x'_k \left[(b_i \epsilon_{mik} \delta_{\alpha m} \delta_{\beta l} + b_i \epsilon_{mik} \delta_{\alpha l} \delta_{\beta m}) \frac{\partial \Delta' q}{\partial x'_l} \right] = \left| \begin{array}{c} \{m,i,l\} \to \{l,m,i\} \\ \text{in 2nd term} \end{array} \right| = \\
&= \frac{\mu}{8\pi} \oint_{\mathcal{C}} \mathrm{d}x'_k \left[\delta_{\alpha m}\delta_{\beta l}\epsilon_{ilk} + \delta_{\alpha l}\delta_{\beta m}\epsilon_{ilk} + \delta_{\alpha i}\delta_{\beta l}\epsilon_{lmk} + \delta_{\alpha l}\delta_{\beta i}\epsilon_{lmk} \right] b_m \frac{\partial \Delta' q}{\partial x'_i}, \qquad \text{(IV.25)} \\
\mu\,U_2 &= \frac{\mu}{8\pi(1-\nu)} \oint_{\mathcal{C}} \mathrm{d}x'_k \left[(b_i \epsilon_{ijk} \delta_{\alpha m} \delta_{\beta l} + b_i \epsilon_{ijk} \delta_{\alpha l} \delta_{\beta m} \right] \frac{\partial^3 q}{\partial x'_l \partial x'_m \partial x'_j} = \\
&= \frac{\mu}{4\pi(1-\nu)} \oint_{\mathcal{C}} \mathrm{d}x'_k \, b_i \epsilon_{ijk} \frac{\partial^3 q}{\partial x'_\alpha \partial x'_\beta \partial x'_j}, \qquad \text{(IV.26)} \\
\lambda\,U_1 &= \frac{\lambda}{8\pi} \oint_{\mathcal{C}} \mathrm{d}x'_k \, b_m \delta_{\alpha\beta}\delta_{ml} \epsilon_{ilk} \frac{\partial \Delta' q}{\partial x'_i} + \frac{\lambda}{8\pi} \oint_{\mathcal{C}} \mathrm{d}x'_k \, b_i \delta_{\alpha\beta}\delta_{ml} \epsilon_{mik} \frac{\partial \Delta' q}{\partial x'_l} = \\
&= \left| \begin{array}{c} i \leftrightarrow m / \text{1st term} \\ m \to j / \text{both terms} \end{array} \right| = -\frac{\lambda \delta_{\alpha\beta}}{4\pi} \oint_{\mathcal{C}} \mathrm{d}x'_k \, b_i \epsilon_{ijk} \frac{\partial \Delta' q}{\partial x'_j}, \qquad \text{(IV.27)} \\
\lambda\,U_2 &= \frac{\lambda}{8\pi(1-\nu)} \oint_{\mathcal{C}} \mathrm{d}x'_k \, \delta_{\alpha\beta}\delta_{ml} b_i \epsilon_{ijk} \frac{\partial^3 q}{\partial x'_l \partial x'_m \partial x'_j} = \\
&= \frac{\lambda \delta_{\alpha\beta}}{8\pi(1-\nu)} \oint_{\mathcal{C}} \mathrm{d}x'_k \, b_i \epsilon_{ijk} \frac{\partial \Delta' q}{\partial x'_j}. \qquad \text{(IV.28)}
\end{aligned}$$

Summing up the four relations above leads to

$$\begin{aligned}\sigma_{\alpha\beta} &= \frac{\mu}{8\pi}\oint_{\mathcal{C}} \mathrm{d}x'_k \,[\overbrace{\delta_{\alpha m}\delta_{\beta l}\epsilon_{ilk}}^{T_1} + \overbrace{\delta_{\alpha l}\delta_{\beta m}\epsilon_{ilk}}^{T_2} + \overbrace{\delta_{\alpha i}\delta_{\beta l}\epsilon_{lmk}}^{T_3} + \overbrace{\delta_{\alpha l}\delta_{\beta i}\epsilon_{lmk}}^{T_4}]\, b_m \frac{\partial \Delta' q}{\partial x'_i} + \\ &+ \frac{\mu}{4\pi(1-\nu)}\oint_{\mathcal{C}} \mathrm{d}x'_k \, b_i \epsilon_{ijk} \frac{\partial^3 q}{\partial x'_\alpha \partial x'_\beta \partial x'_j} - \frac{\mu\nu\delta_{\alpha\beta}}{4\pi(1-\nu)}\oint_{\mathcal{C}} \mathrm{d}x'_k \, b_i \epsilon_{ijk} \frac{\partial \Delta' q}{\partial x'_j},\end{aligned} \tag{IV.29}$$

where λ is expressed in terms of μ and ν, see (III.23).

The terms in the first integral can be further simplified using the following relation for the antisymmetric tensor:

$$\epsilon_{kij}\epsilon_{klm} = \delta_{il}\delta_{jm} - \delta_{im}\delta_{jl} \Rightarrow \delta_{il}\delta_{jm} = \epsilon_{kim}\epsilon_{klj} + \delta_{ij}\delta_{lm}. \tag{IV.30}$$

Therefore, following expansions apply to the first integral in (IV.29):

$$\begin{aligned}&(T_1) = \epsilon_{ilk}(\epsilon_{pl\alpha}\epsilon_{p\beta m} + \delta_{\alpha\beta}\delta_{lm}) = \epsilon_{p\beta m}(\delta_{ip}\delta_{k\alpha} - \delta_{i\alpha}\delta_{kp}) + \epsilon_{imk}\delta_{\alpha\beta} = \epsilon_{i\beta m}\delta_{k\alpha} - \epsilon_{k\beta m}\delta_{i\alpha} + \epsilon_{imk}\delta_{\alpha\beta},\\ &(T_2) = \epsilon_{ilk}(\epsilon_{pl\beta}\epsilon_{p\alpha m} + \delta_{\alpha\beta}\delta_{lm}) = \epsilon_{p\alpha m}(\delta_{ip}\delta_{k\beta} - \delta_{i\beta}\delta_{kp}) + \epsilon_{imk}\delta_{\alpha b} = \epsilon_{i\alpha m}\delta_{k\beta} - \epsilon_{k\alpha m}\delta_{i\beta} + \epsilon_{imk}\delta_{\alpha\beta},\\ &(T_3) = \epsilon_{\beta mk}\delta_{\alpha i},\\ &(T_4) = \epsilon_{\alpha mk}\delta_{\beta i}.\end{aligned} \tag{IV.31}$$

The term (T_3) is cancelled by the first term of the expansion of (T_1) and the term (T_4) by the second term of the expansion of (T_2). A summation of the terms above gives a result

$$2\epsilon_{imk}\delta_{\alpha\beta} + \epsilon_{i\beta m}\delta_{\alpha k} + \epsilon_{i\alpha m}\delta_{\beta k}. \tag{IV.32}$$

Substituting this result back to the equation (IV.29) gives

$$\begin{aligned}\sigma_{\alpha\beta} &= \frac{\mu}{8\pi}\oint_{\mathcal{C}} b_m \epsilon_{i\beta m}\frac{\partial \Delta' q}{\partial x'_i}\,\mathrm{d}x'_\alpha + \frac{\mu}{8\pi}\oint_{\mathcal{C}} b_m \epsilon_{i\alpha m}\frac{\partial \Delta' q}{\partial x'_i}\,\mathrm{d}x'_\beta - \frac{\mu\delta_{\alpha\beta}}{4\pi}\oint_{\mathcal{C}} b_i \epsilon_{ijk}\frac{\partial \Delta' q}{\partial x'_j}\,\mathrm{d}x'_k + \\ &+ \frac{\mu}{4\pi(1-\nu)}\oint_{\mathcal{C}} b_i \epsilon_{ijk}\frac{\partial^3 q}{\partial x'_\alpha \partial x'_\beta \partial x'_j}\,\mathrm{d}x'_k - \frac{\mu\nu\delta_{\alpha\beta}}{4\pi(1-\nu)}\oint_{\mathcal{C}} b_i \epsilon_{ijk}\frac{\partial \Delta' q}{\partial x'_j}\,\mathrm{d}x'_k,\end{aligned} \tag{IV.33}$$

where the indices in the third integral have been changed: $\{i, m\} \to \{j, i\}$. Grouping the terms with factor $\delta_{\alpha\beta}$ gives a final form for the stress field generated by a dislocation curve $\mathcal{C}$:

$$\begin{aligned}\sigma_{\alpha\beta} &= \frac{\mu}{8\pi}\oint_{\mathcal{C}} b_m \epsilon_{i\beta m}\frac{\partial \Delta' q}{\partial x'_i}\,\mathrm{d}x'_\alpha + \frac{\mu}{8\pi}\oint_{\mathcal{C}} b_m \epsilon_{i\alpha m}\frac{\partial \Delta' q}{\partial x'_i}\,\mathrm{d}x'_\beta + \\ &+ \frac{\mu}{4\pi(1-\nu)}\oint_{\mathcal{C}} b_i \epsilon_{ijk}\left[\frac{\partial^3 q}{\partial x'_\alpha \partial x'_\beta \partial x'_j} - \delta_{\alpha\beta}\frac{\partial \Delta' q}{\partial x'_j}\right]\mathrm{d}x'_k.\end{aligned} \tag{IV.34}$$

IV.2.3 Stress field due to a straight dislocation segment

The stress field formula (IV.34) will be used to calculate a stress field about a straight dislocation segment. To perform the calculation, a local coordinate system (x, y, z) is

adopted (Fig. IV.5). The vector $\boldsymbol{r} = (x, y, z)$ defines a point, in which the components of the stress tensor are calculated. The vector $\boldsymbol{r}'$ determines points on the dislocation segment and serves thus as an integration parameter. We recall the distance vector $\boldsymbol{q} = \boldsymbol{r}' - \boldsymbol{r}$. Its length is $q = |\boldsymbol{q}| = \sqrt{x^2 + y^2 + (z - z')^2}$. The dislocation segment of length L has endpoints at $[0, 0, -L/2]$ and $[0, 0, L/2]$.

The integration of the formula (IV.34) is carried along the z axis from $z = -L/2$ to $z = L/2$. This does not contradict the initial idea about the energy W originating from the point force $\boldsymbol{F}$, which is spent on the work done on the surface A, which is encircled by the dislocation loop $\mathcal{C}$ (see section IV.2.1). As long as the segmentation is applied to a dislocation loop, or to an infinite dislocation line (which can be considered as a part of a loop of an infinite radius), the calculation fulfils the initial assumptions. The result of the integration gives relations for the individual components of the stress tensor $\sigma_{\alpha\beta}(\boldsymbol{r})$ [6]:

$$
\begin{aligned}
\frac{\sigma_{xx}}{\sigma_0} &= b_x \frac{y}{q(q+\zeta)} \left[1 + \frac{x^2}{q^2} + \frac{x^2}{q(q+\zeta)}\right] + b_y \frac{x}{q(q+\zeta)} \left[1 - \frac{x^2}{q^2} - \frac{x^2}{q(q+\zeta)}\right], \\
\frac{\sigma_{yy}}{\sigma_0} &= -b_x \frac{y}{q(q+\zeta)} \left[1 - \frac{y^2}{q^2} - \frac{y^2}{q(q+\zeta)}\right] - b_y \frac{x}{q(q+\zeta)} \left[1 + \frac{y^2}{q^2} + \frac{y^2}{q(q+\zeta)}\right], \\
\frac{\sigma_{zz}}{\sigma_0} &= b_x \left[\frac{2\nu y}{q(q+\zeta)} + \frac{y\zeta}{q^3}\right] + b_y \left[-\frac{2\nu x}{q(q+\zeta)} - \frac{x\zeta}{q^3}\right], \\
\frac{\sigma_{xy}}{\sigma_0} &= -b_x \frac{x}{q(q+\zeta)} \left[1 - \frac{y^2}{q^2} - \frac{y^2}{q(q+\zeta)}\right] + b_y \frac{y}{q(q+\zeta)} \left[1 - \frac{x^2}{q^2} - \frac{x^2}{q(q+\zeta)}\right], \\
\frac{\sigma_{xz}}{\sigma_0} &= -b_x \frac{xy}{q^3} + b_y \left[-\frac{\nu}{q} + \frac{x^2}{q^3}\right] + b_z \frac{y(1-\nu)}{q(q+\zeta)}, \\
\frac{\sigma_{yz}}{\sigma_0} &= b_x \left[\frac{\nu}{q} - \frac{y^2}{q^3}\right] + b_y \frac{xy}{q^3} - b_z \frac{x(1-\nu)}{q(q+\zeta)}, \quad \text{where } \sigma_0 = \frac{\mu}{4\pi(1-\nu)} \text{ and } \zeta = z' - z.
\end{aligned}
\tag{IV.35}
$$

The stress components can be rewritten also in different terms [6]:

$$
\begin{aligned}
\frac{\sigma_{xx}}{\sigma_0} &= -b_x \frac{y\zeta}{\theta^2 q} \left(1 + \frac{2x^2}{\theta^2} + \frac{x^2}{q^2}\right) - b_y \frac{x\zeta}{\theta^2 q} \left(1 - \frac{2x^2}{\theta^2} - \frac{x^2}{\theta^2}\right) \\
\frac{\sigma_{yy}}{\sigma_0} &= b_x \frac{y\zeta}{\theta^2 q} \left(1 - \frac{2y^2}{\theta^2} - \frac{y^2}{q^2}\right) + b_y \frac{x\zeta}{\theta^2 q} \left(1 + \frac{2y^2}{\theta^2} + \frac{y^2}{\theta^2}\right) \\
\frac{\sigma_{zz}}{\sigma_0} &= -b_x \left(\frac{2\nu y\zeta}{\theta^2 q} - \frac{y\zeta}{q^3}\right) - b_y \left(\frac{2\nu x\zeta}{\theta^2 q} + \frac{x\zeta}{q^3}\right) \\
\frac{\sigma_{xy}}{\sigma_0} &= b_x \frac{x\zeta}{\theta^2 q} \left(1 - \frac{2y^2}{\theta^2} - \frac{y^2}{q^2}\right) - b_y \frac{y\zeta}{\theta^2 q} \left(1 - \frac{2x^2}{\theta^2} - \frac{x^2}{\theta^2}\right) \\
\frac{\sigma_{xz}}{\sigma_0} &= -b_x \frac{xy}{q^3} + b_y \left(-\frac{\nu}{q} + \frac{x^2}{q^3}\right) - b_z \frac{y\zeta(1-\nu)}{\theta^2 q} \\
\frac{\sigma_{yz}}{\sigma_0} &= b_x \left(\frac{\nu}{q} - \frac{y^2}{q^3}\right) + b_y \frac{xy}{q^3} + b_z \frac{x\zeta(1-\nu)}{\theta^2 q}, \quad \text{where } \theta^2 = x^2 + y^2.
\end{aligned}
\tag{IV.36}
$$

The stress field about a straight dislocation segment is then given as

$$
\tilde{\sigma}_{\alpha\beta}(\boldsymbol{r}) = \sigma_{\alpha\beta}(\boldsymbol{r})\big|_{z'=+L/2} - \sigma_{\alpha\beta}(\boldsymbol{r})\big|_{z'=-L/2}, \tag{IV.37}
$$

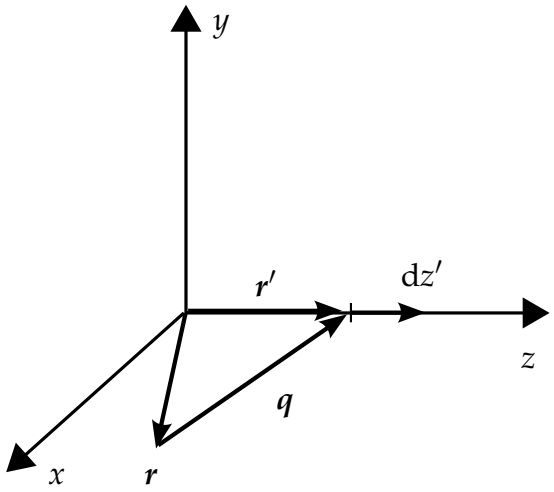

Figure IV.5: Local coordinates for a calculation of a stress field about a straight dislocation segment

where the components are substituted from (IV.35) or (IV.36). These components differ by integration constants, however, they provide a correct solution for the segment stress when substituted to (IV.37) since the integration constants are subtracted.

IV.3 Transformation of coordinates

The relations for the stress field of a straight dislocation segment presented in section IV.2.3 relate to a convenient local coordinate system (x, y, z) centered in the segment center with the z axis directed along the dislocation segment. To make use of these relations for an arbitrary dislocation configuration, a coordinate transformation is necessary.

Therefore, we introduce a global coordinate system is (X, Y, Z). We start with a straight dislocation segment i of length L_i centered at $\boldsymbol{R}_i$, whose Burgers vector is $\boldsymbol{b}_i$ and its direction is $\boldsymbol{\xi}_i$. To calculate a stress field of such dislocation segment at a point $\boldsymbol{R}_j$, we need to construct a local coordinate system (x_i, y_i, z_i). As only the direction of the z_i axis is known (given by the vector $\boldsymbol{\xi}_i$), the x_i and y_i axes are arbitrary, as long as they are perpendicular to each other and to z_i. We prefer following choice of the coordinate system:

$$\begin{aligned} \boldsymbol{z}_i &= \boldsymbol{\xi}_i, \\ \boldsymbol{y}_i &= \frac{\boldsymbol{z}_i \times \boldsymbol{b}_i}{|\boldsymbol{z}_i \times \boldsymbol{b}_i|}, \\ \boldsymbol{x}_i &= \frac{\boldsymbol{y}_i \times \boldsymbol{z}_i}{|\boldsymbol{y}_i \times \boldsymbol{z}_i|}. \end{aligned} \tag{IV.38}$$

In case of a screw dislocation segment, i.e. $\boldsymbol{b} \parallel \xi$, we take a cyclic permutation of the components of $\boldsymbol{b}$ in the cross product to acquire a non-zero vector perpendicular to $\boldsymbol{\xi}$.

The vectors $\boldsymbol{x}_i, \boldsymbol{y}_i, \boldsymbol{z}_i$ represent an orthonormal basis of the local coordinate system (x, y, z) and also a transformation operator $\hat{T}_i$ from the local coordinate system (x, y, z) to the global coordinate system (X, Y, Z). The inverse operator $\hat{T}_i^{-1}$ transforms a vector from (X, Y, Z) to (x, y, z):

$$\boldsymbol{U} = \hat{T}_i \boldsymbol{u}, \quad \boldsymbol{u} = \hat{T}_i^{-1} \boldsymbol{U}, \tag{IV.39}$$

where $\boldsymbol{U}$ and $\boldsymbol{u}$ represent the same vector, the former represented in the global and the latter in the local coordinate system. Starting from here, the vector quantities represented in global coordinates are denoted by bold uppercase letters, like $\boldsymbol{U}$, whereas their local coordinate associates by bold lowercase letters, like $\boldsymbol{u}$. The sole exception is the Burgers vector $\boldsymbol{b}$, whose local coordinate representation is denoted by $\hat{T}_i^{-1}\boldsymbol{b}$.

The stress field of a straight dislocation segment of length L_i evaluated in a point $\boldsymbol{r}_j$ is $\tilde{\sigma}(\boldsymbol{r}_j, L_i, \hat{T}^{-1}\boldsymbol{b})$, see Eq. (IV.35-IV.37) for a full form. The representation of the stress field in global coordinates is

$$\hat{\sigma}_{j,i}(\boldsymbol{R}_{j,i}, L_i, \boldsymbol{b}) = \hat{T}_i\tilde{\sigma}(\hat{T}_i^{-1}\boldsymbol{R}_{j,i}, L_i, \hat{T}_i^{-1}\boldsymbol{b})\hat{T}_i^{-1}, \tag{IV.40}$$

where $\boldsymbol{R}_{j,i} = \boldsymbol{R}_j - \boldsymbol{R}_i$.

IV.4 Peach-Koehler force

There are two distinct modes of dislocation motion in a crystal, glide (a conservative mode) or climb (a non-conservative mode). The glide motion breaks and re-establishes only bonds between neighbouring atoms. This process allows dislocations to move in a glide plane. During the glide motion, the crystal lattice changes that a superfluous atomic plane forming the edge dislocation is displaced by many atomic layers, but the individual atoms are only slightly shuffled.

The climb motion is caused by diffusion of interstitials and/or vacancies (sections I.2 and IV.5). The dislocation climb is thus connected with a transport of matter through the crystal lattice. The idea of a Peach-Koehler force, which causes a displacement of a dislocation, originates in the work connected with the transport of matter in the crystal lattice. The derivation is further described in the literature, see e.g. [6].

We consider a straight dislocation line of a mixed character with a unit direction vector $\boldsymbol{\xi}$ and a Burgers vector $\boldsymbol{b}$. The Burgers vector can be decomposed into an edge component $\boldsymbol{b}_e$ and a screw component $\boldsymbol{b}_s$. The glide plane of such dislocation is determined by its edge component and contains both the Burgers vector $\boldsymbol{b}$ and the direction vector $\boldsymbol{\xi}$. Screw dislocations, in principle, do not have a definite glide plane, even though crystallography still dictates a preferential glide planes for screw dislocations.

If the dislocation climbs over a distance δh perpendicular to the glide plane, an amount of matter per unit length must be removed:

$$\delta v = b_e \delta h. \tag{IV.41}$$

This can be expressed by vector notation:

$$\delta v = (\boldsymbol{\xi} \times \boldsymbol{b}) \cdot \delta \boldsymbol{r}, \tag{IV.42}$$

where the cross product is normal to the slip plane (its length denotes the edge component of the Burgers vector $\boldsymbol{b}_e$), so only the component of $\delta\boldsymbol{r}$ normal to the slip plane is important for the non-conservative motion. The situation is depicted in Fig. IV.6.

If the dislocation moves by $\delta\boldsymbol{r}$, a cut of an area $\boldsymbol{\xi} \times \delta\boldsymbol{r}$ is made per unit length. Then the material is removed uniformly over the cut (equation (IV.42)) and the material continuity needs to be restored. This is done by the displacement of the opposite surfaces of the

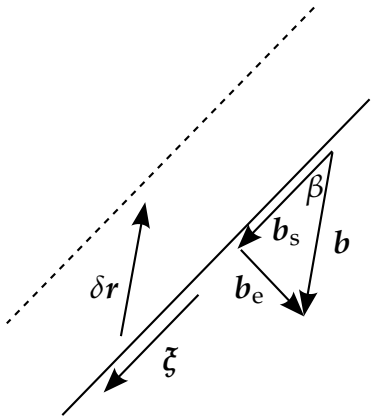

Figure IV.6: A mixed dislocation with direction $\boldsymbol{\xi}$ and Burgers vector $\boldsymbol{b}$ displaced by $\delta\boldsymbol{r}$.

cut by $\boldsymbol{b}$. If there is a uniform stress over the dislocation core, the work done by the operation is

$$\delta W = \boldsymbol{F} \cdot \delta\boldsymbol{r} = [\hat{\sigma} \cdot (\boldsymbol{\xi} \times \delta\boldsymbol{r})] \cdot \boldsymbol{b}, \tag{IV.43}$$

where the term $\hat{\sigma} \cdot (\boldsymbol{\xi} \times \delta\boldsymbol{r})$ denotes a force upon the surface $\boldsymbol{\xi} \times \delta\boldsymbol{r}$ originating in the stress $\hat{\sigma}$. Rewriting the equation (IV.43) gives

$$\boldsymbol{F} \cdot \delta\boldsymbol{r} = \boldsymbol{b} \cdot [\hat{\sigma} \cdot (\boldsymbol{\xi} \times \delta\boldsymbol{r})] = (\boldsymbol{b} \cdot \hat{\sigma}) \cdot (\boldsymbol{\xi} \times \delta\boldsymbol{r}) = [(\boldsymbol{b} \cdot \hat{\sigma}) \times \boldsymbol{\xi}] \cdot \delta\boldsymbol{r}. \tag{IV.44}$$

The force per unit length is called the Peach-Koehler force and is determined by the formula [6]:

$$\boldsymbol{F} = (\boldsymbol{b} \cdot \hat{\sigma}) \times \boldsymbol{\xi}. \tag{IV.45}$$

The force can be decomposed into a climb component

$$\boldsymbol{F}_\mathrm{C} = \frac{\boldsymbol{F} \cdot (\boldsymbol{b} \times \boldsymbol{\xi})}{(\boldsymbol{b} \times \boldsymbol{\xi})^2} (\boldsymbol{b} \times \boldsymbol{\xi}) \tag{IV.46}$$

and a glide component

$$\boldsymbol{F}_\mathrm{G} = \boldsymbol{F} - \boldsymbol{F}_\mathrm{C} = \frac{\boldsymbol{F} \cdot [\boldsymbol{\xi} \times (\boldsymbol{b} \times \boldsymbol{\xi})]}{(\boldsymbol{b} \times \boldsymbol{\xi})^2} [\boldsymbol{\xi} \times (\boldsymbol{b} \times \boldsymbol{\xi})]. \tag{IV.47}$$

IV.5 Dislocation climb rate

The non-conservative dislocation motion (climb) is a thermally activated process, which is very important for the high temperature plasticity. A derivation of dislocation climb velocity (climb rate) is presented in this chapter along lines discussed in [51].

It is assumed that the diffusion process is mediated by a flux of vacancies. The vacancy concentration field generally fulfils the first Fick's law [52]:

$$\frac{\partial c(\boldsymbol{r}, t)}{\partial t} = \nabla \cdot \boldsymbol{J}, \tag{IV.48}$$

where $\boldsymbol{J}$ is the vacancy flux determined by

$$\boldsymbol{J} = \frac{D_v(\boldsymbol{r}) c(\boldsymbol{r}, t)}{kT} \nabla \mu_v(\boldsymbol{r}, t), \tag{IV.49}$$

where μ_v is the vacancy chemical potential related to the local vacancy concentration and the elastic interaction energy within the crystal, k is Boltzmann's constant, T is the temperature and D_v is the vacancy diffusion coefficient dependent on the vacancy migration energy E_m:

$$D_v = D_v^0 \exp\left(-\frac{E_m}{kT}\right). \tag{IV.50}$$

In what follows, a solution to the diffusion vacancy field is given in a stress field of a dislocation. The solution is obtained under following assumptions [51]:

- The vacancy diffusion is fast compared to the velocity of dislocations. Therefore, the vacancy flux reaches a steady state at every time step and the left hand side of (IV.48) is zero.
- The elastic interaction energy between the dislocations and vacancies is neglected, the chemical potential of vacancies is then

$$\mu_v(\boldsymbol{r}) = kT \ln \frac{c(\boldsymbol{r})}{c_0}, \tag{IV.51}$$

  where c_0 is the equilibrium vacancy concentration at temperature T in a crystal free of defects; c_0 is determined by a vacancy formation energy E_f

$$c_0 = \frac{1}{\Omega} \exp\left(-\frac{E_f}{kT}\right). \tag{IV.52}$$

- The diffusion coefficient is constant throughout the crystal and independent of time.
- Any point along the dislocation may act as a vacancy source or sink.

A substitution of the equation (IV.49) into (IV.48) with the above assumptions yields a Laplace's equation:

$$\Delta c(\boldsymbol{r}) = 0. \tag{IV.53}$$

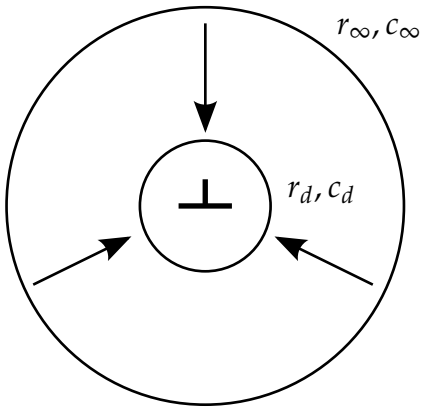

Figure IV.7: A cylindrical volume containing a dislocation line. The vacancy flux direction is indicated by the arrows.

The solution considers a cylindrical volume around a unit length of the dislocation line (see Fig. IV.7). The dislocation climb velocity is to be calculated. The inner radius r_d is approximately of the order of the dislocation core radius (i.e. $r_d \sim r_C$). Since dislocations are perfect sinks or sources of vacancies, the concentration of the vacancies should be in equilibrium with the dislocation near the dislocation core [6]:

$$c_d = c_0 \exp\left(\frac{F_C \Omega}{bkT}\right). \tag{IV.54}$$

There F_C is the climb component of the Peach-Koehler force (section IV.4), Ω is the atomic volume and b_e is the length of the edge component of the Burgers vector. The outer radius r_∞ of the cylindrical volume exhibits a vacancy concentration c_∞ characteristic for the bulk crystal. The boundary condition is thus $c(r_\infty) = c_\infty$.

As the concentrations do not depend on the angle or the position along the dislocation line, the differential equation for the vacancy concentration (IV.53) reduces to an ordinary differential equation:

$$\frac{1}{r}\frac{\partial}{\partial r}\left(r\frac{\partial c(r)}{\partial r}\right) = 0. \tag{IV.55}$$

According to [51], the solution is

$$c(r) - c_\infty = \frac{c_\infty - c_d}{\ln r_\infty / r_d} \ln \frac{r}{r_\infty}. \tag{IV.56}$$

Substituting the result to (IV.49), we obtain the vacancy flux:

$$J(\boldsymbol{r}) = -D_v \frac{\partial c(\boldsymbol{r})}{\partial r} = -\frac{D_v(c_\infty - c_d)}{r \ln(r_\infty / r_d)}. \tag{IV.57}$$

If we assume that each segment is a perfect sink of vacancies and there is no pipe diffusion, then the number of vacancies diffusing in or out from the dislocation core per unit length and time determine the climb velocity [51]:

$$v_C = \eta_v \frac{D_s}{b}\left[\exp\left(\frac{F_C \Omega}{bkT}\right) - \frac{c_\infty}{c_0}\right], \tag{IV.58}$$

where $D_s = f D_v c_0 \Omega$ is the solvent self-diffusion coefficient and $\eta_v = 2\pi/[f \ln(r_\infty / r_d)]$ is a geometrical factor of the flux field and the lattice structure and f is the Bardeen-Herring correlation factor for solvent diffusion. Considering the product $D_v c_0 \Omega$, the self-diffusion coefficient may be rewritten as

$$D_s = D_s^0 \exp\left(-\frac{E_{\text{act}}}{kT}\right) = D_s^0 \exp\left(-\frac{Q}{RT}\right), \tag{IV.59}$$

where $D_s^0 = f D_v^0$, E_{act} or Q is the activation energy for vacancy self-diffusion, the latter being a molar quantity. The symbol R represents the universal gas constant. The equation (IV.58) can be interpreted as a superposition of a force-dependent flux from the dislocation to the bulk and an absorption from the bulk to the dislocation. When the vacancy concentration c_∞ is close to the equilibrium (no under- or supersaturation), i.e. $c_\infty \approx c_0$, the climb forces are small, the climb velocity may be approximated as

$$v_C = B F_C, \quad B = \eta_v \frac{D_s \Omega}{b^2 kT}, \tag{IV.60}$$

as the dimensionless factor in the exponential term of equation (IV.58) is small.

IV.6 Dislocation interactions

IV.6.1 Infinite straight dislocation

The relation (IV.37) for the stress field due to a straight dislocation segment can be also used to compute a stress field of an infinite dislocation.

The stress field about a straight segment is calculated using the relation (IV.37). To determine the limits $\lim_{L\to\infty} \tilde{\sigma}_{ij}$, we use the components in the form (IV.36), which are suitable for the limiting operation $L \to \infty$. We recall the substitutions $\zeta = z' - z$, $\theta^2 = x^2 + y^2$ and $q^2 = \theta^2 + \zeta^2$. Following limits are necessary for the calculation (here $l = L/2$):

$$\begin{aligned}\left.\frac{\zeta}{q}\right|_{z'=l} - \left.\frac{\zeta}{q}\right|_{z'=-l} &= \frac{l-z}{[\theta^2+(l-z)^2]^{\frac{1}{2}}} + \frac{l+z}{[\theta^2+(l+z)^2]^{\frac{1}{2}}} = \\ &= \frac{(l-z)l\left[\left(\frac{\theta}{l}\right)^2+\left(1+\frac{z}{l}\right)^2\right]^{\frac{1}{2}} + (l+z)l\left[\left(\frac{\theta}{l}\right)^2+\left(1-\frac{z}{l}\right)^2\right]^{\frac{1}{2}}}{l^2\left\{\left(\frac{\theta}{l}\right)^4+\left[1-\left(\frac{z}{l}\right)^2\right]^2+\left(\frac{\theta}{l}\right)^2\left[1+\left(\frac{z}{l}\right)^2\right]\right\}^{\frac{1}{2}}}\end{aligned} \tag{IV.61}$$

Taking the limit $l \to \infty$, only the l^2 terms in the numerator of the fraction (IV.61) won't be cancelled. As a result, we have

$$\lim_{l\to\infty}\left(\left.\frac{\zeta}{q}\right|_{z'=l} - \left.\frac{\zeta}{q}\right|_{z'=-l}\right) = 2. \tag{IV.62}$$

Using the same approach, we may evaluate a limit of similar term:

$$\lim_{l\to\infty}\left(\left.\frac{\zeta}{q^3}\right|_{z'=l} - \left.\frac{\zeta}{q^3}\right|_{z'=-l}\right) = \frac{(l-z)l^3\left[\cdots\right]^{\frac{3}{2}} + (l+z)l^3\left[\cdots\right]^{\frac{3}{2}}}{l^6\left\{\cdots\right\}^{\frac{3}{2}}} = 0. \tag{IV.63}$$

Thus we get the components of the stress field generated by an infinite straight dislocation:

$$\begin{aligned}\sigma_{xx} &= -\frac{\mu}{2\pi(1-\nu)}\left[\frac{b_x y(3x^2+y^2)}{(x^2+y^2)^2} + \frac{b_y x(y^2-x^2)}{(x^2+y^2)^2}\right] \\ \sigma_{yy} &= \frac{\mu}{2\pi(1-\nu)}\left[\frac{b_x y(x^2-y^2)}{(x^2+y^2)^2} + \frac{b_y x(3y^2+x^2)}{(x^2+y^2)^2}\right] \\ \sigma_{xy} &= \frac{\mu}{2\pi(1-\nu)}\frac{(b_x x + b_y y)(x^2-y^2)}{(x^2+y^2)^2} \\ \sigma_{zz} &= -\frac{\mu\nu}{\pi(1-\nu)}\frac{b_x x + b_y y}{x^2+y^2} \\ \sigma_{xz} &= -\frac{\mu}{2\pi}\frac{b_z y}{x^2+y^2} \\ \sigma_{yz} &= \frac{\mu}{2\pi}\frac{b_z x}{x^2+y^2}\end{aligned} \tag{IV.64}$$

IV.6.2 Interaction between two dislocations

We use the stress field relations from the preceding section to study interactions between two parallel dislocations. First, we discuss parallel edge dislocations lying in different glide planes (Fig. IV.8) with $\boldsymbol{\xi} = (0,1,0)$ and $\boldsymbol{b} = (b,0,0)$. In the XZ plane, one dislocation is situated in the origin of the coordinate system, the other dislocation is in a point $[X,Z]$. We choose a local coordinate system with $\boldsymbol{x} = (1,0,0)$, $\boldsymbol{y} = (0,0,-1)$ and $\boldsymbol{z} = (0,1,0)$. Then the X component of the Peach-Koehler force acting upon the dislocation at a point $[X,Z]$ is

$$F_X(X,Z) = \frac{\mu}{2\pi(1-\nu)} \frac{b^2 X(X^2-Z^2)}{(X^2+Z^2)^2}. \tag{IV.65}$$

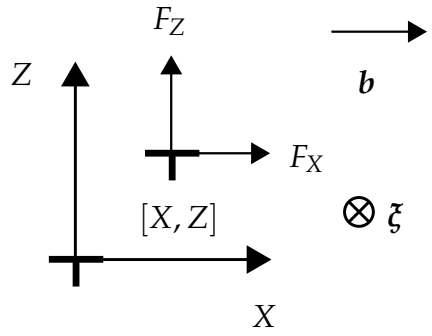

Figure IV.8: Interaction between two parallel edge dislocations.

Two plots of the force as a function of the coordinates $[X,Z]$ are shown in Fig. IV.9. The forces are calculated for $\mu = 80$ GPa, $\nu = 0.3$ and $b = 0.2$ nm. The first plot in Fig. IV.9a shows that for $X/Z = 1$ the F_X component of the Peach-Koehler force is zero, i.e. dislocations situated along a line $X = Z$ are in an unstable equilibrium. If the dislocation at $[X,Z]$ is displaced closer to the dislocation at $[0,0]$, the F_X component of the driving force becomes attractive, whereas when it is displaced away, the driving force becomes repulsive. If the dislocation is located at $[0,Z]$, the F_X component is also zero. However, this position is stable, because the F_X component always points in an opposite direction upon a displacement of the dislocation.

For a case of two antiparallel dislocations (i.e. with an opposite sign), which form a dislocation dipole, the driving force has a reversed direction. This makes the position along a line $X = Z$ stable and the position at $[0,Z]$ unstable.

As the edge dislocations move faster in glide planes than by climbing, the F_X component is, particularly at low temperatures, more important than F_Z. In conclusion, the force component F_X is responsible for the formation of low-angle tilt boundaries consisting of edge dislocations of the same sign.

For a case of two parallel dislocations in the same glide plane, we insert $Z = 0$ in the relation (IV.65). This gives

$$F_X = \frac{\mu}{2\pi(1-\nu)} \frac{b^2}{X}. \tag{IV.66}$$

The interaction between two parallel edge dislocations of the same sign in a common glide plane is always repulsive. On the other hand, two dislocations of an opposite sign are always attracted to each other, which allows them to annihilate.

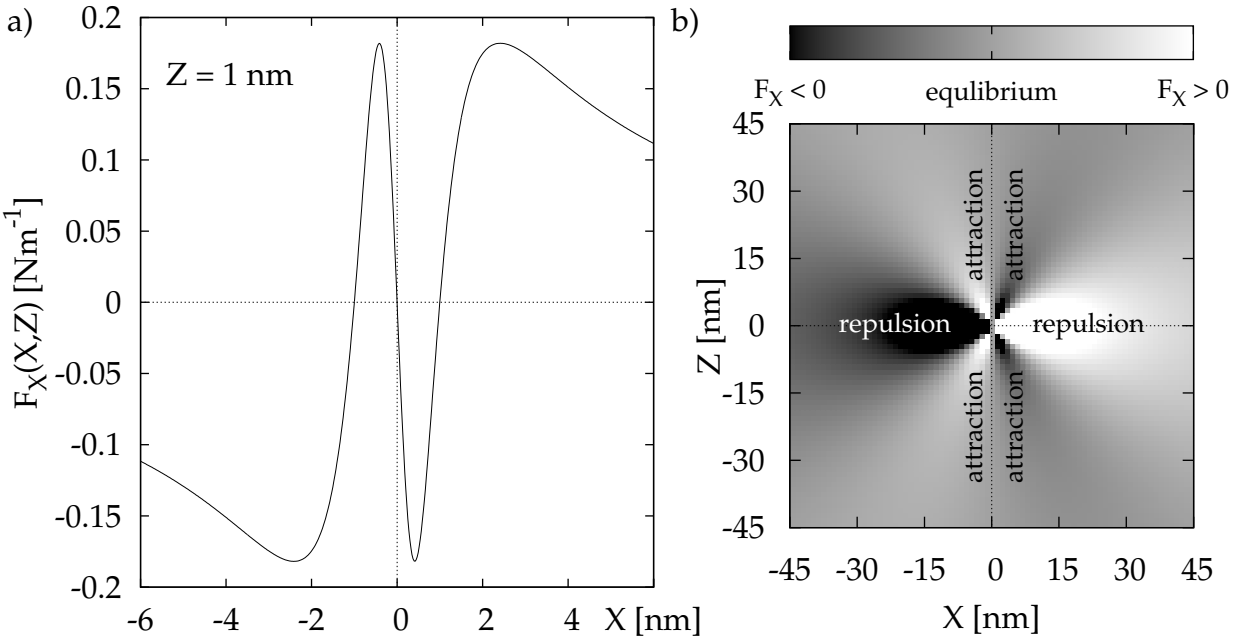

Figure IV.9: Force between two parallel edge dislocations.

On the other hand, two parallel screw dislocations have a different behaviour. If we retain the geometry from Fig. IV.8 and set $\boldsymbol{b} = (0, b, 0)$, we have

$$F_X(X, Z) = \frac{\mu}{2\pi} \frac{b^2 X}{X^2 + Z^2}. \tag{IV.67}$$

The equation (IV.67) shows that two parallel screw dislocations repel each other if they have the same sign and vice versa. Such a kind of interaction does not lead neither to a spontaneous formation of a dislocation boundary, nor to its stabilisation, if it already exists.

IV.6.3 Low-angle dislocation boundary

Now we will investigate an interaction between a low-angle tilt boundary (LATB) and a single edge dislocation. The geometry depicted in the XZ plane perpendicular to dislocation lines is shown in Fig. IV.10. The boundary consists initially of 6 edge dislocations separated by a distance h.

There is a single edge dislocation out of the tilt boundary situated at $[X, 0]$. The force acting upon this dislocation is determined by a sum

$$F_X^{\mathrm{LATB}}(X, Z) = \sum_{i=-3}^{2} F_X \left(X, Z + \frac{2i+1}{2} h \right). \tag{IV.68}$$

A plot of $F_X^{\mathrm{LATB}}(X, 0)$ is in Fig. IV.11a. Like in the case with two parallel dislocations, the forces are calculated for $\mu = 80$ GPa, $\nu = 0.3$ and $b = 0.2$ nm. The distance between the dislocations in the LATB was $h = 20$ nm. The first plot in Fig. IV.11a resembles the plot of the interaction force between two edge dislocations (Fig. IV.9a). Again, there is a region near the dislocation boundary, where the dislocation line is attracted, but further away from the boundary it is repelled. For an edge dislocation situated in a general point

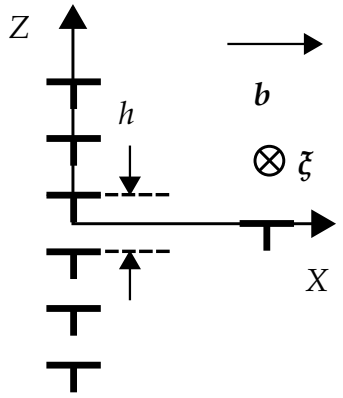

Figure IV.10: Interaction between an edge dislocation and a low-angle tilt boundary.

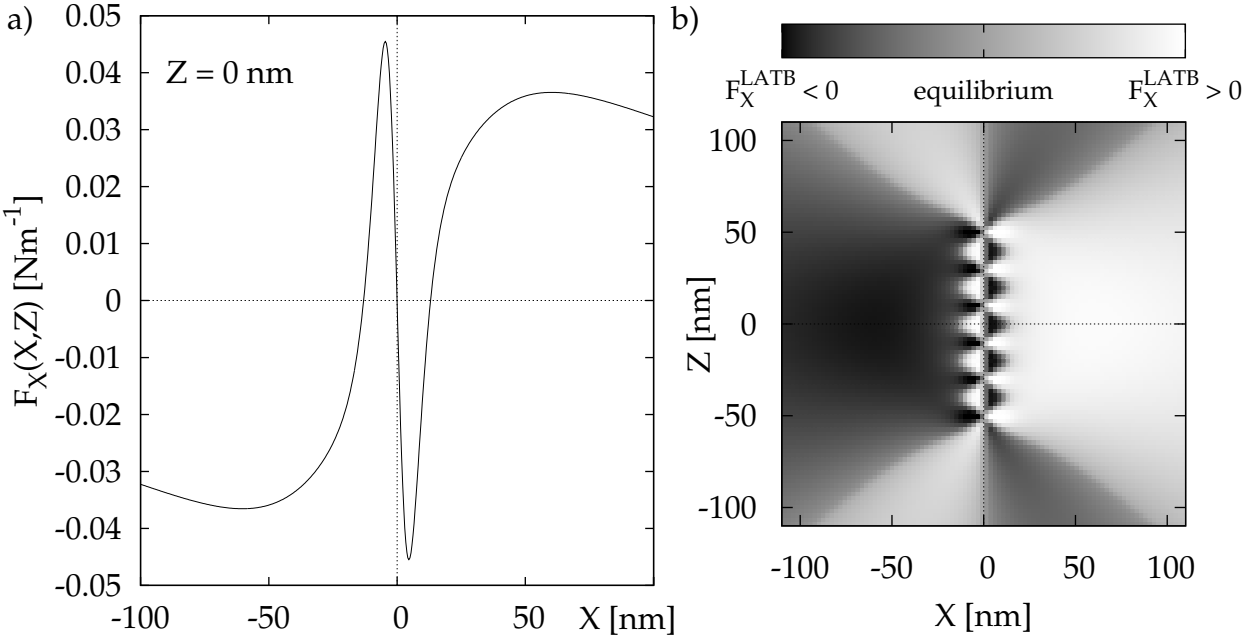

Figure IV.11: Force between a low-angle tilt boundary and a probe edge dislocation: a) at $[X, 0]$, b) at $[X, Z]$.

$[X, Z]$ near the tilt boundary, a force map is presented in Fig. IV.11b. The light regions represent positive values of the driving force upon the dislocation. The dark regions represent negative values of the driving force which pushes the probe dislocation to the left. The Fig. IV.11b shows that there are regions of attraction located between individual lines of the boundary, whereas dislocations sharing the glide planes with the boundary dislocations are rejected. For large distances from the boundary, we take the following limit:

$$\lim_{(X^2+Z^2)\to\infty} F_X^{\mathrm{LATB}}(X,Z) \sim F_X(X,Z). \tag{IV.69}$$

This means that the line $X = Z$ again delimits the regions of attraction and repulsion of the dislocation outside the tilt boundary.

A low-angle dislocation boundary consisting of screw dislocations is analogous to the low-angle tilt boundary described above. As indicated by relation (IV.67) and the plots in Fig. IV.12), such dislocation structure is not stable. The calculation parameters

and the geometry is the same except the Burgers vector, which is set to $\boldsymbol{b} = (0, b, 0)$.

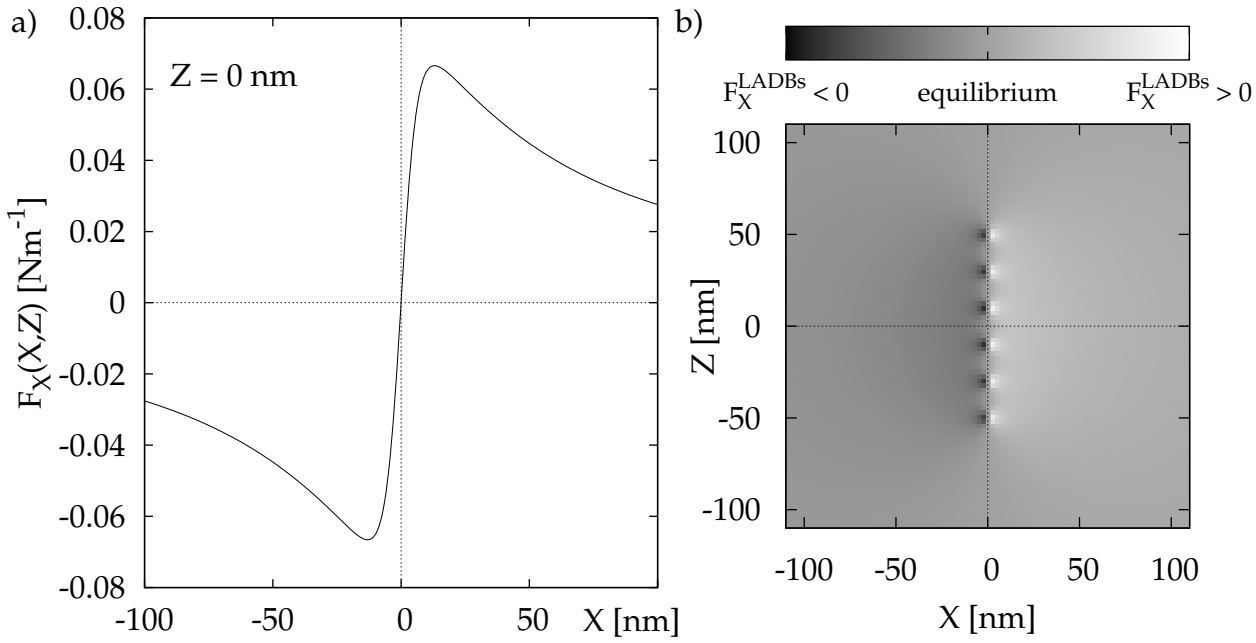

Figure IV.12: Force between a low-angle dislocation boundary consisting of screw dislocations and a probe screw dislocation: a) at $[X, 0]$, b) at $[X, Z]$.

IV.7 Calculation of strain from a dislocation displacement

A displacement of a dislocation generates permanent strain (plastic deformation) of the crystal lattice. Here we calculate this strain for a dislocation motion in one particular glide system. Let's turn back to the strain tensor ε_{ij} (section III.5). A Fig. IV.13 shows a prism (solid line), which is deformed to a parallelepiped (dashed line). The coordinate system is (x_1, x_2, x_3). Following the steps in the section III.5, we will study a displacement at particular points O, A_1 and A_2. The point vectors are $\boldsymbol{r}_O, \boldsymbol{r}_{A_1}$ and $\boldsymbol{r}_{A_2}$. Then $\boldsymbol{u}(\boldsymbol{r}_O) = (0, 0, 0)$, $\boldsymbol{u}(\boldsymbol{r}_{A_1}) = (0, \delta_1, 0)$ and $\boldsymbol{u}(\boldsymbol{r}_{A_2}) = (\delta_2, 0, 0)$. If we set $a_1 = |OA_1|$ and $a_2 = |OA_2|$, we may write:

$$\frac{\Delta u_1}{\Delta x_2} = \frac{\delta_1}{a_1} = \operatorname{tg} \gamma_{12}, \quad \frac{\Delta u_2}{\Delta x_1} = \frac{\delta_2}{a_2} = \operatorname{tg} \gamma_{21}. \tag{IV.70}$$

If the size of the prism in Fig. IV.13 approaches zero, the differentials in the equation (IV.70) turn into derivatives, giving

$$\frac{\partial \boldsymbol{u}_i}{\partial x_j} = \operatorname{tg} \gamma_{ij} \approx \gamma_{ij}, \quad i \neq j. \tag{IV.71}$$

For small deformations, the shear components of the strain tensor correspond to shear angles depicted in Fig. IV.13[1]. Thus we can put

$$\varepsilon_{ij} = \operatorname{tg} \gamma_{ij} \approx \gamma_{ij}. \tag{IV.72}$$

[1]The shear angle is often defined as a change of an angle between two directions in the material before and after the deformation, in this case $\alpha_{12} = |\sphericalangle A_1 O A_2| - |\sphericalangle A_1' O' A_2'| = 2\gamma_{12}$. For small deformations, $\sin \alpha_{ij} \approx \alpha_{ij} = 2\varepsilon_{ij}$ [7].

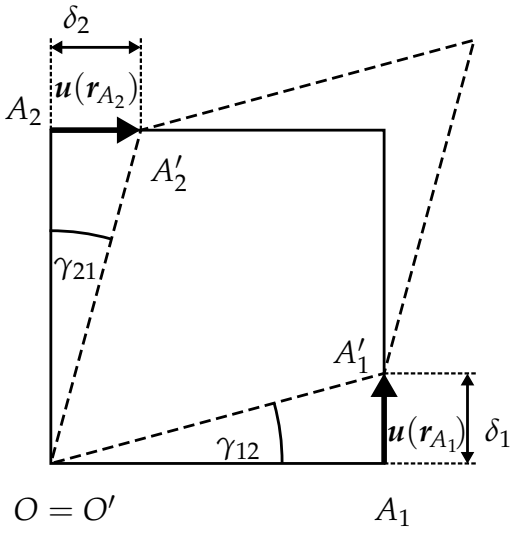

Figure IV.13: Meaning of the shear components of the strain tensor.

This idea allows to estimate shear strain due to the propagation of dislocation boundary in a crystal. Assume we have a dislocation boundary consisting of edge dislocations with a Burgers vector $\boldsymbol{b}$ and with a spacing h between the lines. When a single dislocation line of the dislocation boundary with a Burgers vector $\boldsymbol{b}$ moves through a particular volume of the crystal lattice, the material under and above the glide plane is shifted by a distance equal to the length of the Burgers vector $|\boldsymbol{b}|$. The strain accumulated by this displacement is

$$\varepsilon = \frac{b}{h}. \tag{IV.73}$$

If the whole dislocation boundary consisting of m dislocation moves through a particular volume of the crystal, the strain is $\varepsilon = mb/mh$, which is the same result.

If we consider a single dislocation segment with a direction vector $\boldsymbol{\xi}_i$ and a length L_i which is displaced by a vector $\Delta\boldsymbol{R}_i$, the area swept by the segment is $A_i = L_i|\boldsymbol{\xi}_i \times \Delta\boldsymbol{R}_i|$. The area of the projection of the crystal to the slip plane is A_0. The strain coming from a single dislocation segment is then

$$\varepsilon_i = \frac{A_i}{A_0}\frac{b_i}{h_i}, \tag{IV.74}$$

where b_i is the magnitude of the Burgers vector $\boldsymbol{b}_i$ of the particular segment and h_i delimits the volume displaced by the dislocation. Summing all dislocation segments gives

$$\varepsilon = \sum_i^N \frac{L_i|\boldsymbol{\xi}_i \times \Delta\boldsymbol{R}_i|b_i}{V}, \tag{IV.75}$$

where V is the crystal volume. If all the lines have the same Burgers vector, introducing an average displacement per dislocation segment $\overline{R}$ allows to rewrite (IV.75) to

$$\varepsilon = \rho b\overline{R}, \tag{IV.76}$$

which is the Orowan equation of the accumulated strain due to dislocation motion [1].

V. Fundamentals of the model

The presented model approximates a smooth dislocation curve by a continuous polygonal chain, which consists of straight segments. This greatly simplifies formulas for the Peach-Koehler force or stress field at the cost of high number of line segments. The linear theory of elasticity allows to sum up contributions from individual segments, which compose Peach-Koehler force per unit length of a dislocation line. Displacement of each segment is calculated from a mobility function which combines appropriate component of the Peach-Koehler force and a mobility parameter. The new coordinates are obtained when the displacement is added to the current segment position.

V.1 Stress field and force

Let $\boldsymbol{R}_i$ is the centre of an i-th segment in global coordinates (X, Y, Z). A contribution to stress field at $\boldsymbol{R}_j$ (centre of another segment) is computed in local coordinates (x_i, y_i, z_i) (Fig. V.1). Contributions from all segments (Eq. IV.40), whose number is N, are summed together (Fig. V.2), which leads to the internal stress due to dislocations:

$$\begin{aligned} \hat{\sigma}_j(\boldsymbol{R}_j, \{\boldsymbol{R}_i, L_i, \boldsymbol{b}_i\}) &= \sum_{i=1, i\neq j}^{N} \hat{\sigma}_{j,i}(\boldsymbol{R}_{j,i}, L_i, \boldsymbol{b}_i) = \sum_{i=1, i\neq j}^{N} \hat{T}_i \tilde{\sigma}(\hat{T}_i^{-1}\boldsymbol{R}_{j,i}, L_i, \hat{T}_i^{-1}\boldsymbol{b}_i)\hat{T}_i^{-1}, \\ \boldsymbol{R}_{j,i} &= \boldsymbol{R}_j - \boldsymbol{R}_i, \end{aligned} \tag{V.1}$$

following the ideas presented in section IV.3. The stress field is used to calculate the Peach-Koehler force (see Eq. (IV.45)):

$$\boldsymbol{F}_j = [\boldsymbol{b}_j \cdot \hat{\sigma}_j(\boldsymbol{R}_j, \{\boldsymbol{R}_i, L_i, \boldsymbol{b}_i\})] \times \boldsymbol{\xi}_j. \tag{V.2}$$

However, the linearity of the equations allow to interchange the order of computation of the Peach-Koehler force by the relation (IV.45) and the summation of contributions (V.1). This means we can evaluate a contribution to the total Peach-Koehler force acting on the j^{th} segment by substituting (IV.40) into (IV.45):

$$\boldsymbol{F}_{j,i}(\boldsymbol{R}_{j,i}, L_i, \boldsymbol{b}_j, \boldsymbol{b}_i) = [\boldsymbol{b}_j \cdot \hat{\sigma}_{j,i}(\boldsymbol{R}_j, L_i, \boldsymbol{b}_i)] \times \boldsymbol{\xi}_j = \left\{\boldsymbol{b}_j \cdot \left[\hat{T}_i \tilde{\sigma}(\hat{T}_i^{-1}\boldsymbol{R}_{j,i}, L_i, \hat{T}_i^{-1}\boldsymbol{b}_i)\hat{T}_i^{-1}\right]\right\} \times \boldsymbol{\xi}_j. \tag{V.3}$$

Therefore, the total Peach-Koehler force upon the j^{th} is computed as a summation of contributions (V.3):

$$\boldsymbol{F}_j(\boldsymbol{R}_j, b_j, \{\boldsymbol{R}_i, L_i, \boldsymbol{b}_i\}) = \sum_{i=1, i\neq j}^{N} \boldsymbol{F}_{j,i}(\boldsymbol{R}_{j,i}, L_i, \boldsymbol{b}_j, \boldsymbol{b}_i). \tag{V.4}$$

This approach is more complex than the summation of the stress fields, however, the force contributions show the same symmetry as the whole dislocation system. This is exploited for symmetry optimizations, which will be described further in section VI.9.

The linear combination in (V.1) does not include segment's own self-interaction, since the Peach-Koehler formula (IV.34) diverges with $q \to 0$. This stems from a fact, that the dislocation core is considered to be located sharp at the dislocation line itself. Actually, the dislocation core is distributed in a finite distance along a dislocation line. One solution of this problem is presented in the paper by Cai et al. [53]. The Burgers vector is spread in a tube-like volume about a dislocation line by a well-chosen distribution function. This choice allows to use the relations for stress field due to a straight dislocation segment in a form (IV.35) or (IV.36), only the distance term needs to be substituted: $q \to \sqrt{q^2 + r_C^2}$, where r_C is a dislocation core radius. This method is also described in [45]. This approach avoids divergent terms in (V.1) and (V.4). Thus an evaluation of self-interaction in the summation (V.1) is possible.

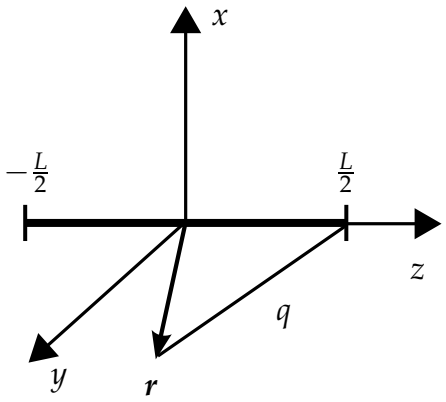

Figure V.1: A line segment extending from $z = -L/2$ to $z = +L/2$ and an associated local coordinate system.

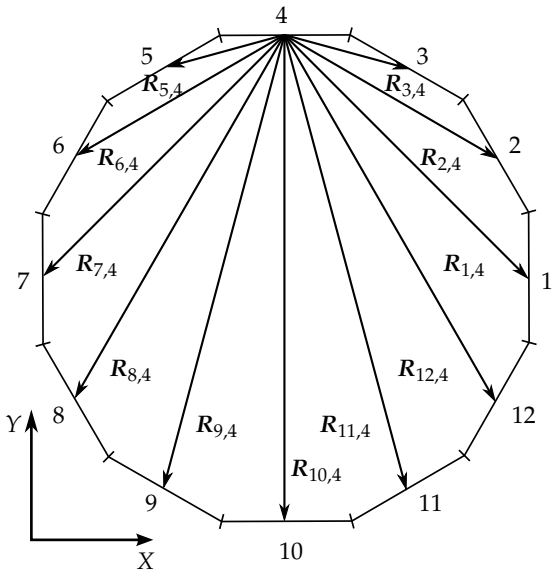

Figure V.2: Interaction between segments of a polygonal loop.

V.1.1 Line tension

Without the regularization based on finite dislocation core radius, the stress components diverge at a center of a particular segment, when the neighbouring segments are almost collinear. In such a case, the contributions from the nearest neighbours cannot be calculated according to the scheme presented in the section V.1. The missing contribution may be estimated by a line tension approximation.

The line tension energy according to [6, 12] is:

$$E_{\mathrm{LT}}(\rho_a) = \frac{\mu b^2}{4\pi(1-\nu)} \left[(1+\nu)\cos^2\beta + (1-2\nu)\sin^2\beta \right] \ln\frac{\rho_a}{r_C}, \tag{V.5}$$

where ρ_a is the arc radius and $\cos\beta = \boldsymbol{\xi} \cdot \boldsymbol{b}/|\boldsymbol{b}|$.

A derivative of the line tension energy with respect to ρ_a defines the line tension force:

$$F_{\mathrm{LT}} = \frac{\mu b^2}{4\pi\rho_a(1-\nu)} \left(1 - 2\nu + 3\nu\cos^2\beta \right). \tag{V.6}$$

The force is directed to the centre of curvature of the arc, which may be determined by a least-squares fit to a particular segment and it's two neighbours (4 vertices).

V.2 Equations of motion

Unlike the objects of classical mechanics, the dislocations do not have a mass and thus do not obey the Newton laws of motion. According to [6, 51], the climb velocity of a segment is given by a relation

$$v_{\mathrm{C}} = \frac{D_s \Omega}{b^2 kT} \frac{F_{\mathrm{C}}}{L} = B \frac{F_{\mathrm{C}}}{L}, \tag{V.7}$$

where Ω is a volume per atom, b is the length of the Burgers vector, k is the Boltzmann constant, T is the temperature and D_s is the self-diffusion coefficient, which can be approximated as

$$D_s = D_0 \mathrm{e}^{-\frac{Q}{RT}}, \tag{V.8}$$

where Q is the activation energy of self-diffusion, $R = kN_A$ is the universal gas constant and N_A is the Avogadro constant. The climb velocity is further discussed in section IV.5.

The glide movement is approximated by a similar linear function:

$$v_{\mathrm{G}} = A \frac{F_{\mathrm{G}}}{L}. \tag{V.9}$$

The movement in the slip plane is expected to be much faster than the climb, so we choose $A = 10B$ as a first order approximation.

The particular methods for a decomposition of the driving force $\boldsymbol{F} = \boldsymbol{F}_{\mathrm{G}} + \boldsymbol{F}_{\mathrm{C}}$ will be discussed later in section VI.2.

V.3 Time integration of the evolution equations

V.3.1 Euler forward integration

The investigated system of dislocation segments evolves in time in accord with acting driving forces.

The simplest way of time integration is a product of velocity and time step.

$$\boldsymbol{R}_i^{(n+1)} = \boldsymbol{R}_i^{(n)} + \boldsymbol{v}(\{\boldsymbol{R}_j^{(n)}\})\Delta t, \quad j \in \{1, \dots N\}. \tag{V.10}$$

The symbol $\boldsymbol{R}_i^{(n+1)}$ is a position of i-th segment's centre at $(n+1)$-th iteration, $\boldsymbol{v}(\{R_j^{(n)}\})$, $j \in \{1, \dots N\}$ means that the velocity v is a function of positions of all segments. The time step length is denoted by Δt. The Euler integration may not provide stable solutions particularly in cases when underlying functions are subjected to strong variation.

V.3.2 Trapezoid integration

The trapezoid integration

$$\boldsymbol{R}_i^{(n+1)} = \boldsymbol{R}_i^{(n)} + \left[\boldsymbol{v}(\{\boldsymbol{R}_j^{(n)}\}) + \boldsymbol{v}(\{\boldsymbol{R}_j^{(n+1)}\})\right] \frac{\Delta t}{2}, \quad j \in \{1, \dots N\} \tag{V.11}$$

largely overcomes weaknesses of the Euler integration. The trapezoid integration is much more stable, however, it is an implicit integration formula, which has $\boldsymbol{R}_i^{(n+1)}$ on both left and right side. Since the Peach-Koehler formula is rather complex to be inverted, we adopt an approximation – the Euler-trapezoid integration [45].

V.3.3 Euler-trapezoid integration

Let $\boldsymbol{R}_i^{(n+1),\mathrm{E}}$ is a result of (V.10). Then the trapezoid integration can be approximated by a relation:

$$\boldsymbol{R}_i^{(n+1),\mathrm{E-T}} = \boldsymbol{R}_i^{(n),\mathrm{E-T}} + \left[\boldsymbol{v}(\{\boldsymbol{R}_j^{(n),\mathrm{E-T}}\}) + \boldsymbol{v}(\{\boldsymbol{R}_j^{(n+1),\mathrm{E}}\})\right] \frac{\Delta t}{2}, \quad j \in \{1, \dots N\}. \tag{V.12}$$

The equations (V.10) and (V.12) form a pair of two explicit formulas with comparable accuracy with trapezoid integration at a cost of doubling the number of numerical operations needed to evaluate velocities $\boldsymbol{v}(\{\boldsymbol{R}_j^{(n),\mathrm{E-T}}\})$ and $\boldsymbol{v}(\{\boldsymbol{R}_j^{(n+1),\mathrm{E}}\})$.

This pair of formulas also allows to estimate integration error. This can be used to dynamically adjust the time integration step.

$$\delta_i = \frac{\boldsymbol{R}_i^{(n+1),\mathrm{E-T}} - \boldsymbol{R}_i^{(n+1),\mathrm{E}}}{\sum_{j=0}^{N} \left|\boldsymbol{R}_j^{(n+1),\mathrm{E-T}} - \boldsymbol{R}_j^{(n),\mathrm{E-T}}\right|}, \quad \begin{cases} \max\{\delta_i\} > \delta_{\max} \Rightarrow \Delta t^{(n+1)} = t_\downarrow \Delta t^{(n)}, \\ \max\{\delta_i\} \leq \delta_{\max} \Rightarrow \Delta t^{(n+1)} = t_\uparrow \Delta t^{(n)}. \end{cases} \tag{V.13}$$

The purpose of these relations is to keep a difference between the Euler forward and trapezoid integration methods (which is the estimation of the integration error) small with respect to an average segment displacement in the whole dislocation system. This is measured by the quantity $\delta_{\max}$. If the estimated integration error is small, the time integration step can be prolonged – scaled up by a factor $t_\uparrow$. A reasonable choice of the scaling factor is $t_\uparrow \in (1, 1.5)$. Larger values are not suitable, as they may increase the integration error too much. If the integration error is too high, the time step is scaled down by $t_\downarrow$. A reasonable choice is $t_\downarrow \in (0.3, 0.7)$, but any value smaller than 1 should work.

V.3.4 Runge-Kutta method of the 4th order

We may improve the integration accuracy even further using the Runge-Kutta method of 4th order. New coordinates are determined by the following set of equations:

$$
\begin{aligned}
\boldsymbol{R}_i^{(n+1)}(t+\Delta t) &= \boldsymbol{R}_i^{(n)}(t) + \frac{\Delta t}{6}\left(\boldsymbol{\Delta}_{i,1}^{(n)} + 2\boldsymbol{\Delta}_{i,2}^{(n)} + 2\boldsymbol{\Delta}_{i,3}^{(n)} + \boldsymbol{\Delta}_{i,4}^{(n)}\right), \\
\boldsymbol{\Delta}_{i,1}^{(n)} &= v\left(t, \{\boldsymbol{R}_j^{(n)}\}\right) \\
\boldsymbol{\Delta}_{i,2}^{(n)} &= v\left(t+\frac{\Delta t}{2}, \{\boldsymbol{R}_j^{(n)} + \frac{\Delta t}{2}\boldsymbol{\Delta}_{j,1}^{(n)}\}\right) \\
\boldsymbol{\Delta}_{i,3}^{(n)} &= v\left(t+\frac{\Delta t}{2}, \{\boldsymbol{R}_j^{(n)} + \frac{\Delta t}{2}\boldsymbol{\Delta}_{j,2}^{(n)}\}\right) \\
\boldsymbol{\Delta}_{i,4}^{(n)} &= v\left(t+\Delta t, \{\boldsymbol{R}_j^{(n)} + \Delta t\boldsymbol{\Delta}_{j,3}^{(n)}\}\right)
\end{aligned} \tag{V.14}
$$

V.4 New coordinates

V.4.1 Segment forces

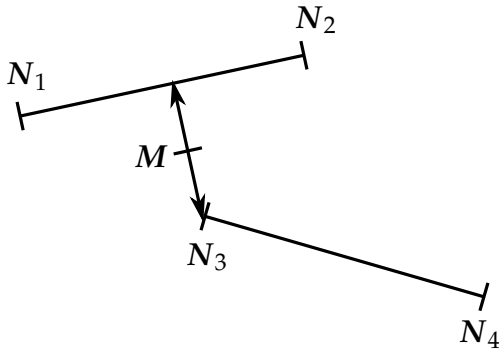

Figure V.3: The shortest distance between two segments.

Theory of dislocations [6] suggests how to calculate a Peach-Koehler force per unit length of a segment. In the presented model, this force is applied to a segment, which moves with a velocity given by formulas (V.7) and (V.9), (VI.6), (VI.11) or (VI.23). However, these displacements of individual segments may result in situations when the segments are neither connected by their endpoints, nor do they have an intersection. As a remedy of these disconnections, every two neighbouring segments are reconnected by a procedure depicted in Fig. V.3. At first it is necessary to find the shortest line connecting two adjacent segments. The midpoint denoted by the vector $\boldsymbol{M}$ is used as a new common endpoint of two adjacent segments, which were originally connected. This technique keeps the dislocation network continuous and allows the segments to rotate in each iteration.

Finally, the endpoints of the polygonal chain cannot be determined by this method. Either the endpoints are fixed due to the nature of the simulated process (e.g. Frank-Read source), or they are mobile, because they lie on a free surface, in a symmetry plane of the process, or at a boundary plane of the simulation cell (see sections VI.6 and VI.9). As a result, the direction of the mobile ending dislocation segment is considered fixed, which allows to compute the coordinates of the endpoints.

The algorithm is further illustrated in Fig. V.4, where three dislocation segments with endpoints denoted by vectors $\boldsymbol{N}_i^{(n)}$ are displaced due to driving forces (dashed segments in the figure). The segments are reconnected using the algorithm described above, which leads to new coordinates $\boldsymbol{N}_i^{(n+1)}$ for the next integration step.

V.4.2 Nodal forces

An alternative approach is based on nodal forces, which are computed as a weighted average of forces applied to segments connected in a node [45]:

$$
\boldsymbol{F}_{\mathrm{v}} = \frac{\sum_i \boldsymbol{F}_i L_i}{\sum_i L_i}, \tag{V.15}
$$

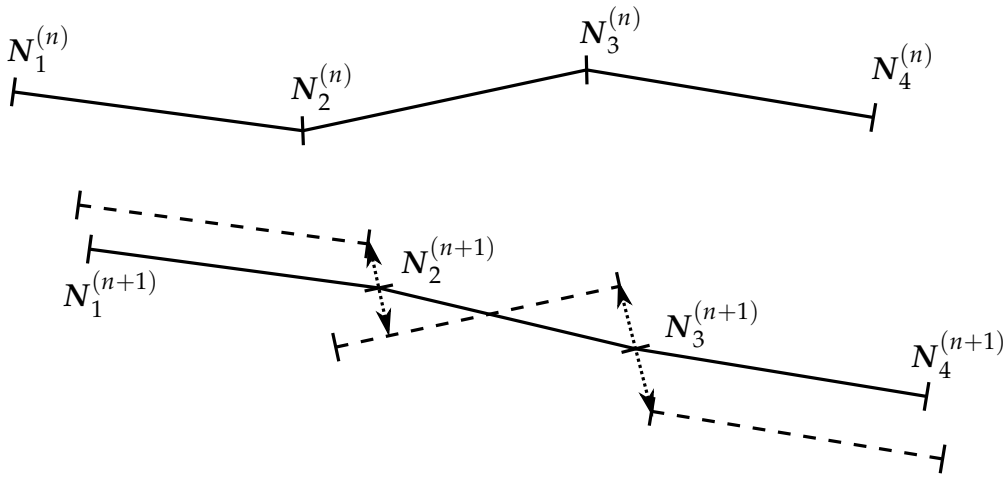

Figure V.4: Application of the algorithm for finding new coordinates to a set of 3 dislocation segments.

where $\boldsymbol{F}_i$ is a force applied to the segment of a length L_i with a centre at $\boldsymbol{R}_i$.

New coordinates can be computed straightforwardly, however, the glide and climb components cannot be separated, unless all segments connected to the node have common glide plane. This feature restricts this approach to planar processes.

V.5 Benchmarks (I.)

V.5.1 A single dislocation loop

The first benchmark simulation was focused on a single planar dislocation loop contracting due to its self-stress. The circular dislocation loop represented by a regular polygon is shown in Fig. V.5. Coordinates of the polygon vertices are:

$$\begin{aligned} \boldsymbol{N}_i &= (R\cos\varphi_i, R\sin\varphi_i, 0)\,, \\ \varphi_i &= \frac{2\pi[i-\frac{3}{2}]}{N}, \\ i &= 1,\ldots,N. \end{aligned} \tag{V.16}$$

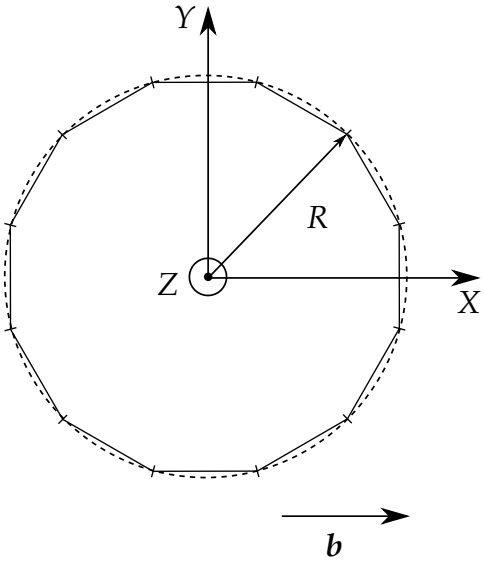

Figure V.5: A dislocation loop.

Material parameters μ, ν and $\boldsymbol{b}$, as well as the initial dislocation loop radius R, number of segments N and other input parameters are listed in the Table V.1.

In the following plots, segment positions are described by a polar angle φ, which determines the coordinate of a segment center: $\boldsymbol{R}_i = [a_i\cos\varphi_i, b_i\sin\varphi_i, 0]$. The simulation results are shown in Fig. V.6 The simulation starts with a circular loop of a diameter R (see Table V.1) and shrinks to a small elliptical loop (Fig. V.6a). Initially, the driving forces (the lowermost set of points in Fig. V.6b) acting on the screw segments ($\varphi \in \{\pi/2, 3\pi/2\}$ are considerably higher than those on the edge segments ($\varphi \in \{0, \pi\}$). Later, as the loop reshapes into an ellipse (the edge segments are perpendicular to the major axis of the ellipse), the local curvature at the edge segments is higher than at the screw segments. The driving forces acting on the edge segment thus grow faster than

Table V.1: Parameters of the simulation.

μ	$0.8 \cdot 10^{11}\ \mathrm{Nm}^{-2}$	shear modulus
ν	0.3	Poisson ratio
D_0	$2 \cdot 10^{-4}\ \mathrm{m}^2\mathrm{s}^{-1}$	diffusion factor for zero Q
Q	$240\ \mathrm{kJ\,mol}^{-1}$	activation energy of self-diffusion
T	873 K	temperature of simulate process
Ω	$(3.5 \cdot 10^{-10}\ \mathrm{m})^3$	atomic volume
$\boldsymbol{b}$	$(2,0,0) \cdot 10^{-10}\ \mathrm{m}$	Burgers vector
R	500 nm	initial dislocation loop radius
N	40	# of nodes of the approximating polygon
Δt	3 s	initial time step
Δt	$\langle 0.03, 5.00 \rangle$ s	time step range

in the case of screw segments (see the uppermost points in Fig. V.6b). The Figs. V.6c and d show, in a logarithmic scale, the force contribution from all of the segments upon two segments with prevailing screw character. It is obvious, that the major contribution comes from the nearest neighbours. Again, the forces are growing as the loop is shrinking.

The stability of the simulation for a particular dislocation strongly depends not only on the dislocation line geometry, but also on the discretisation and the integration time step. A set of simulations was performed to demonstrate these dependencies. These simulations started with the same parameters (Table V.1) except the number of segments, which was, respectively, 20, 40 and 80 in the simulation 1, 2 and 3. The forces on segments in the first 3 iterations are plotted in Fig. V.7. Again, the forces acting upon screw segments are higher than the forces acting upon the edge segments. However, it can be seen that the forces quickly start to oscillate, if the discretisation is too fine for the particular time step ($\Delta t = 3$ s).

V.5.2 Force analysis

As a benchmark calculation, a force analysis was performed for a single circular dislocation loop in the plane $Z = 0$ with radius R and a center at point $[0,0,0]$. Material parameters and the temperature are the same as in the preceding benchmark (see the Table V.1). The loop radius R and the number of segments N differs from the preceding calculation:

$$\begin{array}{rclcrcl} R & = & \dfrac{R_0}{k}, & & R_0 & = & 1000\ \mathrm{nm}, \qquad k \in \{1,2,4,\ldots,32\} \\ N & = & l\,N_0, & & N_0 & = & 40, \qquad\qquad\ \ l \in \{1,1.5,2,4,8,12,16\}. \end{array}$$

For given radius R and number of segments N, the initial segment length L is

$$L = 2R \sin\frac{\pi}{N} \approx \frac{2\pi R}{N}. \tag{V.17}$$

The Fig. V.8 shows that the edge segments at $\varphi \in \{0, \pi\}$ are acted on by a lower force than the screw segments at $\varphi \in \{\pi/2, 3\pi/2\}$. Furthermore, the force magnitude depends also on the segment length. A loop composed of shorter segments exhibits

a) Loop evolution, R = 500 nm, N = 40, Δt = 3 s,

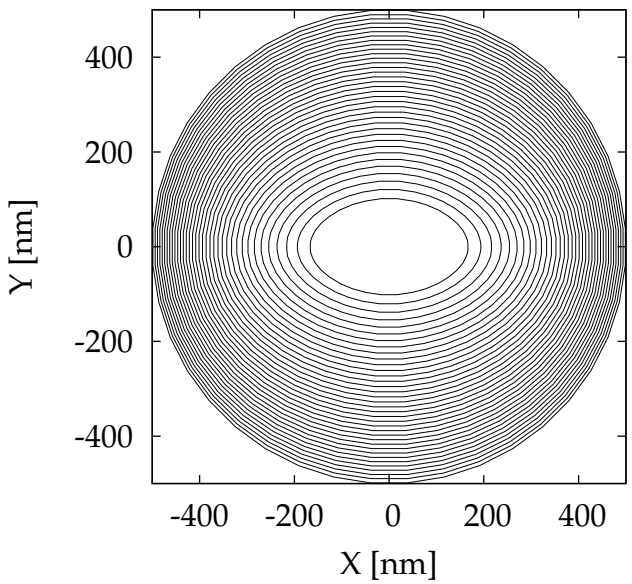

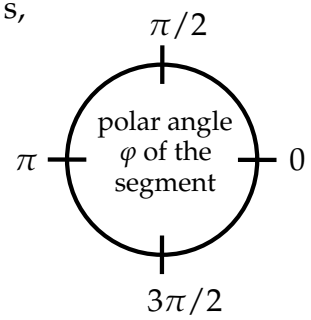

Figure V.6: Evolution of single loop using segment forces and Euler forward time integrator.

b) evolution of segment forces,

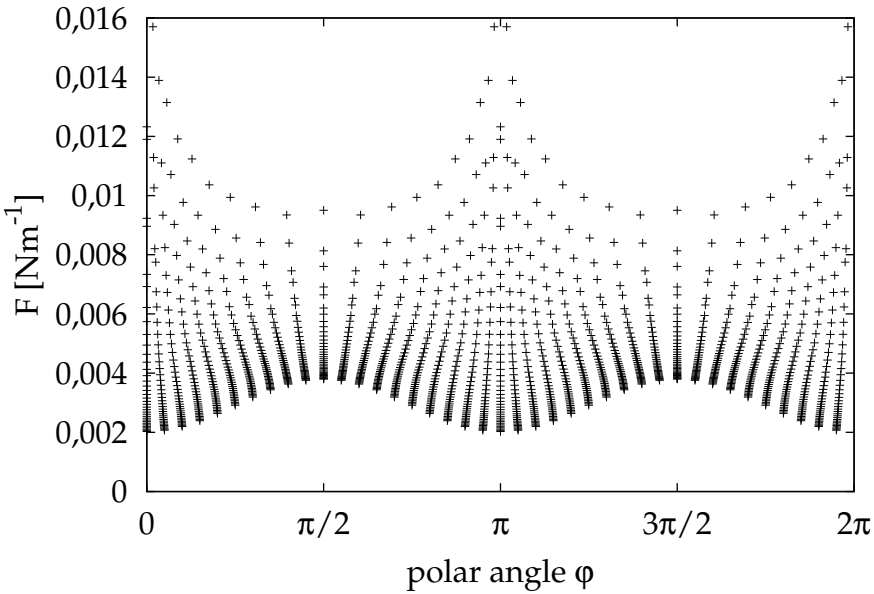

c) evolution of forces on segment φ = 9π/20,

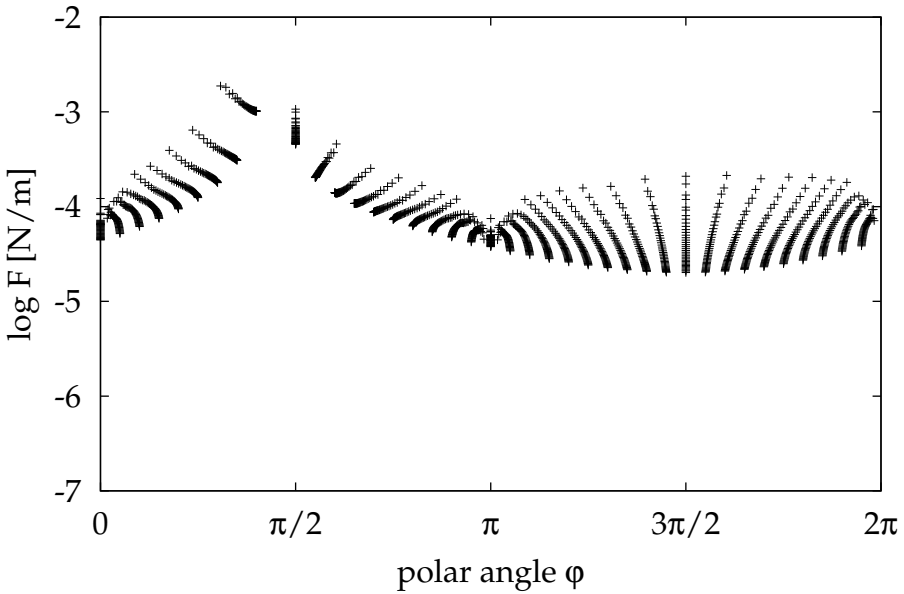

d) evolution of forces on segment φ = π/2.

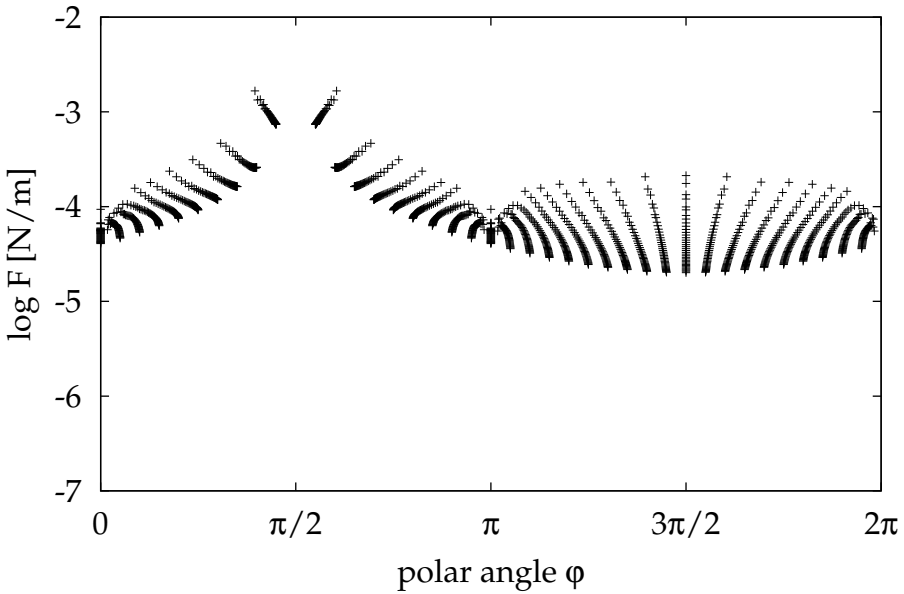

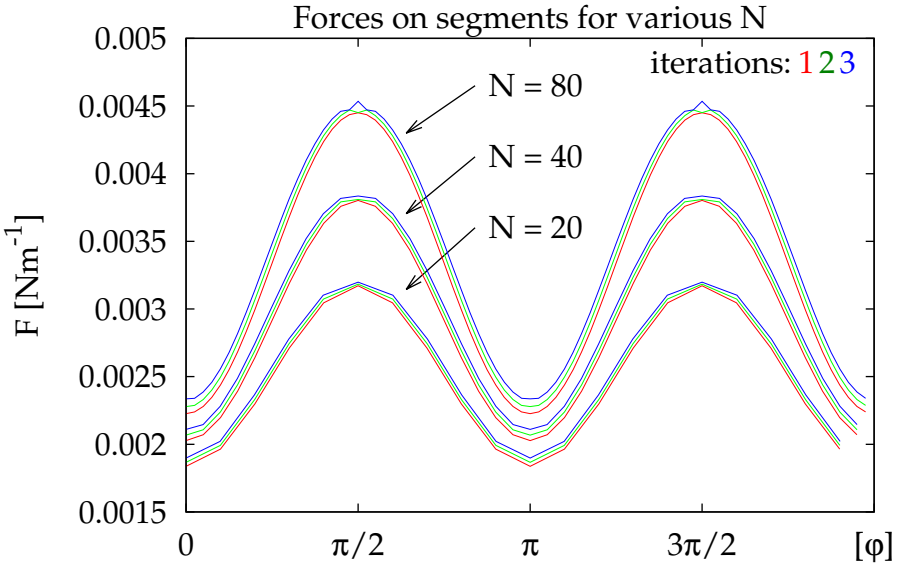

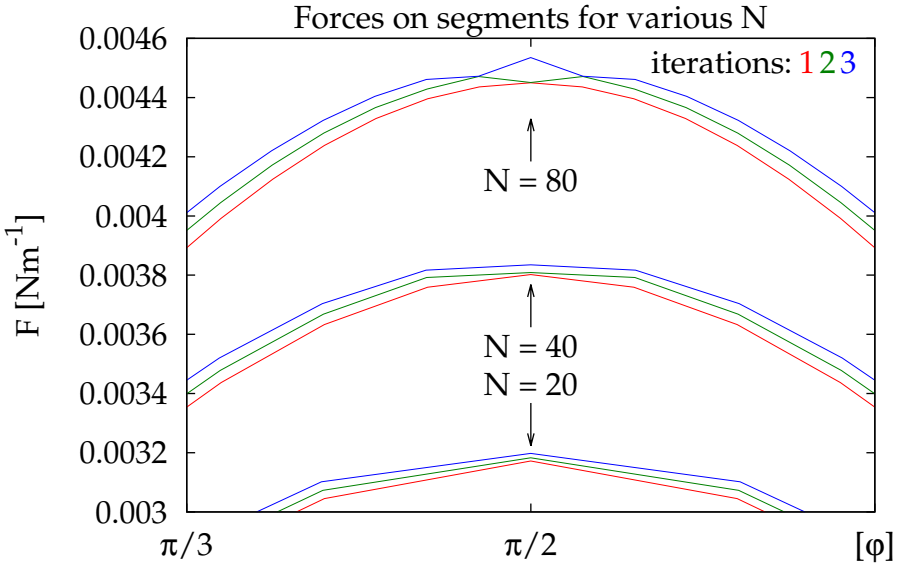

Figure V.7: Segment forces for various N. Graphs show first 3 steps, the forces grow monotonically with time. Time step: $\Delta t = 3$ s.

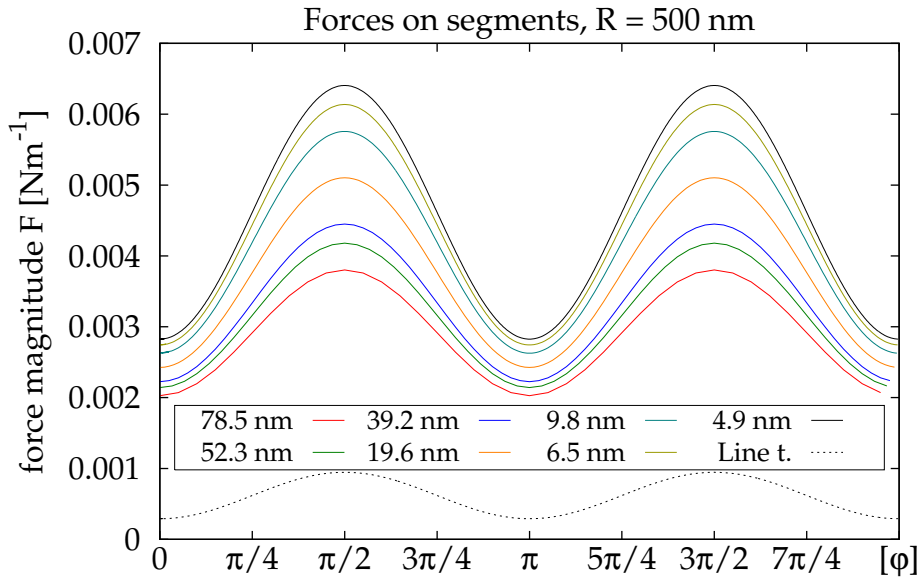

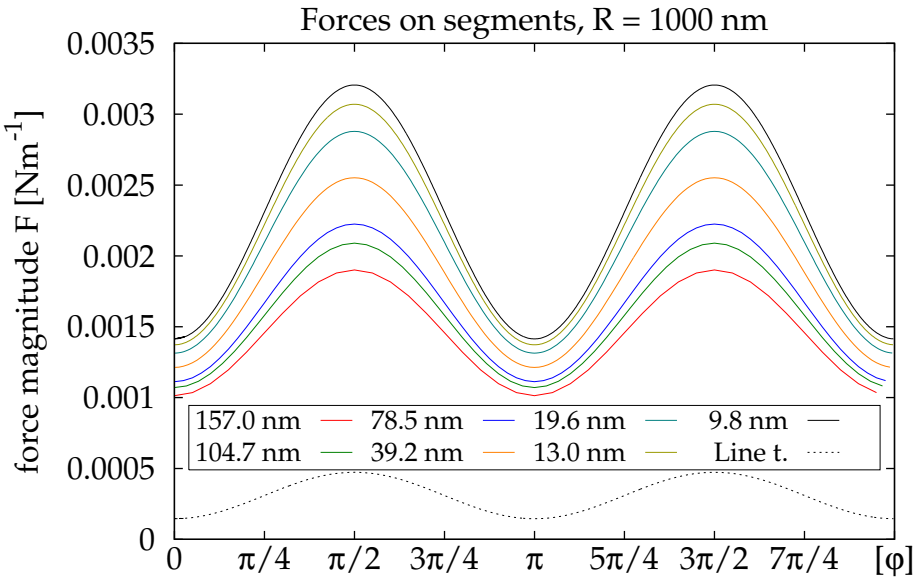

Figure V.8: Force magnitude vs. segment position, various radii R and segment lengths L.

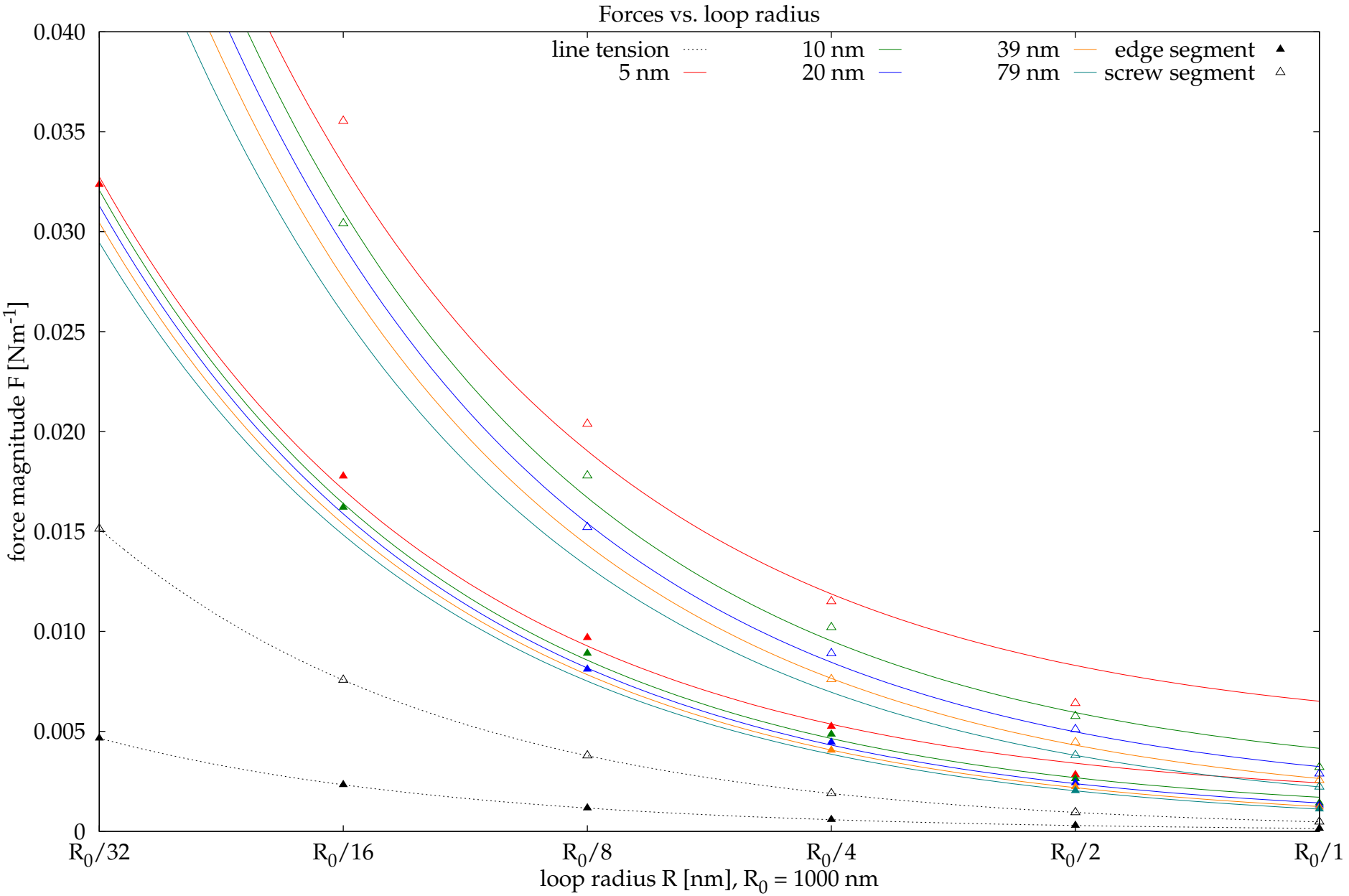

Figure V.9: Force magnitude vs. loop radius. Only pure edge and screw segments.

stronger self-stress. The forces depend also on the loop radius (Fig. V.9). We see that smaller loops have stronger self-stress than greater loops, because the distance between all the interacting segments is smaller.

Another benchmark calculation was focused on local stress contributions for an arc of length δR, where $\delta = 2\pi\frac{3}{N}$. This arc is a part of a circular dislocation loop with N segments described above. Initially, the arc is discretised with three dislocation segments of the same length corresponding to the number N. The arc discretisation is then consecutively refined to $2m + 1$ segments, where $m \in \{1, 2, \ldots, 8\}$. The arc is depicted in Fig. V.10.

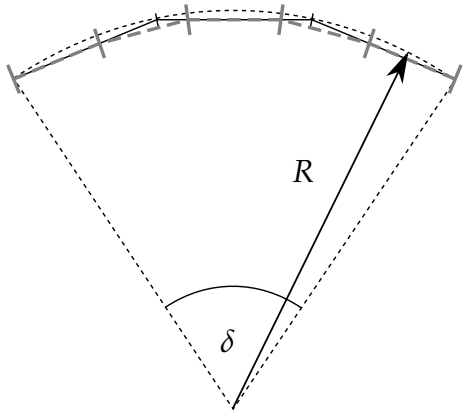

Figure V.10: An arc of length δR (dotted line), originally discretised with 3 segments (solid line) is replaced with $2m + 1$ segments (thick grey dashed line). Here $m = 2$.

A part of the driving force acting on the central arc segment due to interactions with all segments remaining inside the arc is calculated for different count of segments N and for several rediscretisations m of the arc. In every calculation, the central segment has $2m$ neighbours along the arc, which contribute to the total driving force. Such calculation is performed for all m-multiplets of segments along the initial circular loop. The results are summarized in Fig. V.11a. Like in the plots in Fig. V.7 and V.8, these contributions are higher for the screw segments ($\varphi \in \{\pi/2, 3\pi/2\}$) than for the edge segments ($\varphi \in \{0, \pi\}$). However, the magnitude of the force contribution exhibits only a weak dependence of the segment length L (on the initial discretisation of the loop N). On the other hand, a higher number of neighbours along the arc leads again to an increase of the force contribution. This is readable from the plots in Fig. V.11b, where δ is constant (i.e. N is constant), but the number of neighbouring segments $2m$ changes – it is inversely proportional to L on the horizontal axis in the plot in Fig. V.11b.

V.5.3 Self-stress of the dislocation loop

The first simulation addressed a contraction of a single circular dislocation loop driven by its self-stress. At first we focus on results with constant time integration step. The segment force approximation has been used. The simulation is stable in the first iterations, but as the self-forces increase with decreasing loop dimensions, the simulation starts to oscillate and finally breaks up at the regions of high curvature. The results are presented in Fig. V.12. The outer loop is the initial configuration, the inner loop shows the last stable iteration. Total time is $t = 90.3$ s.

The second simulation was performed with a variable time step $\Delta t \in \langle 0.03, 5.00 \rangle$ s with max. integration error $\rho_{\max} = 0.12$, see Eq. (V.13). The speedup factor was $t_{\uparrow} = 1.2$ and slowdown factor was $t_{\downarrow} = 0.5$. The results are shown at the Fig. V.13. The last iteration approaches the result of the simulation with the shortest constant time step, but the simulation required about 30 times less iterations to finish. However, the total time of the process increased by about 21%.

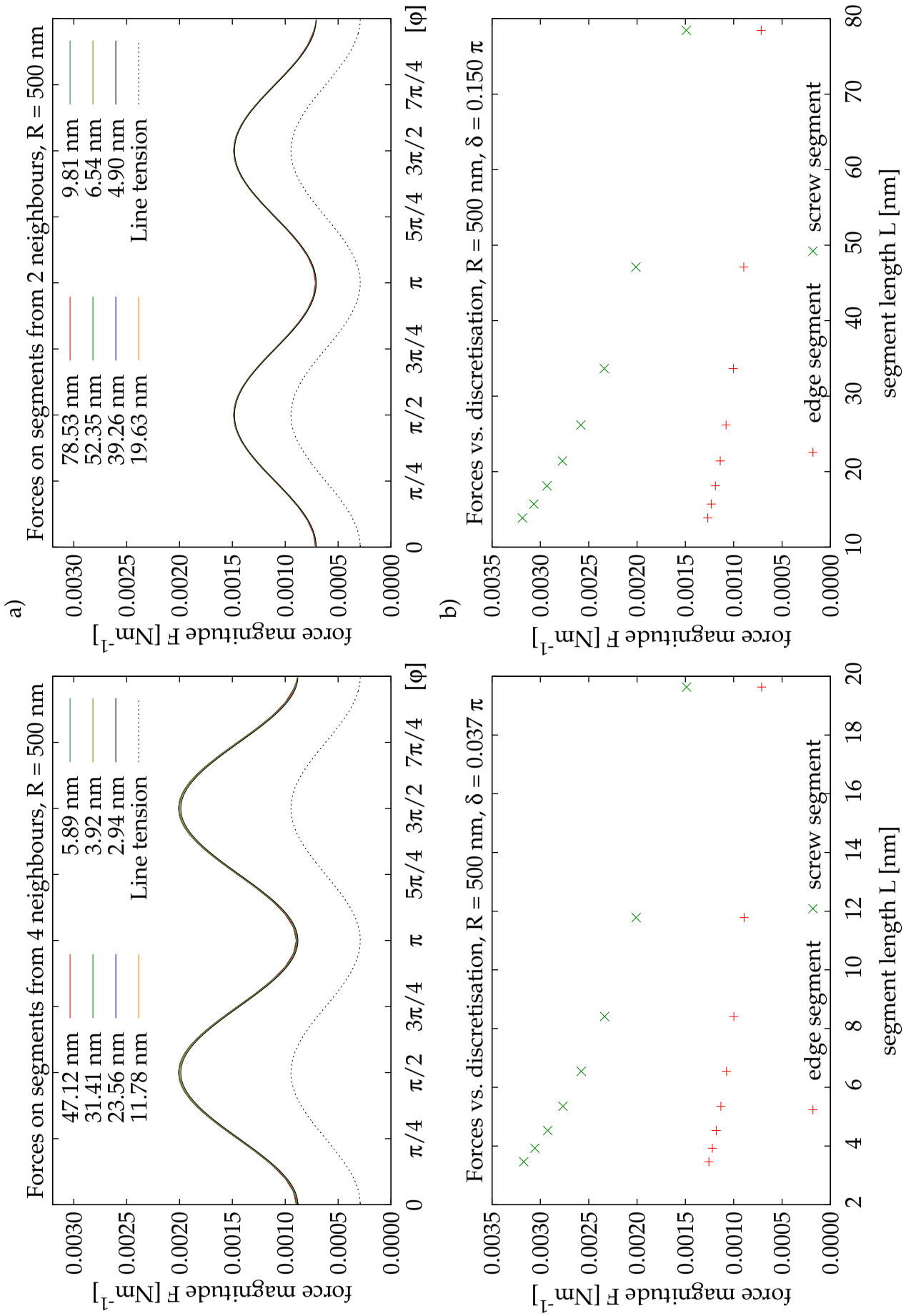

Figure V.11: a) Force magnitude (2/4 neighbours), b) force vs. discretisation (two arc lengths).

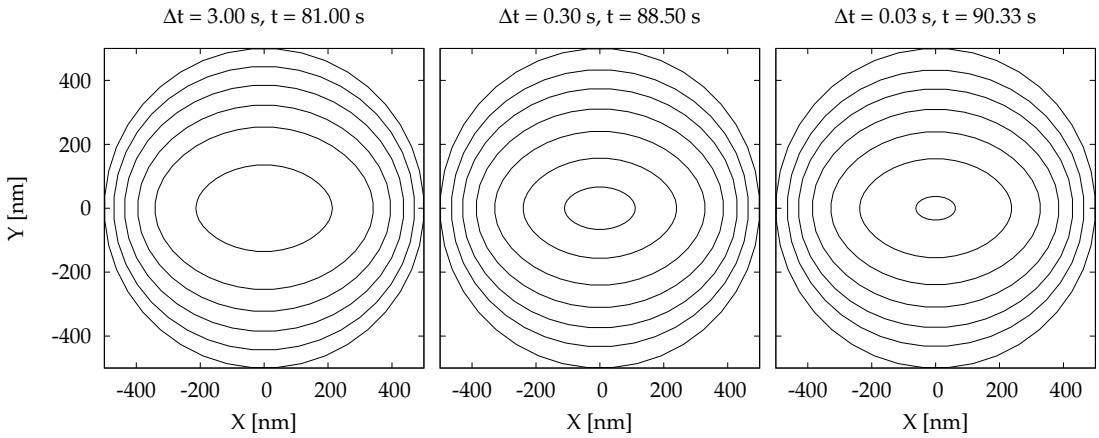

Figure V.12: Loop contraction with a constant time step.

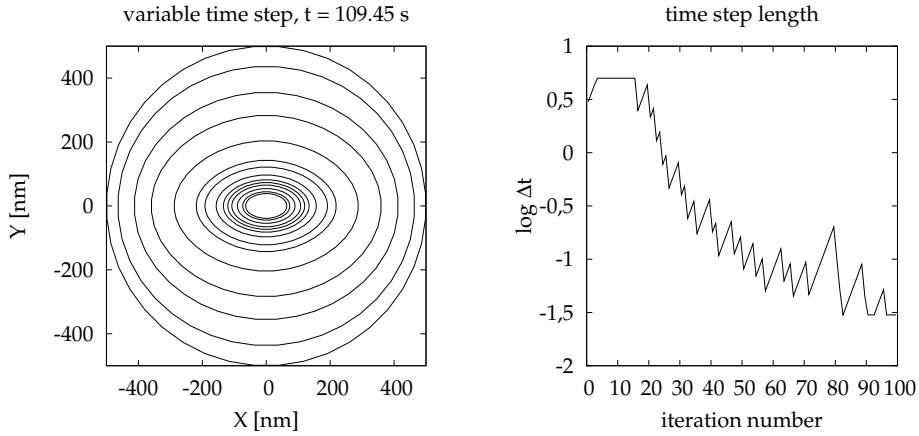

Figure V.13: Loop contraction with a variable time step.

V.5.4 Frank-Read source

The third benchmark simulation dealt with the operation of Frank-Read source and was performed with nodal forces. Initial configuration was a straight dislocation line pinned at points $[0, -100, 0]$ nm and $[0, 100, 0]$ nm equidistantly divided into 25 segments. External stresses of values $\sigma_{xz} \in \{10, 100\}$ MPa were considered. The time integration step was set to $\Delta t = 0.5$ s. The other input parameters are the same as in the Table V.1.

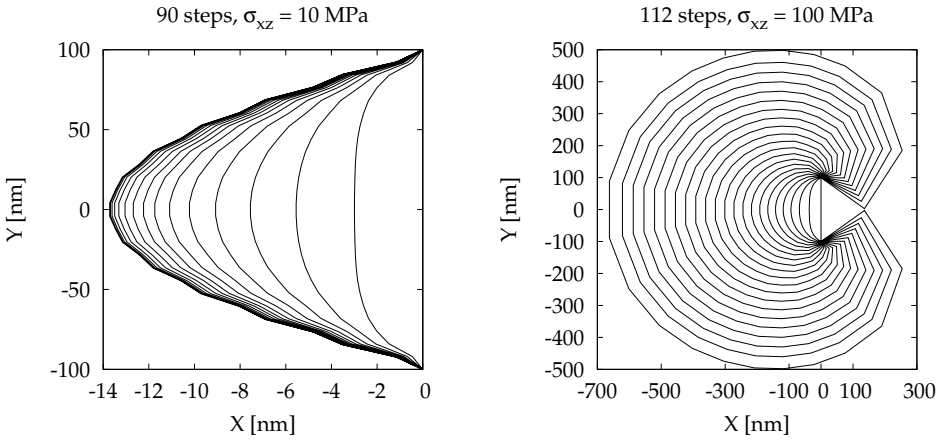

Figure V.14: Frank-Read source.

The results are shown in Fig. V.14. The left picture presents the simulation with the applied stress of 10 MPa, which is lower than the critical stress required for the source operation. Therefore, the source cannot produce new dislocations (note that the left picture is scaled, the original aspect ratio is very narrow – 7:100). The applied stress of 100 MPa is above the critical stress and the source generates dislocation loops by pivoting around the two anchoring points.

VI. Modelling of complex dislocation structures

VI.1 Segment structure and its representation by graphs

VI.1.1 Motivation

Considering the benchmarks described in the section V.5, the system of dislocation segments represented a single dislocation loop, a curved dislocation line pinned at its endpoints (a Frank-Read source) or a single dislocation line connecting two points at a crystal surface. Such simple systems can be represented by an array of nodes, where every node in the array is connected by a segment with its neighbours. The number of segments is the same as the number of nodes for a dislocation loop or minus one for a Frank-Read source. In these special cases, the numerical implementation requires only information about exactly one node and one segment. This approach reduces memory costs of the simulation code.

Even if this representation can be applied also to systems consisting of several dislocation lines, an implementation of topological changes triggered by dislocation reactions would be rather difficult. As a remedy to this problem, a representation based on the graph theory has been applied.

Graph representation

An ideal representation of general dislocation structures is a *graph* $\mathcal{G}$ defined as

$$\mathcal{G} = \{\mathcal{V}, \mathcal{E}\}, \tag{VI.1}$$

where $\mathcal{V} = \{v_i\}$ is a set of vertices and $\mathcal{E} = \{e_i\}$ is a set of edges. An edge $e_i = [a_i, b_i], a_i, b_i \in \mathbb{N}$ is an (ordered) pair of values labelling particular vertices connected by the edge. The order of the values denotes the edge direction from the vertex v_{a_i} to v_{b_i}. Such edge is called *directed* and can be traversed only in the denoted direction. If the pair is unordered, the edge is *undirected*, allowing the traversal in both directions. A graph consisting of directed edges only is called a *directed graph*, whereas the opposite is an *undirected graph*. A *mixed graph* has both directed and undirected edges. If two vertices in the graph are connected by more than one edge, the graph is called a *multigraph*. Further details can be found in [54] or in any textbook about discrete mathematics.

The graph implementation in the presented model builds upon directed graphs. The dislocation structure is considered as a special case of a *multigraph*, where every dislocation segment is represented by two edges in both directions. This approach allows a fast assessment of a particular vertex and its neighbourhood just by listing all edges directed from the vertex.

An example of a dislocation structure represented by a graph is in Fig. VI.1. The initial configuration is a dislocation loop (Fig. VI.1a), which encounters several precipitates during its contraction (Fig. VI.5 shows an actual simulation). The loop encircles the precipitates and the opposite sections of the loop annihilate, leaving dislocation loops

at the precipitates and a remaining loop, which contracts until it annihilates (Fig. VI.1b). The annihilation of the opposite loop sections changes the topology of the system. In the graph structure, this means, that the set of vertices $\mathcal{V}$ does not change, but some of the edges are removed from the set $\mathcal{E}$ and new edges are added to the set.

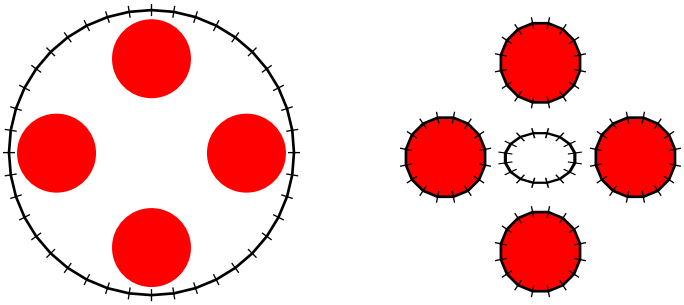

a) Initial configuration.

b) A state after loop contraction.

Figure VI.1: A dislocation loop in the field of particles: a) initial configuration, b) a state before the annihilation of the remaining loop.

The graph approach is advantageous for any situation, where the system topology changes, because the underlying data structures are not dependent on the particular topology of the dislocation system.

VI.2 Segment mobility and force decomposition

VI.2.1 Force decomposition with respect to a glide plane

The Peach-Koehler force is determined by relation (IV.45), i.e.

$$\frac{\boldsymbol{F}}{L} = (\boldsymbol{b} \cdot \hat{\sigma}) \times \boldsymbol{\xi},$$

where $\boldsymbol{b}$ is the Burgers vector and ξ is a unit tangent vector The glide plane normal is determined by a $\boldsymbol{b} \times \boldsymbol{\xi}$ cross product:

$$\boldsymbol{n} = \frac{\boldsymbol{b} \times \boldsymbol{\xi}}{|\boldsymbol{b} \times \boldsymbol{\xi}|}. \tag{VI.2}$$

For a screw dislocation line, the Burgers vector is parallel to the line, which gives a zero normal in the formula (VI.2). This corresponds to a fact that a screw dislocation has no determined glide plane.

The decomposition is based on a projection of the driving force to the glide plane and perpendicular to it (equations (IV.47) and (IV.46)):

$$\boldsymbol{F}_{\mathrm{C}} = (\boldsymbol{F} \cdot \boldsymbol{n})\, \boldsymbol{n}, \quad \boldsymbol{F}_{\mathrm{G}} = \boldsymbol{F} - \boldsymbol{F}_{\mathrm{G}}. \tag{VI.3}$$

These components are used to compute contributions to the dislocation segment velocity:

$$\boldsymbol{v}_{\mathrm{C}} = B\boldsymbol{F}_{\mathrm{C}}, \quad \boldsymbol{v}_{\mathrm{G}} = A\boldsymbol{F}_{\mathrm{C}}. \tag{VI.4}$$

The total velocity is a sum of these components:

$$\boldsymbol{v} = \boldsymbol{v}_{\mathrm{G}} + \boldsymbol{v}_{\mathrm{C}}. \tag{VI.5}$$

The prefactors for the driving force component are described in the section V.2. We recall the relation between the glide prefactor A and the climb prefactor B is $A = 10B$. This decomposition was used for the calculations mentioned above, but these involved only the glide motion of the dislocations.

VI.2.2 Stress tensor decomposition

The drawback of the decomposition mentioned above is that a relation of a pure screw segment with its mixed-character neighbours is completely neglected. The screw segments cannot glide in arbitrary slip planes, as their motion is constrained by their neighbours. To remedy this issue, an attempt was made to compute the climb component of the driving force using the diagonal terms of the stress tensor and the glide component using the off-diagonal terms of the stress tensor.

$$\begin{aligned}
\sigma_{ij}^{\mathrm{H}} &= \begin{cases} \sigma_{ij} \Leftrightarrow i = j, \\ 0 \Leftrightarrow i \neq j, \end{cases} \\
\sigma_{ij}^{\mathrm{S}} &= \begin{cases} 0 \Leftrightarrow i = j, \\ \sigma_{ij} \Leftrightarrow i \neq j, \end{cases} \\
\boldsymbol{F}_{\mathrm{C}} &= (\boldsymbol{b} \cdot \hat{\sigma}^{\mathrm{H}}) \times \boldsymbol{\xi}, \\
\boldsymbol{F}_{\mathrm{G}} &= (\boldsymbol{b} \cdot \hat{\sigma}^{\mathrm{S}}) \times \boldsymbol{\xi}, \\
\boldsymbol{v} &= A\boldsymbol{F}_{\mathrm{G}} + B\boldsymbol{F}_{\mathrm{C}}.
\end{aligned} \tag{VI.6}$$

The advantage of this approach is that the simulation program can easily switch between these two approaches to the force decomposition with no further changes to the code. The velocity components are thus computed using the relations (VI.4) a (VI.5).

VI.2.3 Force decomposition with respect to crystallographic slip planes

The implementations discussed so far do not take into account the fact that a mobility of a dislocation segment is related to the underlying crystallography. The fast glide can occur only in crystallographic planes of the material. Otherwise, only non-compact glide or climb due to diffusion is possible. Both these processes are much slower than the glide in crystallographic planes.

The following method takes the effect of the crystallography into account. It is derived from the former method described in the section VI.2.1. At first, the unit normal vector $\boldsymbol{n}$ of the slip plane of the segment is determined by the relation (VI.2). Then the driving force is decomposed by the relation (VI.3). If the particular slip plane $\boldsymbol{n}$ corresponds to any crystallographic plane from a set N_{K}, i.e.

$$|\arccos \boldsymbol{n} \cdot \boldsymbol{n}_k| \leq 1^{\circ}, \quad \boldsymbol{n}_k \in N_{\mathrm{K}}, \tag{VI.7}$$

following decomposition is used:

$$\boldsymbol{F}_{\mathrm{G}_2} = (\boldsymbol{F}_{\mathrm{G}} \cdot \boldsymbol{n}_k)\, \boldsymbol{n}_k, \quad \boldsymbol{F}_{\mathrm{G}_1} = \boldsymbol{F}_{\mathrm{G}} - \boldsymbol{F}_{\mathrm{G}_2}. \tag{VI.8}$$

The component $\boldsymbol{F}_{\mathrm{G}_1}$ corresponds to the glide in a crystallographic plane with normal vector $\boldsymbol{n}_k$, whereas the component $\boldsymbol{F}_{\mathrm{G}_2}$ is responsible for the non-compact glide. In a particular calculation, this component is nonzero only due to rounding errors. The component $\boldsymbol{F}_{\mathrm{C}}$ is the climb component of the driving force, like in section VI.2.1.

If there is no $\boldsymbol{n}_k$ fulfilling the relation (VI.7), the decomposition changes this way:

$$\boldsymbol{F}_{\mathrm{G}_1} = \boldsymbol{0}, \quad \boldsymbol{F}_{\mathrm{G}_2} = \boldsymbol{F}_{\mathrm{G}}. \tag{VI.9}$$

In this case there is no glide in any of the crystallographic planes, thus $\boldsymbol{F}_{\mathrm{G}_1}$ is zero. The component lying in the slip plane of the particular segment corresponds to the non-compact glide $\boldsymbol{F}_{\mathrm{G}_2}$.

Finally, the segment velocity is computed according to the relations (V.7) and (V.9):

$$\boldsymbol{v}_{\mathrm{G}_1} = A_1 \boldsymbol{F}_{\mathrm{G}_1}, \quad \boldsymbol{v}_{\mathrm{G}_2} = A_2 \boldsymbol{F}_{\mathrm{G}_2}, \quad \boldsymbol{v}_{\mathrm{C}} = B \boldsymbol{F}_{\mathrm{C}}. \tag{VI.10}$$

The prefactors follow the ideas mentioned in sections V.2 and VI.2.1. The prefactor B is the same as in the relation for the climb velocity V.7 and the A_1 and A_2 are scaled glide prefactors. The crystallographic glide is set to $A_1 = 10B$ like in the former paragraphs. The non-compact glide is slow, so we set it to a value of the same order as the climb prefactor, usually $A_2 = B$ or $A_2 = 2B$.

The total velocity of the segment is the sum of the individual velocity contributions:

$$\boldsymbol{v} = \boldsymbol{v}_{\mathrm{G}_1} + \boldsymbol{v}_{\mathrm{G}_2} + \boldsymbol{v}_{\mathrm{C}}. \tag{VI.11}$$

VI.2.4 Force decomposition with respect to crystallographic slip planes and components of the Burgers vector

Here, the driving force is computed separately for two segments composing the overall dislocation segment, which generally may exhibit a mixed character. Thus the Burgers vector of a general mixed segment is first decomposed into its edge $\boldsymbol{b}_e$ and screw $\boldsymbol{b}_s$ parts:

$$\boldsymbol{b} = \boldsymbol{b}_e + \boldsymbol{b}_s, \quad \boldsymbol{b}_s = (\boldsymbol{b} \cdot \boldsymbol{\xi})\xi, \quad \boldsymbol{b}_e = \boldsymbol{\xi} \times \frac{\boldsymbol{b} \times \boldsymbol{\xi}}{|\boldsymbol{b} \times \boldsymbol{\xi}|} = \boldsymbol{b} - \boldsymbol{b}_s \tag{VI.12}$$

Next, the Peach-Koehler forces are computed as

$$\boldsymbol{F}_e = (\boldsymbol{b}_e \cdot \hat{\sigma}) \times \boldsymbol{\xi}, \quad \boldsymbol{F}_s = (\boldsymbol{b}_s \cdot \hat{\sigma}) \times \boldsymbol{\xi}, \tag{VI.13}$$

following the relation (IV.45).

Also this method takes into account the effect of the crystallography on the dislocation mobility. Again, the unit normal vector $\boldsymbol{n}$ of the slip plane of the segment is computed by the relation (VI.2). A crystallography plane $\boldsymbol{n}_k \in N_{\mathrm{K}}$ is found by the criterion (VI.7), if possible.

The edge $\boldsymbol{F}_e$ and screw component $\boldsymbol{F}_s$ of the Peach-Koehler forces are analyzed separately.

We introduce a mobility function $\beta(b)$:

$$\beta(b) = \frac{D_s \Omega}{b^2 kT}, \tag{VI.14}$$

which corresponds to the diffusion processes. (See section V.2 and the relation (V.7).) The b is the length of the Burgers vector or its component.

- The screw component $\boldsymbol{F}_s$.

  The segment lies in a crystallographic plane, but the $\boldsymbol{F}_s$ does not, or vice versa.
  The segment motion is not in a crystallographic plane – a non-compact glide. The condition:

$$[\boldsymbol{\xi} \cdot \boldsymbol{n}_k = 0 \wedge \boldsymbol{F}_s \cdot \boldsymbol{n}_k \neq 0] \vee [\boldsymbol{\xi} \cdot \boldsymbol{n}_k \neq 0 \wedge \boldsymbol{F}_s \cdot \boldsymbol{n}_k = 0]. \tag{VI.15}$$

  We set a prefactor

$$A_s = a_{\mathrm{nc}}\, \beta(|\boldsymbol{b}_s|). \tag{VI.16}$$

  The segment and $\boldsymbol{F}_s$ lie in a crystallography plane. The segment motion is in a crystallographic plane. The condition:

$$\boldsymbol{\xi} \cdot \boldsymbol{n}_k = 0 \wedge \boldsymbol{F}_s \cdot \boldsymbol{n}_k = 0 \tag{VI.17}$$

  We set a prefactor

$$A_s = a_{\mathrm{g}}\, \beta(|\boldsymbol{b}_s|). \tag{VI.18}$$

- The edge component $\boldsymbol{F}_e$ is decomposed into a glide component $\boldsymbol{F}_{e,\mathrm{G}}$ and a climb component $\boldsymbol{F}_{e,\mathrm{G}}$ using the relation (VI.3).

  The slip plane $\boldsymbol{n}$ corresponds to the crystallographic plane $\boldsymbol{n}_k$. The condition is

$$\boldsymbol{n} \equiv \boldsymbol{n}_k. \tag{VI.19}$$

  The prefactors are

$$A_{e,\mathrm{G}} = a_{\mathrm{g}}\, \beta(|\boldsymbol{b}_e|), \quad A_{e,\mathrm{C}} = \beta(|\boldsymbol{b}_e|). \tag{VI.20}$$

  The slip plane does not correspond to any crystallographic plane. The condition:

$$\boldsymbol{n} \neq \boldsymbol{n}_k. \tag{VI.21}$$

  The prefactors are

$$A_{e,\mathrm{G}} = a_{\mathrm{nc}}\, \beta(|\boldsymbol{b}_e|), \quad A_{e,\mathrm{C}} = \beta(|\boldsymbol{b}_e|). \tag{VI.22}$$

The scaling factors are $a_{\mathrm{g}} = 10$ for the glide in a crystallographic plane and $1 \leq a_{\mathrm{nc}} \leq a_{\mathrm{g}}$ for the non-compact glide.

Finally, the total dislocation segment velocity is

$$\boldsymbol{v} = \left(\frac{b_s}{b}\right)^2 A_s \boldsymbol{F}_s + \left(\frac{b_e}{b}\right)^2 \left(A_{e,\mathrm{G}} \boldsymbol{F}_{e,\mathrm{G}} + A_{e,\mathrm{C}} \boldsymbol{F}_{e,\mathrm{C}}\right). \tag{VI.23}$$

VI.3 Interactions between dislocations and precipitates

The mobile dislocation lines can encounter an obstacle – a particle of a *secondary phase* (*precipitate*) in the crystal. If the crystalline structure of the particle does not correspond to the crystal lattice of the surrounding material (a matrix), the boundary between the matrix and the secondary phase impedes the dislocation motion. If the lattice planes of the matrix and the secondary phase are in a complete register, the secondary phase

is *coherent* with the matrix. When the register is not perfect, the boundary between the materials is *semicoherent* and can be described by a dislocation arrangement. This situation happens if the lattice parameters of the two phases are about the same order. In the opposite case, the secondary phase is *incoherent*. In the case of coherent or semicoherent precipitates, the dislocations can under special circumstances pass through the boundary between a matrix and the precipitate. On the other hand, the incoherent precipitates are impenetrable and are considered rigid. The presented model is focused on the latter case.

In the present model, the interactions between a dislocation line and a precipitate are analyzed on the level of individual dislocation segments. Boundary conditions at the particle-matrix interface do not allow dislocation lines to enter the interior of the particle. The numerical implementation thus must care about this constraint and check, whether the straight segments do not cross the particle surface.

In a general case, the endpoints of a single straight segment before and after a displacement are situated in the vertices of a tetrahedron. If we take infinitesimal time steps, the moving segment will sweep along a curved surface. As it would be rather difficult to compute an intersection of the swept curved surface and the particle surface, we approximate the area swept in a single integration step by a rectangle, i.e. the endpoints during the single iteration lie in a single plane. This approximation does not prevent the segments from rotation, as both techniques for determining the coordinates for the next integration step allow the dislocation segments to rotate (see section V.4). In what follows, we focus on spherical precipitates only.

VI.3.1 Intersection of a sphere and a plane

Let's have a plane with the following parametrisation:

$$\mathcal{P} = \{P | \boldsymbol{P} = \boldsymbol{P}'_0 + s\boldsymbol{v}_1 + t\boldsymbol{v}_2, \quad s, t \in \mathbb{R}\}. \tag{VI.24}$$

The plane equation is

$$ax + by + cz = d, \quad \boldsymbol{n} = (a, b, c), \quad \boldsymbol{n} = \frac{\boldsymbol{v}_1 \times \boldsymbol{v}_2}{|\boldsymbol{v}_1 \times \boldsymbol{v}_2|}, \quad |\boldsymbol{n}| = 1, \quad d = \boldsymbol{n} \cdot \boldsymbol{P}'_0, \tag{VI.25}$$

where the vector $\boldsymbol{P}'_0$ denotes the position of the point P'_0. A distance of a point $\boldsymbol{X}$ from the plane $\mathcal{P}$ can be computed by a relation

$$d_X = |\boldsymbol{n} \cdot \boldsymbol{X} - d|. \tag{VI.26}$$

If there is a sphere with radius r in the coordinate origin, we substitute $\boldsymbol{X} = (0, 0, 0)$ into (VI.26). The intersection of the sphere and the plane must correspond to one of the following conditions:

$|d| > r \quad \rightarrow$ a plane and a sphere have no common point
$|d| = r \quad \rightarrow$ a plane and a sphere have a single point of contact $[da, db, dc]$,
$|d| < r \quad \rightarrow$ a circle with a center at $\boldsymbol{K}'_0 = (da, db, dc)$ and a radius $R = \sqrt{r^2 - d^2}$.

Now we consider a sphere not centered at the coordinate origin (i.e. at $[0, 0, 0]$), but in an arbitrary point S. To calculate an intersection with a plane, which contains a point

P_0, we introduce a coordinate system with an origin at S. The position vectors in this coordinate system are denoted by a prime throughout this paragraph. The position of the point P_0 in this coordinate system is determined by a vector $\boldsymbol{P}_0' = \boldsymbol{P}_0 - \boldsymbol{S}$. The vector $\boldsymbol{P}_0'$ is substituted into into (VI.25).

The interesting case is an intersection of the plane and a sphere – an intersection circle $\mathcal{K}$. The circle lies in the plane $\mathcal{P}$ and the points along the circle fulfil the plane parametrisation. If we take two orthonormal vectors $\boldsymbol{f}_1$ and $\boldsymbol{f}_2$, we can parametrise the circle as[1]

$$\mathcal{K} = \{K | \boldsymbol{K} = \boldsymbol{K}_0 + s\boldsymbol{f}_1 + t\boldsymbol{f}_2, \quad s = R\cos\varphi, \quad t = R\sin\varphi, \quad \varphi \in \langle 0, 2\pi \rangle\}. \tag{VI.27}$$

In the plane $\mathcal{P}$ defined by (VI.24) the vectors $\boldsymbol{f}_1$ and $\boldsymbol{f}_2$ are

$$\boldsymbol{f}_1 = \frac{\boldsymbol{v}_1}{|\boldsymbol{v}_1|}, \quad \boldsymbol{f}_2 = \frac{\boldsymbol{n} \times \boldsymbol{v}_1}{|\boldsymbol{n} \times \boldsymbol{v}_1|}. \tag{VI.28}$$

The remaining step is to find the circle center in the unprimed coordinates:

$$\boldsymbol{K}_0 = \boldsymbol{K}_0' + \boldsymbol{S}. \tag{VI.29}$$

Now we have a relation for the circle as an intersection of a plane and a sphere. The plane is determined by a vertex before and after the displacement and its neighbouring vertex (for the nodal forces), or by the dislocation segment and its displacement vector (for the segment forces). Now we will calculate the maximum displacement, which won't make the segment intersect the particle surface. To compute this, we need to find a tangent to the intersection circle parametrised in the preceding paragraph.

A tangent of a circle $\mathcal{K}$ parametrised by (VI.27) at a point parametrised by φ_0 fulfils a parametric equation of a straight line:

$$T_{\varphi_0} = \{T | \boldsymbol{T} = \boldsymbol{T}_0 + u\boldsymbol{v}_{\varphi_0}, \quad u \in \mathbb{R}\} \tag{VI.30}$$

Let the point of contact corresponds to $u = 0$, therefore $T_0 = \mathcal{K}(\varphi_0)$. The tangent direction vector is determined by a derivation of a curve at the given point, so we have

$$\boldsymbol{v}_{\varphi_0} = \left.\frac{\mathrm{d}\mathcal{K}(\varphi)}{\mathrm{d}\varphi}\right|_{\varphi_0} = (-R\sin\varphi_0)\boldsymbol{f}_1 + (R\cos\varphi_0)\boldsymbol{f}_2. \tag{VI.31}$$

Without losing generality, we can replace it with a unit vector:

$$\boldsymbol{n}_{\varphi_0} = (-\sin\varphi_0)\boldsymbol{f}_1 + (\cos\varphi_0)\boldsymbol{f}_2. \tag{VI.32}$$

From the orthonormality of $\boldsymbol{f}_1$ a $\boldsymbol{f}_2$ follows:

$$\begin{array}{rcl} \boldsymbol{f}_1 \cdot \boldsymbol{n}_{\varphi_0} & = & -\sin\varphi_0 \\ \boldsymbol{f}_2 \cdot \boldsymbol{n}_{\varphi_0} & = & \cos\varphi_0 \end{array} \Rightarrow \varphi_0 = -\operatorname{arctg}\frac{\boldsymbol{f}_1 \cdot \boldsymbol{n}_{\varphi_0}}{\boldsymbol{f}_2 \cdot \boldsymbol{n}_{\varphi_0}} + k\pi, \quad k \in \{0, 1\}. \tag{VI.33}$$

The equation (VI.33) has two solutions, as there are two tangents parallel to $\boldsymbol{v}_{\varphi_0}$ at two distinct points of contact.

The angle φ_0 determines the point of contact and the tangent direction vector, which we already know. So we only need to find the points of contact, thence we do not need to know φ_0. As the points of contact are symmetric with respect to the circle center, we obtain the following relation:

$$\boldsymbol{T}_0 = \boldsymbol{K}_0 + (\pm R\cos\varphi_0)\boldsymbol{f}_1 + (\pm R\sin\varphi_0)\boldsymbol{f}_2 = \boldsymbol{K}_0 + (\pm R\boldsymbol{f}_2 \cdot \boldsymbol{n}_{\varphi_0})\boldsymbol{f}_1 + (\mp R\boldsymbol{f}_1 \cdot \boldsymbol{n}_{\varphi_0})\boldsymbol{f}_2. \tag{VI.34}$$

[1] This parametrisation is frequently used in two dimensional space with $\boldsymbol{f}_1 = (1, 0)$ and $\boldsymbol{f}_2 = (0, 1)$.

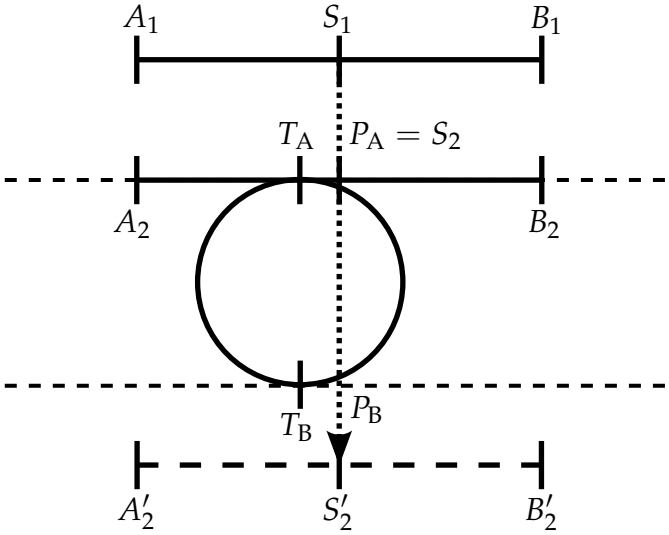

Figure VI.2: A contact between a segment and a particle.

VI.3.2 Contact of the dislocation line with the particle

An example configuration of a dislocation line segment approaching a spherical particle is shown in Fig. VI.2. If there was no particle, the driving force would displace the segment[2] A_1B_1 to the position $A'_2B'_2$. If neither the vertices nor the segment AB is allowed to enter the particle, we consider a plane determined by A_1, B_1, A'_2, or vectors $\boldsymbol{\xi} = (B_1 - A_1)/|(B_1 - A_1)|$ and $\Delta\boldsymbol{R} = S'_2 - S_1$. We assume that, after the reconnection of the segment system (see section V.4), the segment center will displace only slightly from this plane. A necessary condition of the line-particle contact is an existence of an intersection between the plane and the sphere representing the particle.

If there is an intersection – a circle $\mathcal{K}$, we need to find the tangents to $\mathcal{K}$, which are parallel with the segment AB. The choice of geometry guarantees, that each of these tangents has an intersection with a straight line $S_1S'_2$. We denote these intersections by the symbols P_A and P_B in Fig. VI.2. Then we distinguish following cases concerning the tangents parallel to the given dislocation segment AB and the intersections P_A and P_B:

1. *Both intersections lie on the ray S'_2S_1, but do not lie on the segment S'_2S_1.*
   The dislocation line moves away from the particle, no contact will occur.
2. *One intersection lies on the ray S'_2S_1 but not on the segment S'_2S_1, another lies on the ray and the segment $S_1S'_2$.*
   The dislocation line has entered the particle interior. This case is forbidden by the boundary conditions.
3. *Both intersections lie on the ray $S_1S'_2$, at least one of them lies on the segment $S_1S'_2$.*
   The line will get into contact with the particle. One of the intersection points P_A and P_B, which is nearer to S_1, corresponds to S_2, which is the center of the displaced segment stopped at the particle surface.

[2]Here we introduce a short-hand notation for line segments, rays and straight lines, which can be parametrised by two points A and B:

$$\boldsymbol{X} = \boldsymbol{A}(1-t) + \boldsymbol{B}t. \tag{VI.35}$$

For a segment AB, we set $t \in \langle 0, 1\rangle$. For a ray AB, we set $t \in \langle 0, \infty\rangle$, i.e. the ray starts at the point A. For a straight line AB the parameter is $t \in \mathbb{R}$. A similar notation is used also for polygonal chains, e.g. $ABCD$ is a polygonal chain built from segments AB, BC and CD starting at A and ending in D. This notation is used also in section I.2.

4. *Both intersections lie on the ray S_1S_2', but none of them lie on the segment S_1S_2'.*
   The line will not get into contact with the particle in the current integration step.

When a dislocation gets into contact with a particle (Fig. VI.3a), the interaction with the particles cannot be analyzed using the algorithm mentioned above. The driving forces usually do not change too much from one iteration to another. Thus we can suppose, that the driving force acting on a segment stopped at the particle will be directed also inside the particle in the next iteration. This would make any further movement of the dislocation segment impossible. Thus a different approach is necessary to solve this problem.

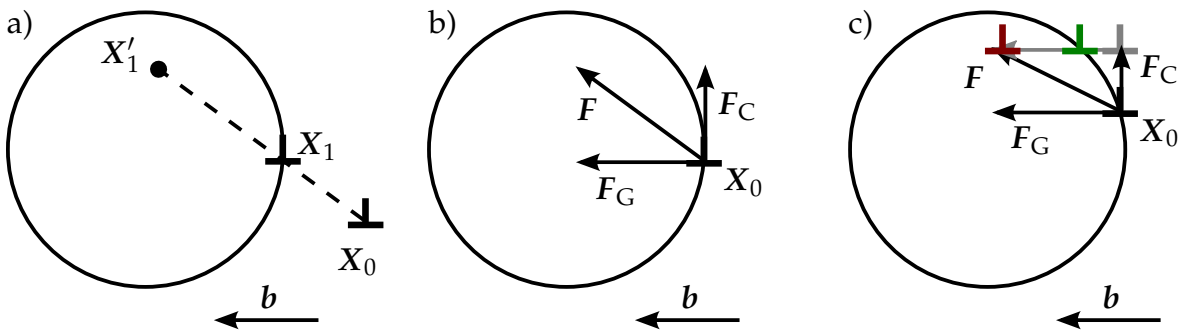

Figure VI.3: A contact with a particle: a) initial contact, b) segment blocked on the particle boundary, force splitting, c) partial displacements: glide, climb and glide.

In such situations, the driving force is decomposed to a glide component $\boldsymbol{F}_G$ and a climb component $\boldsymbol{F}_C$, e.g. according to the relations (IV.46) and (IV.47) (see section IV.4). Note that if the decomposition based on the components of the Burgers vector is used (see section VI.2.4), then the force components $\boldsymbol{F}_e$ and $\boldsymbol{F}_s$ are instead a subject of the analysis.

This decomposition is shown in Fig. VI.3b. As it can be seen from the figure, we suppose that at least one of the components may be directed outside of the precipitate. In such a case, we take the algorithm mentioned above, but it is applied for displacements calculated from the individual components of the driving force. As it is generally undefined, which component should be considered first, the program displaces the segment at first by the glide component, secondly a displacement by climb component follows, and finally the displacement by the glide component is repeated if the initial glide displacement was hindered by the particle. The mechanism of the displacement along the particle surface is illustrated in Fig. VI.3c.

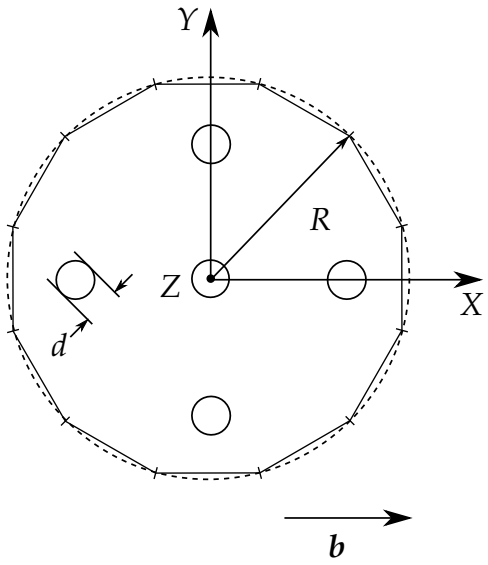

Figure VI.4: A dislocation loop and 4 particles.

VI.4 A single loop with particles – planar simulation

The extended model, now comprising the dislocation-particle interaction, was applied to a self-contraction of a single dislocation loop (like in Fig. V.5), in a field of 4 spherical particles, see Fig. VI.4. The simulation parameters were the same as in the previous case and are summarized in the Table VI.1.Unless otherwise stated, all further mentioned simulations have been performed with the forces acting upon segments.

Table VI.1: Parameters of the simulation.

μ	$0.8 \cdot 10^{11}\ \mathrm{Nm}^{-2}$	shear modulus
ν	0.3	Poisson ratio
D_0	$2 \cdot 10^{-4}\ \mathrm{m}^2\mathrm{s}^{-1}$	diffusion factor for zero Q
Q	$240\ \mathrm{kJ\,mol}^{-1}$	activation energy of self-diffusion
T	873 K	temperature
Ω	$(3.5 \cdot 10^{-10}\ \mathrm{m})^3$	atomic volume
$\boldsymbol{b}$	$(2,0,0) \cdot 10^{-10}\ \mathrm{m}$	Burgers vector
R	500 nm	initial dislocation loop radius
N	40	# of nodes of the approximating polygon
Δt	3 s	initial time step
d	$\{50, 100, 200, 225\}$ nm	diameters of spherical particles
e	$425\ \mathrm{nm} - d/2$	particle eccentricity
$\boldsymbol{c}_i$	$\{[\pm e, 0]; [0, \pm e]\}$	coordinates of particle centers
λ	$\sqrt{2}e$	interparticle distance

VI.4.1 Results

The simulation was performed for 4 different particle diameters. The results are presented in Fig. VI.5. Obviously, the results show many numerical artifacts, which mostly come from the absence of a remeshing procedure. A detailed discussion of this issue is presented later in section VI.7. The long segments cannot properly encircle the spherical precipitates and that leads to the unsatisfactory results for small particle diameters ($d \in \{50, 100\}$ nm). On the other hand, these results show, that the self-stress driven loop contraction takes place even in the particle field. However, the distance $\lambda - d$ must be large enough, so that the parts of the dislocation loop can bow-out and pass by the particles. In case of bigger particles, i.e. $d \in \{200, 225\}$ nm, the interparticle gate $\lambda - d$ is rather short and the system remains in an equilibrium state, whereas the smaller particles with larger gates $\lambda - d$ allow the system to undergo an annihilation process[3] leaving four loops on the matrix-particle interfaces.

VI.5 Two dislocation loops with particles – 3D motion

The results of the planar loop simulations provided a motivation to investigate the influence of the time integration step also for the 3D simulations. To facilitate a comparison with the former calculations, very similar simulation parameters have been

[3] It will be described later in section VI.8.

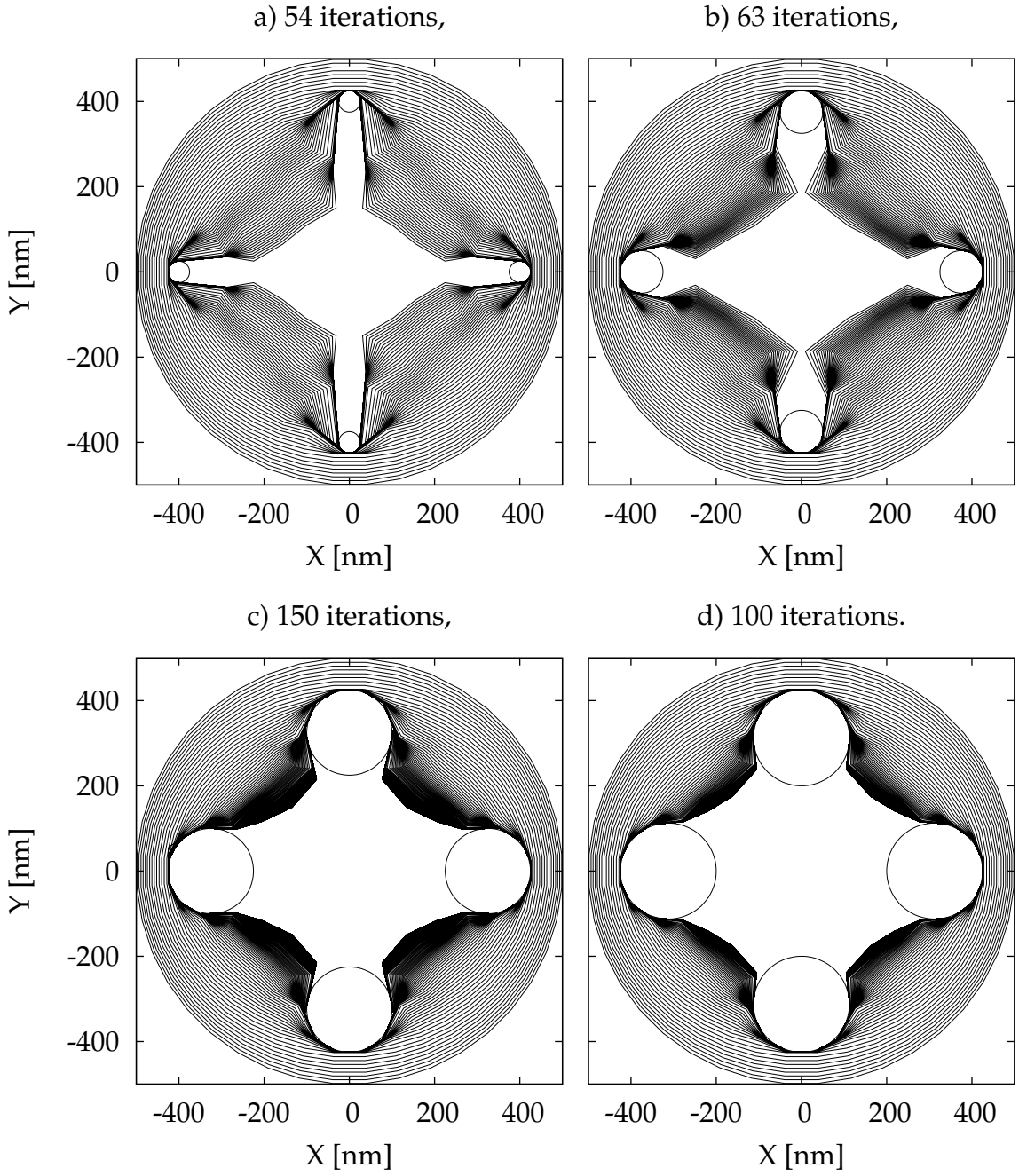

Figure VI.5: A contraction of a single dislocation loop in a field of spherical particles for $N = 40$ segments and a particle diameter d: a) 50, b) 100, c) 200 and d) 225 nm.

Table VI.2: Parameters of the 3D simulation. See also Table VI.1.

R	1500 nm	initial dislocation loop radius
N	$\{40; 80; 120; 160\}$	# of nodes of the approximating polygon
Δt	$\{6.00; 0.60; 0.06; 0.01\}$ s	initial time step
d	600 nm	spherical particle diameters
e	1150 nm	particle eccentricity
h	100 nm	initial loop distance

used (see V.5 and VI.4), with the stress-tensor decomposition based relations for the dislocation segment mobility (see VI.2.2). The number of the particles and their location were the same. Several fixed time integration steps and discretisations were used: $\Delta t \in \{6.00; 0.60; 0.06; 0.01\}$s and $N \in \{40; 80; 120; 160\}$. Neither any remeshing technique nor a time step adjustment was used in these simulations. The simulation parameters are summarized in Table VI.2, the remaining parameters are the same as in Table VI.1.

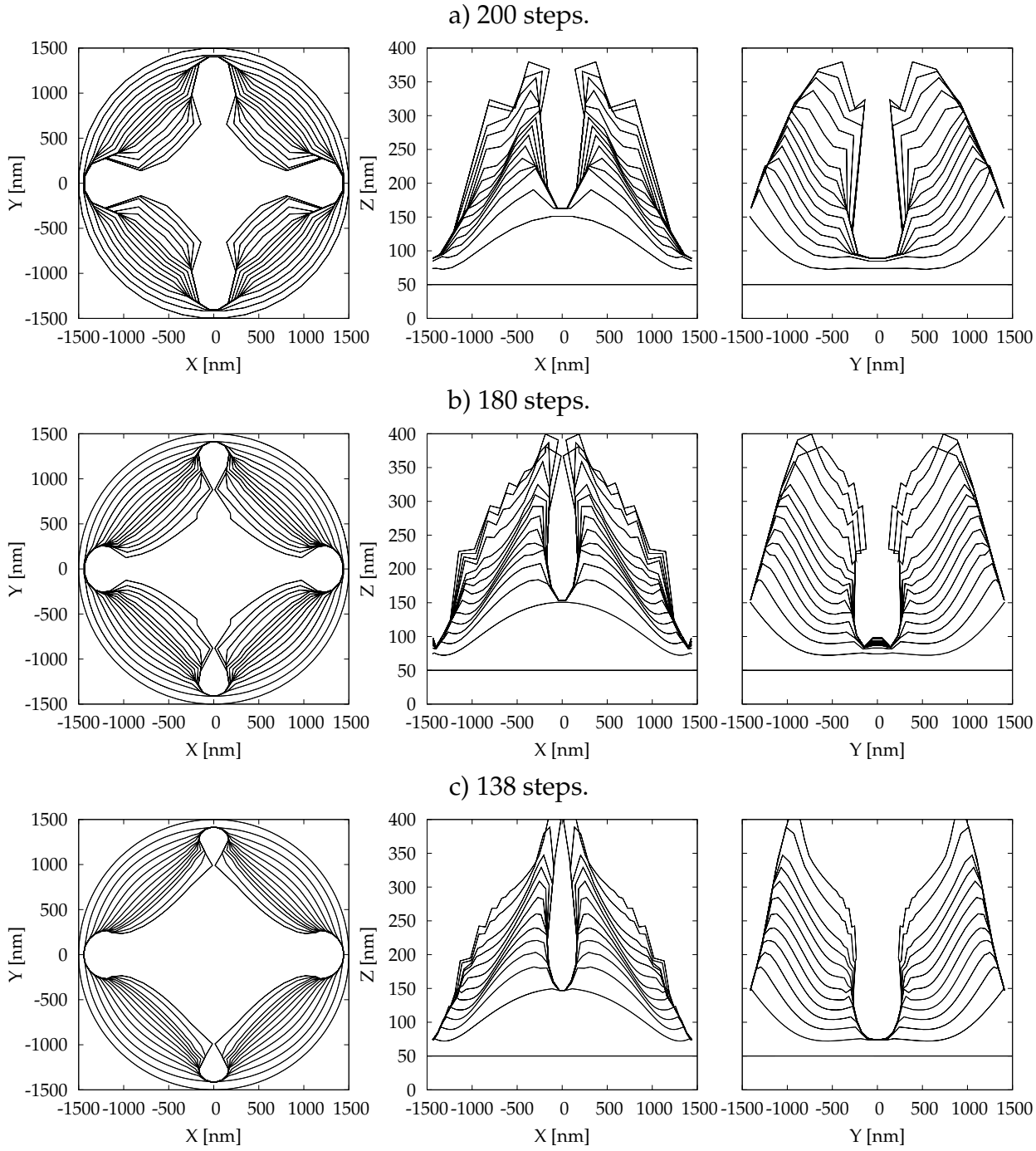

Figure VI.6: 2D projections of an upper dislocation loop during its evolution with $\Delta t = 6$ s and different mesh density: a) $N = 40$, b) $N = 80$ and c) $N = 120$ segments.

The results of the simulations with a time step $\Delta t = 6$ s are shown in Fig. VI.6. The Fig. VI.6a ($N = 40$) clearly illustrates artifacts connected with the very coarse discretisation of the loop. The next Fig. VI.6b shows that even a finer discretisation with $N = 80$ is not sufficient. Only the discretisation with $N = 120$ offered plausible smooth curves during the major part of the simulation. However, the time step $\Delta t = 6$ s is too coarse.

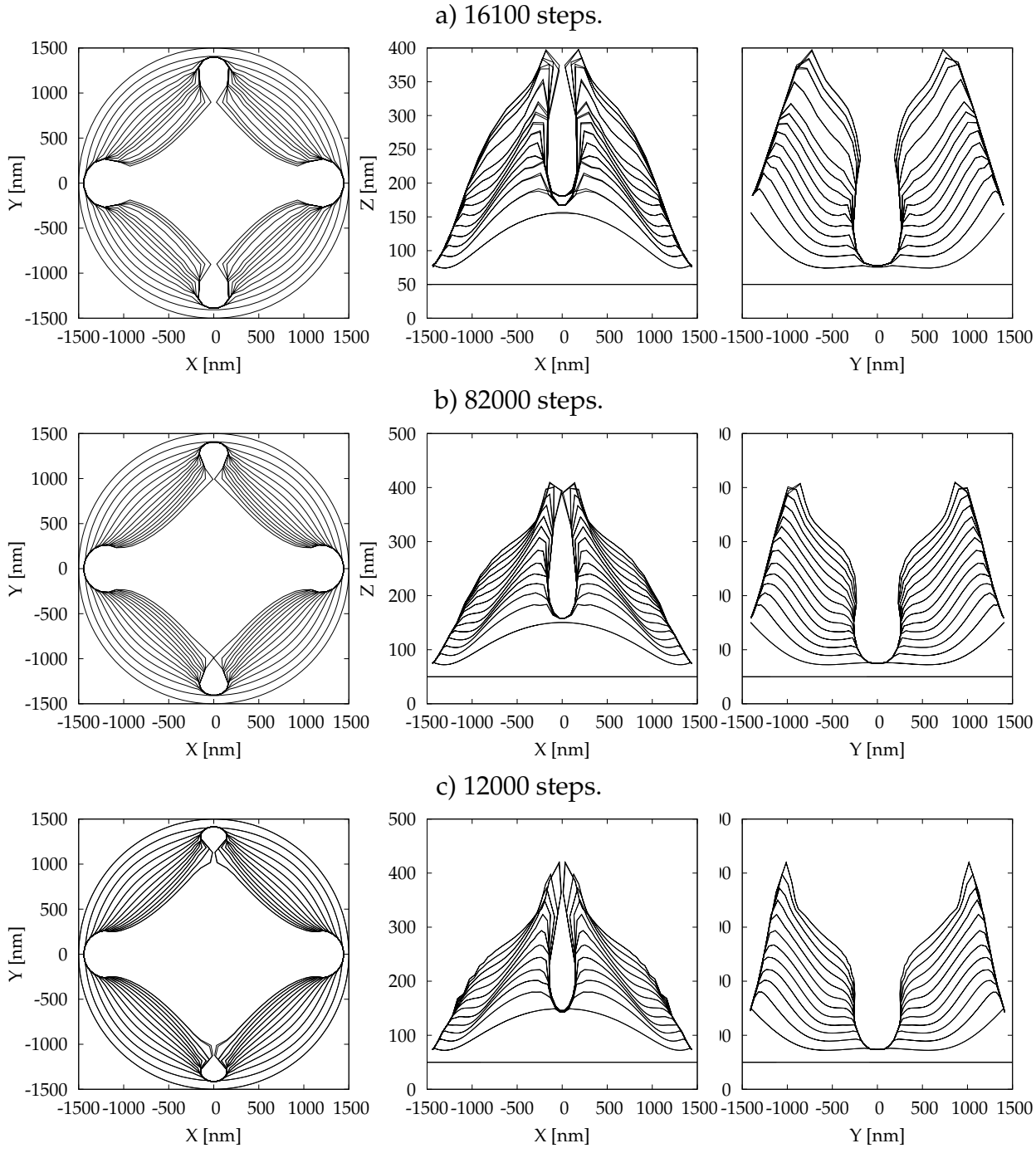

Figure VI.7: 2D projections of an upper dislocation loop during its evolution with a) $\Delta t = 0.06$ s and $N = 120$, b) $\Delta t = 0.01$ s and $N = 120$, c) $\Delta t = 0.06$ s and $N = 160$.

Results for finer time steps with discretisation $N = 120$ are presented in Fig. VI.7a and b. The results show that the sharp spikes almost disappeared when the time step

was shortened by two orders of magnitude to $\Delta t = 0.06$ s. Also a simulation with $\Delta t = 0.01$ s was run for comparison. However, the six times shorter time step was not so advantageous while keeping the same discretisation. A single calculation with even finer discretisation $N = 160$ is illustrated in Fig. VI.7c. The results show smooth dislocation curves. The evolution is stopped just before the annihilation of dislocation line segments encircling the particles, as the annihilation technique had not yet been developed at the time of these simulations.

VI.6 Symmetry (I.)

As the time integration step decreases, the number of iterations inevitably rises and the overall accuracy of the simulation decreases due to a cumulation of rounding errors. The analysis of the results shows that the shapes of the dislocation loops in later iterations do not correspond to the physical symmetry of the system. The planar simulations with a single loop were not much influenced by the rounding errors. Consequently, the loss of symmetry with respect to the planes $X = 0$ and $Y = 0$ is hardly visible even with large magnifications. On the other hand, the 3D simulations are more sensitive and the artifacts coming from rounding errors are visible even without magnification.

The loss of symmetry is associated with the rounding errors during the summation of the stress fields or driving forces. It is obvious that with a rising number of computation steps these errors grow and negatively influence the results. It is very likely that these problems would cause instabilities during more complex simulations.

A symmetry break-up caused by the rounding errors was eliminated when a unit cell technique was employed. This technique allows to reproduce the whole system by the elementary cell and symmetry operations. For the case of the planar simulations, the elementary cell is the 1st quadrant, for the 3D simulations, the elementary cell is the 1st octant of the system. The initial implementation only transformed the segment coordinates from the elementary cell to the rest of the system. This approach proved to be working and reliably preventing the simulations from failure due to this kind of computational errors. The results were slightly different from the previous simulations without the symmetry transformations. A drawback of this approach is a less-efficient algorithm – the symmetry of the simulated system was not used to reduce the memory consumption and time complexity (the time complexity even slightly increased due to the transformation of the coordinates from the elementary cell – a quadrant or an octant).

VI.6.1 Advanced representation of symmetric systems

An analysis of the interactions between individual segments showed that the corresponding forces reflect the physical symmetry of the system. Thus the whole system can be represented by an elementary cell, which can be mirrored to the whole system by the symmetry operations. Accordingly, the calculation of forces acting upon any dislocation segment can be based only on the dislocation segments from the elementary cell. As a result, it is necessary to retain only the elementary system in the computer memory, which considerably decreases the memory costs of simulation. Besides that, all operations need to be performed only for the segments in the elementary cell, which thus reduces also the computation time.

Now we recall the calculation of the total stress field at the center of a j^{th} segment at a position $\boldsymbol{R}_j$:

$$\hat{\sigma}_j = \sum_{i=1, i\neq j}^{n} \hat{T}_i \tilde{\sigma}(\hat{T}_i^{-1}\boldsymbol{R}_{j,i}, L_i)\hat{T}_i^{-1}, \quad \boldsymbol{R}_{i,j} = \boldsymbol{R}_i - \boldsymbol{R}_j. \tag{VI.36}$$

Here $\hat{T}_i$ is a transformation from a local coordinate system (x, y, z) to the global coordinates (X, Y, Z) and $\tilde{\sigma}$ is the stress tensor around a straight segment of dislocation oriented along a z axis (local), which is determined by a Peach-Koehler formula (IV.37).

The stress field $\hat{\sigma}_j$ at the center $\boldsymbol{R}_j$ causes a Peach-Koehler force upon the j^{th} segment determined by the relation

$$\boldsymbol{F}_j = (\boldsymbol{b} \cdot \hat{\sigma}_j) \times \boldsymbol{\xi}_j. \tag{VI.37}$$

Because the cross product as well as the matrix multiplication are linear functions of their arguments, we can change the summation by the index i and rearrange the Peach-Koehler force upon the j^{th} segment as a sum of *forces* from individual dislocation segments:

$$\boldsymbol{F}_j = \sum_{i=1, i\neq j}^{n} \boldsymbol{F}_{j,i}(\boldsymbol{R}_{j,i}, L_i), \tag{VI.38}$$

where the individual contributions are computed as

$$\boldsymbol{F}_{j,i}(\boldsymbol{R}_{j,i}, L_i) = \left[\boldsymbol{b} \cdot \left(\hat{T}_i \tilde{\sigma}(\hat{T}_i^{-1}\boldsymbol{b}_i, \hat{T}_i^{-1}\boldsymbol{R}_{j,i}, L_i)\hat{T}_i^{-1}\right)\right] \times \boldsymbol{\xi}_j. \tag{VI.39}$$

This rearrangement of the summation will be used to compute Peach-Koehler forces in the symmetric system.

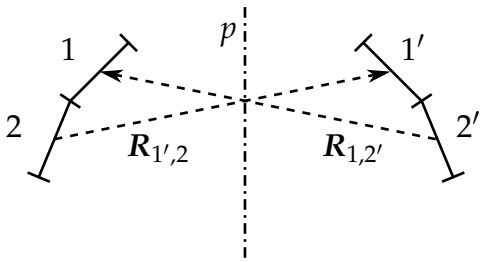

Figure VI.8: Calculation of the Peach-Koehler forces in a symmetric system.

We will demonstrate this idea on a system consisting of four dislocation segments with a planar symmetry (see Fig. VI.8). Two couples of segments 1, 1′ and 2, 2′ are symmetric with respect to the plane p. A force, which the segment 2 exerts upon a segment 1′, i.e. $\boldsymbol{F}_{1',2}(\boldsymbol{R}_{1',2}, L_{2'})$ is a mirror image of the force, which the segment 2′ exerts upon the segment 1, i.e. $\boldsymbol{F}_{1,2'}(\boldsymbol{R}_{1,2'}, L_2)$. The plane of symmetry is p. A general force contribution exerted by a primed segment upon an unprimed segment is computed according to following relation

$$\boldsymbol{F}_{j,i'}(\boldsymbol{R}_{j,i'}, L_i) = \operatorname{sgn}(\hat{Z}')\, \hat{Z}_{\mathrm{L}}^{\prime -1} \left\{ \left[\boldsymbol{b} \cdot \left(\hat{T}_i \tilde{\sigma}(\hat{T}_i^{-1}\boldsymbol{R}_{j',i}, L_i)\hat{T}_i^{-1}\right)\right] \times \left(\hat{Z}'_{\mathrm{L}}\boldsymbol{\xi}_j\right)\right\}, \; \boldsymbol{R}_{j',i} = \hat{Z}'\boldsymbol{R}_j - \boldsymbol{R}_i. \tag{VI.40}$$

The symbol $\hat{Z}'$ denotes an affine transformation, which transforms an unprimed segment or vector upon a primed segment or vector. It's linear component is denoted by

$\hat{Z}'_{\mathrm{L}}$. Note that some transformations, such as the reflection, invert the sense of the dislocation line, which inverts the sense of the resulting force contribution. This is corrected by the term $\mathrm{sgn}(\hat{Z}')$, which is negative in such cases. This general relation is also used for a translational symmetry, see section VI.9.

If we have, for example, a single dislocation loop with the parameters mentioned in Table VI.4, we will have a planar problem with a four-fold symmetry. This kind of symmetry can be expressed also as a reflectional symmetry with two planes (axes). We choose the first quadrant ($X, Y \geq 0$) and the symmetry operations will be reflections with planes $X = 0$ and $Y = 0$. The total number of segments in the system is $N = 40$, so there will be $n = N/4 = 10$ segments in the elementary cell. The segments reflected by the plane $X = 0$ will be denoted by a prime, segments reflected by the plane $Y = 0$ will be denoted by two primes and the segments reflected by both planes will be denoted by three primes (these also have an axial symmetry (Z axis) with the elementary cell).

To compute a total force acting upon, for example, the segment 1, which is $\boldsymbol{F}_1$, we sum all force contributions from the segments in the elementary cell at first, i.e. $\boldsymbol{F}_{1,j}(\boldsymbol{R}_{1,j}, L_j), j \in \{2 \dots n\}$. Further we add the contributions from the primed segments, i.e. $\boldsymbol{F}_{1,j'}(\boldsymbol{R}_{1,j'}, L_{j'}), j' \in \{1' \dots n'\}$, which are computed using a transformation of the force $\boldsymbol{F}_{1',j}(\boldsymbol{R}_{1',j}, L_j), j \in \{1 \dots n\}$ and an appropriate symmetry operation. The same approach is used also for the two-primed and three-primed segments.

VI.6.2 2D simulations with symmetry

The real situation is slightly simplified in the preceding paragraph. The parameters in the section VI.4 (Table VI.1) are set in a such way, that there are two edge segments parallel to the Y axis, whose centers lie in the plane $Y = 0$, and two screw segments parallel to the X axis with centers lying in the plane $X = 0$. To perform the calculation with the symmetry techniques mentioned in the former paragraph, each of these segments has to be divided into two subsegments. Thus in the first quadrant there will be one half of an edge segment and one half of a screw segment. The system will not have 40 segments, but $N = 44$ segments and there will be $n = 11$ segments in the first quadrant.

The parameters were set according to the section V.1, only the time step was set shorter, i.e. $\Delta t = 0{,}03$ s. The results are shown in Fig. VI.9. The resulting shape of the dislocation loop in the last step 2945 ($t = 88{,}35$ s) is very close to the shape of the dislocation loops in the last steps of the former simulations displayed in Fig. V.12 and V.13. The difference between the current simulation and the former ones is that the current loop shrinks slightly faster. However, this is not surprising – as it is mentioned in the section V.5.2, shorter segments (here the four divided segments parallel to the axes $X = 0$ and $Y = 0$) cause higher driving forces, which leads to higher velocities of the segments and faster evolution of the system. It is also possible to run the original simulation with the segments parallel to the axes $X = 0$ and $Y = 0$ artificially divided – this will also make the shrinking process faster and will almost exactly correspond to the simulation run with the symmetry operations. Here the only difference will be a slightly faster motion of the centers of the divided segments, as this is not treated in the numerical implementation.

The symmetrisation is thus an efficient way how to suppress the influence of rounding errors and the corresponding break-up of the system symmetry.

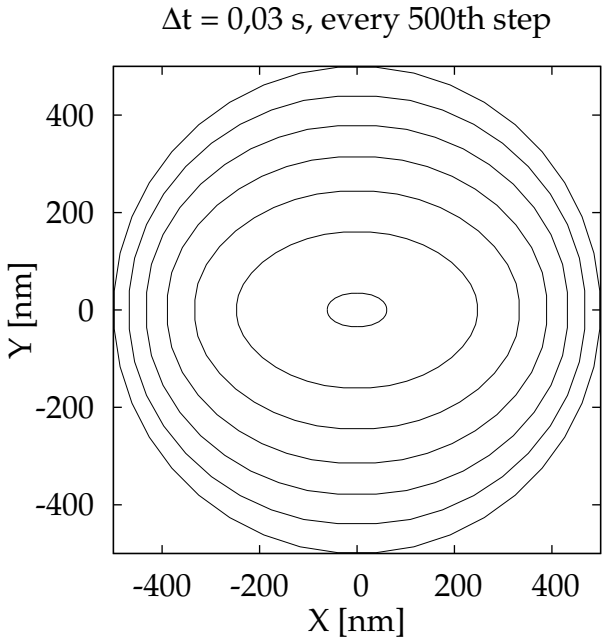

Figure VI.9: An evolution of a single dislocation loop with a four-fold symmetry.

VI.7 Remeshing

An important part of the model is a remeshing of the dislocation lines. As the dislocation line is approximated by a set of short straight segments, this discrete representation should not differ too much from the smooth dislocation curves, which are observed in experiments. This can be achieved only by an adaptive remeshing of the dislocation structure, i.e. by adding, removing and redistributing vertices in the system of straight segments.

If we recall the first results related to a single dislocation loop (section V.5) and the results of the simulation with a couple of co-axial dislocation loops (section VI.5), we see that some of the segments in both simulations became very short. In the latter simulation, the polygonal chain representing the dislocation lines has formed regions with very high curvature (i. e. very small acute angles at some vertices). While the very short segments are physically plausible, these may produce instabilities, or may require too short time integration steps and this considerably slows down the calculation. On the other hand, the nonphysical acute angles at the vertices are a result of a too coarse discretisation, which does not match the smooth dislocation curves. In both cases, it is necessary to adjust the vertex distribution to make the simulation more stable and accurate.

VI.7.1 Adding and removing of a single vertex

The simplest technique is to add (Fig. VI.10) or remove (Fig. VI.11) just a single vertex. During the simulation, the segment length is periodically checked. If the length is out of predefined range, the program adds or removes a vertex. It is very easy to add a vertex by dividing a segment into two segments of an equal length. However, evaluating the Peach-Koehler formula (IV.34) for a case of a pair of dislocation segments lying on a

straight line gives a zero contribution to the stress field from one segment to the other. As a result, both segments would perceive almost equal Peach-Koehler forces, so they would keep their direction for many iterations, making the remeshing less effective, unless these divided segments come into a contact with a precipitate. Obviously, the remeshing should consider the local curvature of the dislocation line. This problem will be discussed further in section VI.7.4.

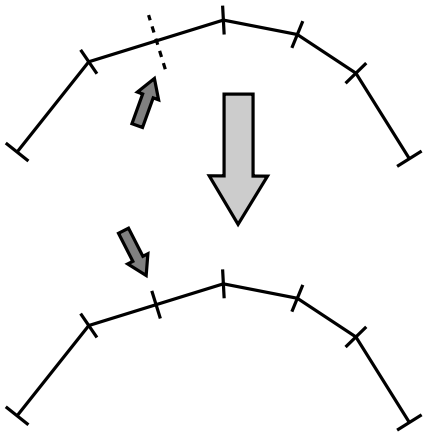

Figure VI.10: Addition of a single vertex.

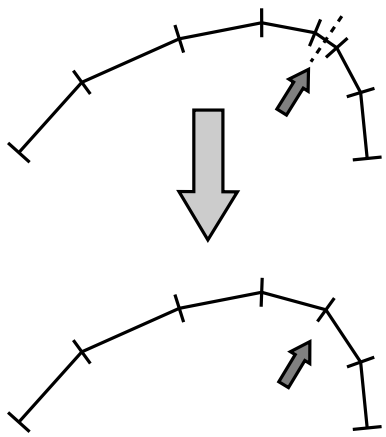

Figure VI.11: Removal of a single vertex.

The program removes a vertex at the endpoint of a segment and connects the neighbouring vertices with a new segment (Fig. VI.11). To improve the results, the other endpoint is moved to the center of the original segment.

VI.7.2 Cubic spline interpolation

Real cubic splines

More sophisticated remeshing procedures can employ cubic splines [55]. Let $f : \langle t_0, t_n \rangle \to \mathbb{R}$ is a real function we need to interpolate. A cubic spline is a piece-wise polynomial function $S(t) : \langle t_0, t_n \rangle \to \mathbb{R}$. The interval $\langle t_0, t_n \rangle$ consists of n subintervals $\langle t_{i-1}, t_i \rangle$, $t_0 < t_1 < \ldots < t_n$, on which cubic polynomials are defined:

$$S(t) = S_i(t) = a_i t^3 + b_i t^2 + c_i t + d_i \Leftrightarrow t \in \langle t_{i-1}, t_i \rangle, \quad i \in \{1, \ldots, n\}. \tag{VI.41}$$

The cubic spline parameters $\{a_i, b_i, c_i, d_i\}, \quad i \in \{1, \ldots, n\}$ are determined by following conditions:

$$\begin{array}{lrcll} a) & S(t_i) & = & f(t_i), & i \in \{0, \ldots, n\}, \\ b) & S_{i+1}(t_i) & = & S_i(t_i), & i \in \{1, \ldots, n-1\}, \\ c) & S'_{i+1}(t_i) & = & S'_i(t_i), & i \in \{1, \ldots, n-1\}, \\ d) & S''_{i+1}(t_i) & = & S''_i(t_i), & i \in \{1, \ldots, n-1\}. \end{array} \tag{VI.42}$$

These conditions give $4n - 2$ equations. As we have $4n$ parameters, two additional conditions are necessary. The following two give a natural cubic spline:

$$\begin{array}{ll} a) & S''(t_0) = 0, \\ b) & S''(t_n) = 0. \end{array} \tag{VI.43}$$

The resulting system of linear equations is represented by a tridiagonal matrix, which can be quickly solved by a Crout method with a time complexity $O(n)$ [55]. This kind

of cubic spline is suitable to aperiodic functions. Periodic functions are not represented properly, as it produces artifacts at the end of the period. For a periodic function $f(t_0) = f(t_n)$, it is necessary to employ another pair of conditions:

$$\begin{array}{ll} a) & S'(t_0) = S'(t_n), \\ b) & S''(t_0) = S''(t_n). \end{array} \tag{VI.44}$$

Again, the system of linear equations can be solved with a time complexity $O(n)$.

Cubic splines in three dimensions

Cubic splines introduced in section VI.7.2 can be used to interpolate curves in a 3D space. Let $\boldsymbol{F} : D_{\boldsymbol{F}} \to \mathbb{R}^3$ is a parametric function. The vector function $\boldsymbol{F}$ determines coordinates of the vertices of the polygonal chain. The function domain $D_{\boldsymbol{F}} = \{t_0, \ldots, t_n\}$ can be a finite ascending series of natural numbers (this is very suitable for the numerical implementation of the Crout method), but a cumulative sum of dislocation segment lengths along the polygonal chain gives a better interpolation of more complex shapes.

The vector function $\boldsymbol{F}$ is interpolated with a vector spline:

$$\boldsymbol{S}(t) : \langle t_0, t_n \rangle \to \mathbb{R}^3. \tag{VI.45}$$

This spline is a parametric function with the following components:

$$\boldsymbol{S}(t) = [S_X(t), S_Y(t), S_Z(t)], \tag{VI.46}$$

where the components $S_X(t)$, $S_Y(t)$ and $S_Z(t)$ are cubic splines defined by the equation (VI.41) and determined by the conditions (VI.42) and supplemental conditions (VI.43) for the polygonal chain or (VI.44) for a closed polygon.

Remeshing

The actual remeshing with the spline changes coordinates of most of the vertices. The ratio of the total length of the original polygonal chain and a predefined optimal segment length gives a count of new segments m. The cubic spline is evaluated at $m + 1$ equidistant points, which become new vertices for the next iteration. (In case of a closed polygon only m points are evaluated.)

VI.7.3 Simulations with remeshing

The simulation with a single dislocation loop (Fig. V.5) was carried out. The parameters are listed in Table VI.3. The time step was variable between 1 s and 5 s and the dislocation segment length was limited to a range $(50, 100)$ nm. Two remeshing techniques have been used: the single-vertex approach for the first simulation and the cubic splines for the second.

The results of the simulation with the single-vertex remeshing are shown in Fig. VI.12. The simulation starts with a circular loop (the outermost circle) and proceeds via shrinking stages in which size of the loop decreases due to its self-stress. As the segments become shorter, some vertices are removed from the system. As can be seen from the figure, during the final iterations the representation becomes very crude (as

Table VI.3: Parameters of the simulation.

μ	$0.8 \cdot 10^{11}\ \mathrm{Nm}^{-2}$	shear modulus
ν	0.3	Poisson ratio
D_0	$2 \cdot 10^{-4}\ \mathrm{m}^2\mathrm{s}^{-1}$	diffusion factor for zero Q
Q	$240\ \mathrm{kJ\,mol}^{-1}$	activation energy of self-diffusion
T	873 K	temperature of simulate process
Ω	$(3.5 \cdot 10^{-10}\ \mathrm{m})^3$	atomic volume
$\boldsymbol{b}$	$(2,0,0) \cdot 10^{-10}\ \mathrm{m}$	Burgers vector
R	500 nm	initial dislocation loop radius
N	42	# of nodes of the approximating polygon
Δt	3 s	initial time step
Δt	$\langle 1,5 \rangle$ s	time step range
$t_\uparrow = t_\downarrow$	2	time step multiplicators
l	$(50,100)$ nm	segment length range
l	75 nm	optimal segment length

the minimum allowed length of a dislocation segments has been set to 50 nm). Also the initial system symmetry is completely lost. This is not caused only by the rounding errors, it is actually broken by the very first vertex removal.

The next simulation used the cubic spline interpolation for remeshing. The simulation shows similar evolution of the dislocation line, as can be seen in Fig. VI.13. The cubic spline representation produces finer discretisation of the dislocation loop for much more iterations than the single-vertex remeshing. Even the symmetry is retained for more iterations. In the last iterations, it is even lost and regained again, because the spline can be well represented even with just a few points. On the other hand, the symmetry is not perfect, as it is influenced by the rounding errors, and also by the redis-

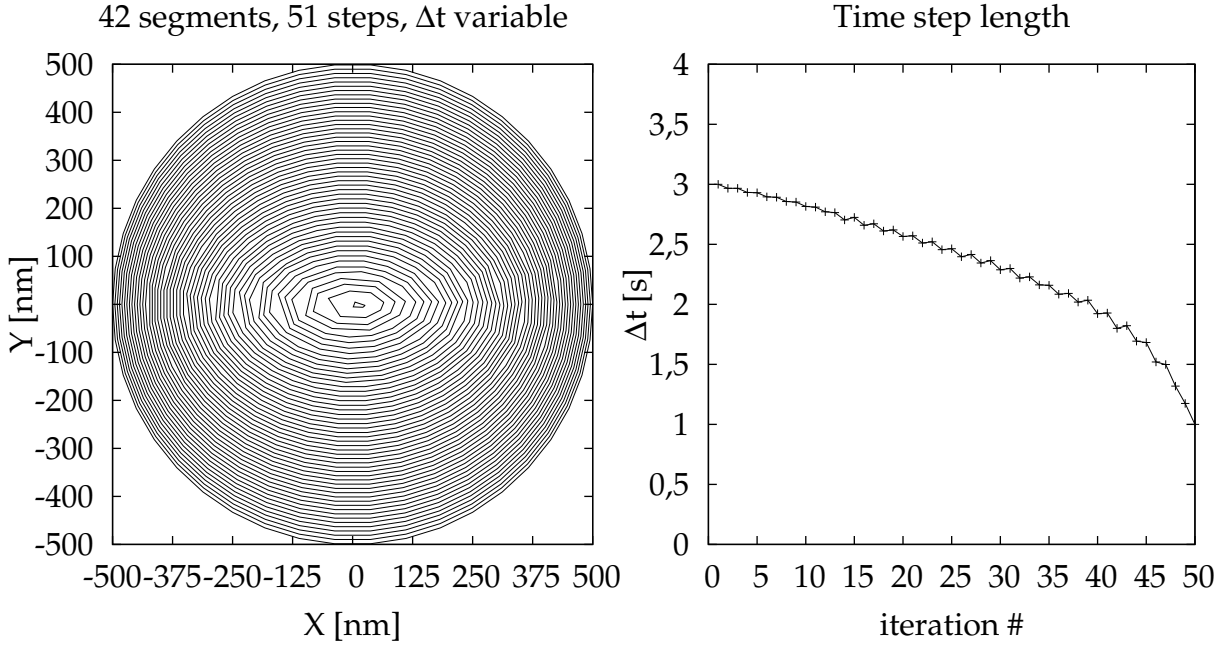

Figure VI.12: A simulation with single vertex addition and removal.

tribution of vertices along the spline, which does not take the symmetry into account.

VI.7.4 Adding and removing of a single vertex – improved method

The single-vertex approach mentioned in section VI.7.1 can be further improved. As in the already mentioned approach, the new point should be added between two end points once the segment length exceeds certain limit (see Fig. VI.14). If the particular segment X_1X_2 is not in contact with any particle (i.e. it can move freely), a circle $\mathcal{C}$ is fitted to the end points X_1, X_2 and their nearest neighbours X_0, X_3. In total, 4 neighbouring vertices are involved. The least-squares method is used to fit a circle to these 4 points. The new vertex is placed at the intersection of the circle $\mathcal{C}$ and the straight line CS_{12}, where S_{12} is the center of the segment X_1X_2 and C is the center of the circle $\mathcal{C}$.

It may happen that the segment X_1X_2 is the ending segment of a polygonal chain, e.g. there would be no vertex X_3. Then it is possible to fit the circle to the points X_0, X_1, X_2 just by solving a set of 3 linear equations.

For a general 3D case, the same approach may be used, but it is necessary to fit a plane to the particular points (3 points define the plane exactly, 4 points require the least-squares method) and fit the circle in the particular plane. The vertex removal is solved by the already mentioned merging of the endpoints of a too short dislocation line segment.

This remeshing method works the same way for both closed polygons (dislocation loops) and polygonal chains (dislocation lines). It is also independent of the symmetry techniques described in section VI.6. It will be used in all simulations presented in the next sections unless stated otherwise.

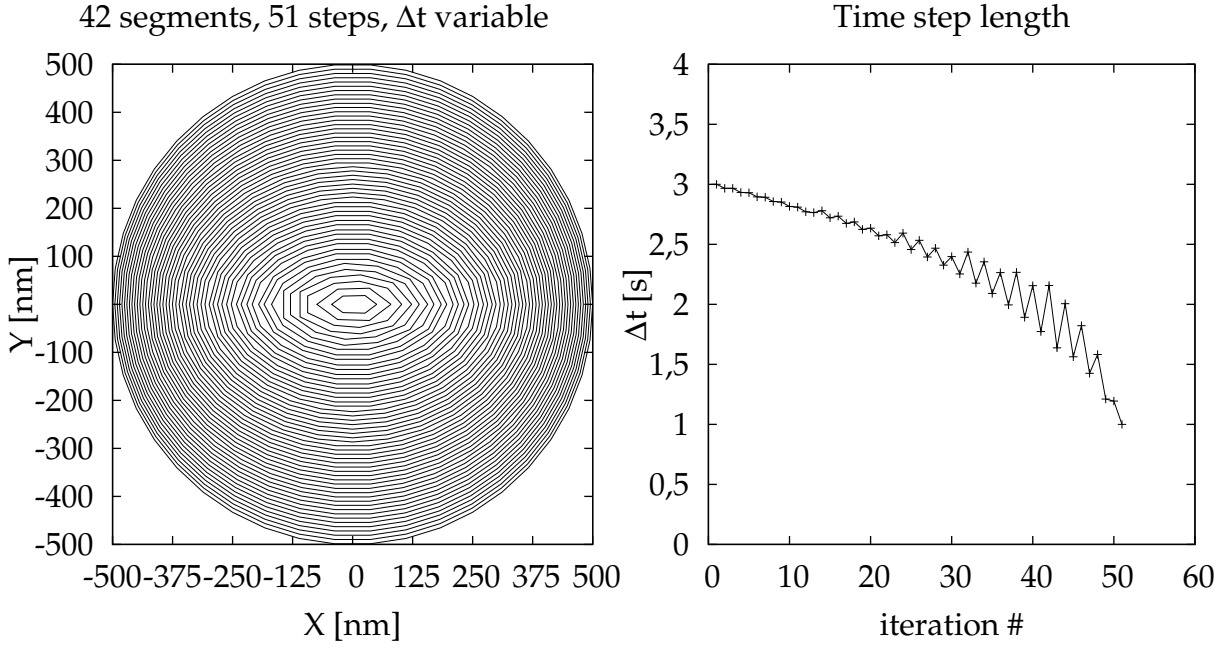

Figure VI.13: A simulation with remeshing based on the cubic spline interpolation.

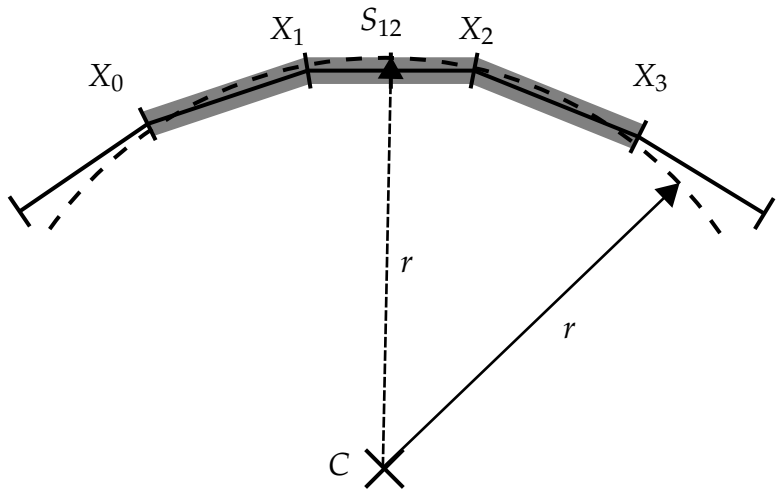

Figure VI.14: Fitting a circle to 4 points.

VI.8 Annihilation

VI.8.1 A general approach

Two dislocations will annihilate, if they have the same orientation and their Burgers vectors have the same magnitude and an opposite direction, or the dislocations have the same Burgers vector and the opposite orientation. These two situations are equivalent. An encounter and an annihilation of two edge dislocations is shown in Fig. VI.15 in a 2D projection. An analogous situation may happen for the screw or mixed dislocations, e.g. for two dislocation curves or for two segments of one dislocation curve.

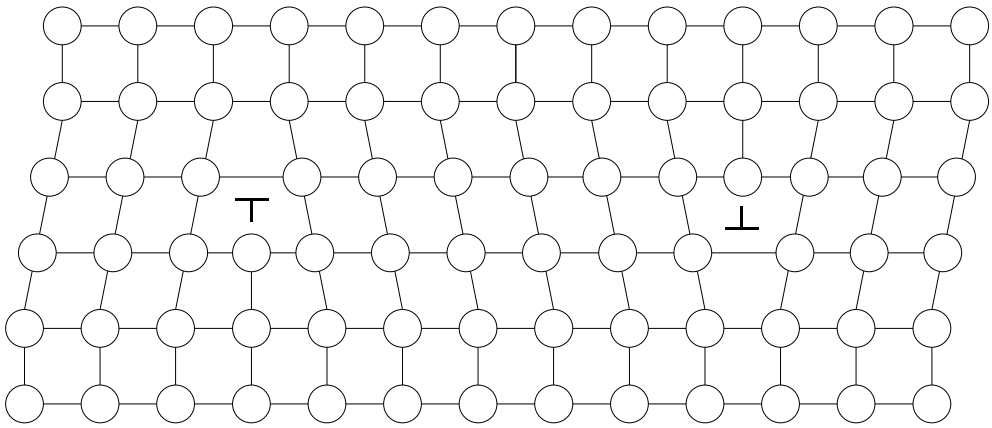

Figure VI.15: Annihilation of two edge dislocations.

An illustrative example of such situation is a Frank-Read source. Upon activation, the source before creating the first loop will take a shape similar to Fig. VI.16a. Further evolution makes parts A and B of the dislocation curve to approach each other up to a critical distance (Fig. VI.16b). The dashed lines are tangents in the nearest two points

of the two parts of the curve. The situation at these points is similar to the situation depicted in Fig. VI.15. The parts of the dislocation curve at this location are going to annihilate. A dislocation loop is created, which expands away from the source due to the externally applied stress. The remaining part of the dislocation is quickly recovered to the initial state by its self-stress as well as the externally applied stress. If the applied stress is high enough, the whole process can repeat and the Frank-Read source can thus produce more dislocation loops.

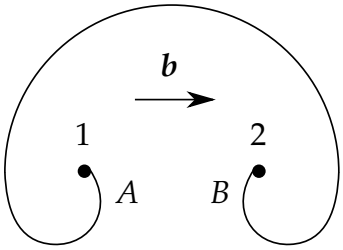

a) The activated source.

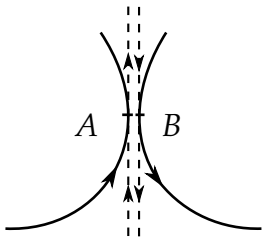

b) Two parts of the dislocation curve approaching each other.

Figure VI.16: A Frank-Read source.

An algorithm for the annihilation

An annihilation of dislocations represented by discrete polygonal lines consisting of straight segments needs a different description, as the tangents in the two nearest vertices do not correspond to the tangents of the continuous lines. Thus the single criterion is the critical distance, at which the dislocations annihilate. The algorithm is illustrated in Fig. VI.17.

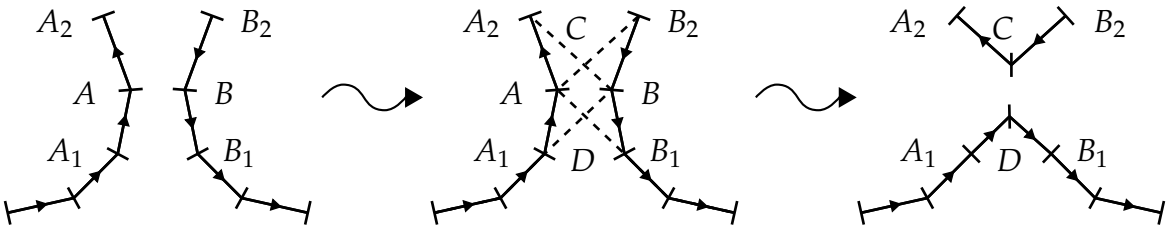

Figure VI.17: An annihilation of dislocation curves represented by a polygonal chain.

If two vertices A and B are in a distance shorter than a critical distance of the annihilation, and these vertices are not neighbours to each other, the topology of the dislocation system is adjusted in a following way. If each of the vertices A and B has exactly two neighbours A_1, A_2 and B_1, B_2, we create two polygonal chains A_1BA_2 and B_1AB_2. In such case it is possible to find two points, where the line segments AB_2 and BA_2 are nearest to each other. Let these points are C_1 and C_2. Similarly, let D_1 and D_2 are points where the line segments BA_1 and AB_1 are nearest to each other. Then C is the centre of a line segment C_1C_2 and D is the centre of D_1D_2. Then we remove sections of the polygonal chains A_1AA_2 and B_1BB_2. These sections are replaced by A_2CB_2 and A_1DB_1. These sections are created in a way fitting the direction of the remaining polygonal chains.

Notes on the numerical implementation

Before the carrying out the annihilation, it is necessary to order the segments according to the Fig. VI.17, so that $|A_1B_1| < |A_1B_2|$ and $|A_2B_2| < |A_2B_1|$. If these relations are not fulfilled, we exchange B_1 and B_2. Then the segments $(A, A_1), (A, A_2), (B, B1)$ and $(B, B2)$ are removed. In the next step, the coordinates of C and D are found, which are assigned to the vertices A and B (an optimization to re-use the vertex structures). Then we create new segments $(A_1, D), (D, B1), (B2, C), (C, A_2)$.

VI.8.2 Planar simulations

The annihilation algorithm described above was tested during the contraction of a single dislocation loop in a field of four precipitates. The simulation parameters including the particle positions and diameters were set according to section VI.4 (Tab. VI.1), but the particle diameter was set to $d = 100$ nm and the time integration step was selected as $\Delta t = 30$ ms. A simple remeshing approach based only the length of segments was used. The critical annihilation distance was set to $d_\mathrm{a} = 10$ nm. The input parameters of the calculation are summarized in Tab. VI.4.

Table VI.4: Simulation parameters for a single dislocation loop contracting and annihilating in a field of particles.

μ	$0.8 \cdot 10^{11}$ Nm^{-2}	shear modulus
ν	0.3	Poisson ratio
D_0	$2 \cdot 10^{-4}$ m^{2}s^{-1}	diffusion coefficient for zero Q
Q	240 kJ mol^{-1}	activation energy of self-diffusion
T	873 K	temperature
Ω	$(3.5 \cdot 10^{-10}$ m$)^3$	atomic volume
$\boldsymbol{b}$	$(2, 0, 0) \cdot 10^{-10}$ m	Burgers vector
R	500 nm	initial dislocation loop radius
N	40	# of segments of the polygon
Δt	0.03 s	time step
l	$\langle 30, 120 \rangle$ nm	segment length
d_a	10 nm	critical distance for annihilation
d	100 nm	particle diameters
e	425 nm $- d/2$	eccentricity of the particles
$\boldsymbol{c}_i$	$\{[\pm e, 0]; [0, \pm e]\}$	position of the particle centers
λ	$\sqrt{2}e$	particle distance

A dislocation loop in a particle field

The simulation is recorded in Fig. VI.18 starting with the outermost loop. The evolution corresponds to systems depicted in Fig. VI.5 for a diameter $d = 100$ nm. The major difference is the time step, which is of two orders smaller than in the former simulations ($\Delta t = 3$ s), which allows to find a configuration of the dislocation loop just before the annihilation of the branches encircling the particles. After the annihilation, new loops

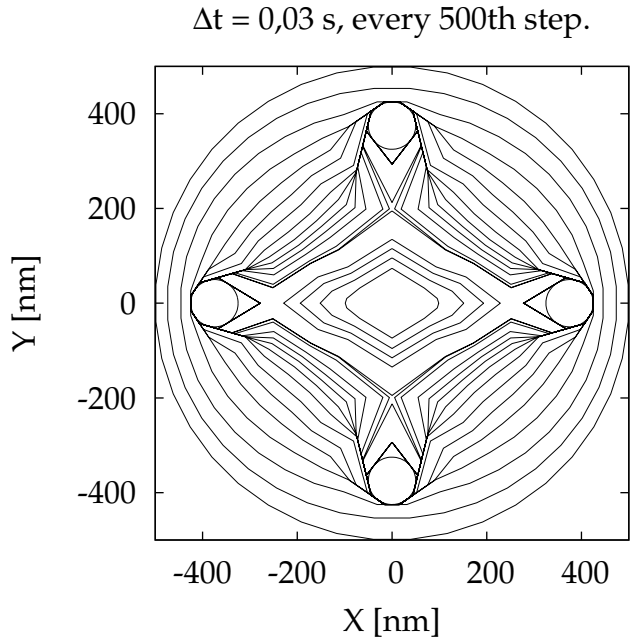

Figure VI.18: A contracting dislocation loop and its interaction with spherical particles.

are detached from the original loop at the particles centered on the Y axis. As the contraction of the remaining loop continues, the loops around the particles centered at X are detached later. Finally, the remaining loop in the center of the system would annihilate, but the system becomes unstable due to the very short dislocation segments. The total number of iterations was 6773, which corresponds to a simulation time $t = 203.19$ s.

Frank-Read source

The simulation with a Frank-Read source (section V.5.4) has been performed second time. The common simulation parameters are listed in Tab. VI.4. The geometry is the same as in the section V.5.4, i.e. a straight dislocation line pinned at points $[0, -100, 0]$ nm and $[0, 100, 0]$ nm and equidistantly divided into 25 segments. An external stress $\sigma_{xz} = 10$ MPa was applied in the first simulation, which converged to an equilibrium state, see Fig. VI.19. In the next simulation an external stress $\sigma_{xz} = 100$ MPa allowed the Frank-Read source to generate dislocation loops, see Fig. VI.20.

Two co-axial loops in a particle field

The annihilation was also tested for a 3D system of two dislocation loops with four spherical particles. The parameters were set according to the section VI.5. Again, the forces acting upon segments were used. The number of segments was $N = 120$ and the time step was $\Delta t = 60$ ms. Initially, the dislocation structure evolves as in the former simulations (see Fig. VI.7), but the simulation continues further with the annihilation process. Again, the very short segments make the simulation unstable, thus only 18000 steps were achieved. This corresponds to total simulation time $t = 1080$ s. Thus only the loops about the particles situated at the Y axis detached from the initial dislocation loops. The evolution is shown in Fig. VI.21.

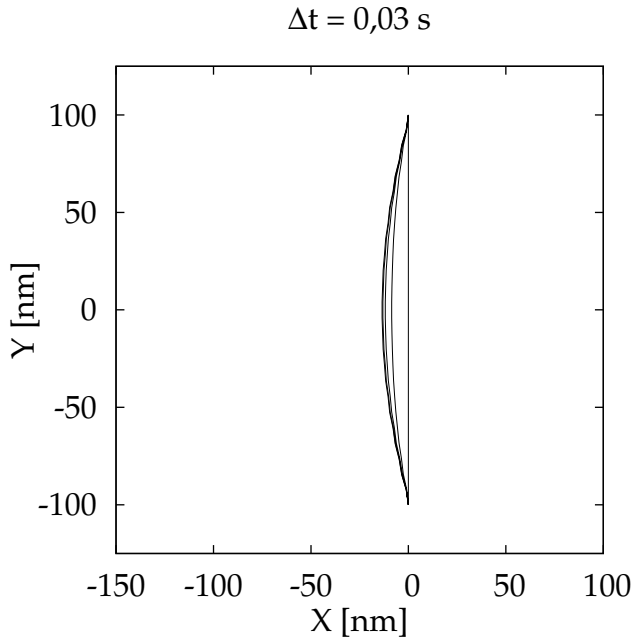

Figure VI.19: A Frank-Read source under shear stress $\sigma_{xz} = 10$MPa – equilibrium state.

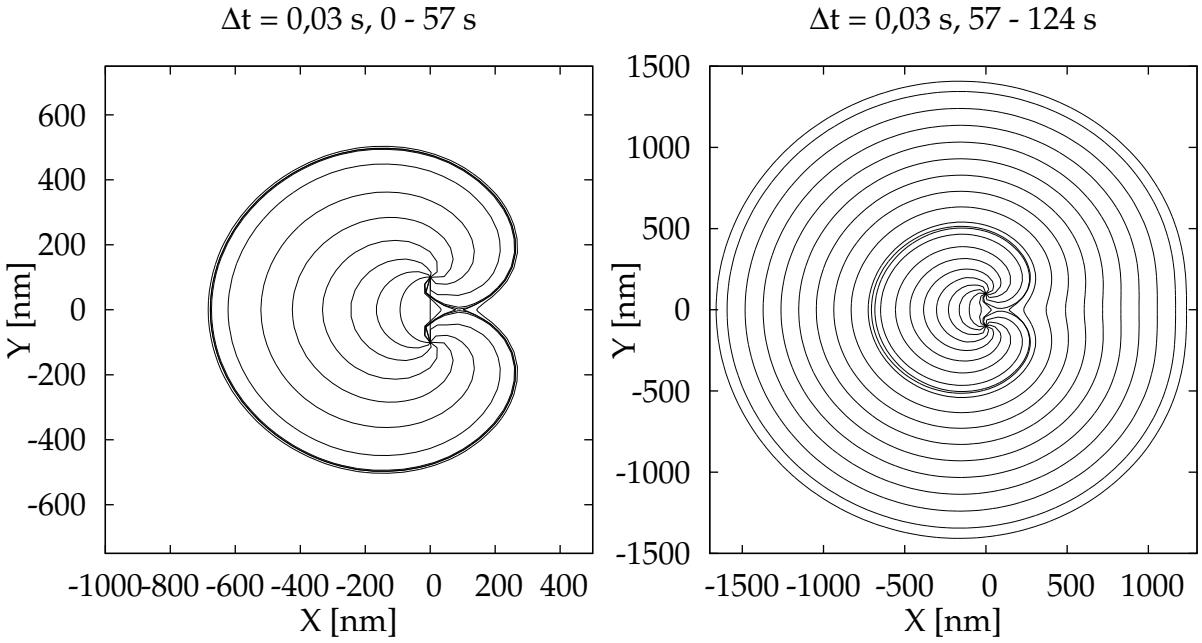

Figure VI.20: A Frank-Read source under shear stress $\sigma_{xz} = 100$MPa generating dislocation loops.

VI.8.3 Annihilation in symmetric systems

The algorithm described in section VI.8.1 has been extended in order to incorporate the symmetry operations in the simulations with particles. The situation before annihilation in a symmetric system is illustrated in Fig. VI.22. The extension of the algorithm is also searching for generalised intersections of two adjacent polygonal chains, in which the

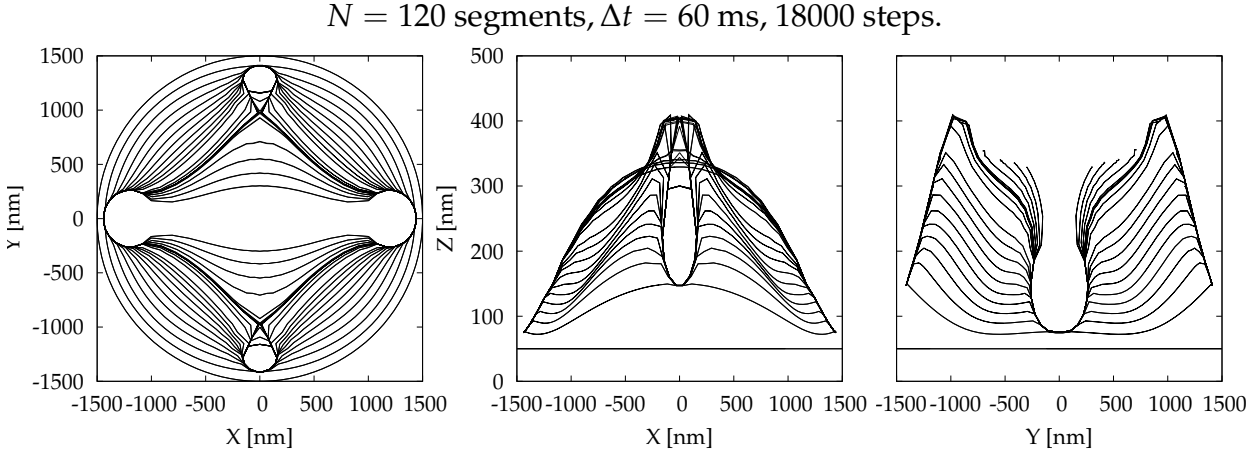

Figure VI.21: An evolution of two co-axial dislocation loops in a 3D crystal with four spherical particles illustrating the annihilation process in 3D. Only the shapes of the upper loop are shown.

two nearest vertices are interchanged. The scheme in Fig. VI.17 shows that the new vertices will be created at the plane of symmetry. The situation can be redrawn, as it is displayed in Fig. VI.23.

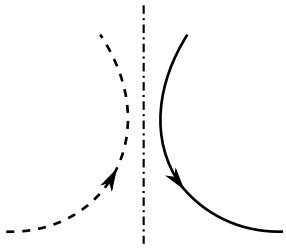

Figure VI.22: Annihilation of a dislocation line (full line) and its image (dashed line).

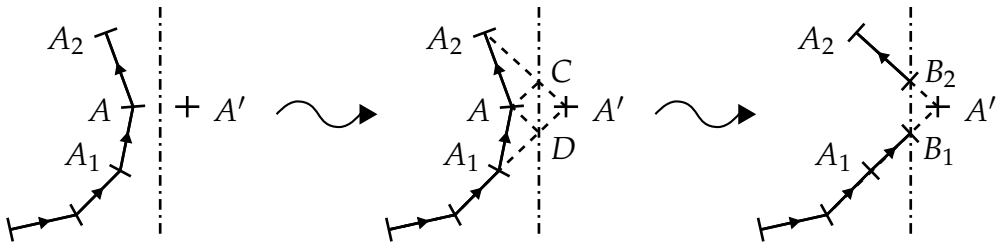

Figure VI.23: Annihilation of a dislocation curve represented by a polygonal line and its symmetric image.

If the distance between a vertex A and its image A' is shorter than the critical distance of annihilation, we find intersections of the line segments A_1A' and A_2A' with the symmetry plane. These are B_1 and B_2 respectively. Further the segments (A_1, A) and (A_2, A) are removed, then also the vertex A is removed and new vertices B_1 and B_2 are created. Then new edges will be created: (A_1, B_1) and (A_2, B_2).

The implementation can be optimized again in a way, that one of the new coordinates (B_1, for example) can be assigned to the original vertex A, so only one segment needs to

be removed (here (A_2, A)) and just one vertex needs to be created with the coordinate B_2 and just one segment needs to be created: (A_2, B_2).

VI.8.4 A planar simulation with particles and a four-fold symmetry

A contraction in a field of particles

The planar simulation with four spherical particles has been repeated according to the section VI.8.2. Thus the number of segments in the whole system was $N = 40 + 4$ and $n = 11$ in the elementary cell (first quadrant). The simulation was performed with forces acting upon the segments.

The results are presented in Fig. VI.24. At the beginning, the shapes are the same as the shapes formed during the simulation with the whole system (Fig. VI.18). Later the simulations show the effect of the fixed direction of the ending segments near the border of the quadrant, which makes the interior loop to keep the diamond shape. The segments propagating through the quadrant border are removed from the system. This is the actual implementation of the annihilation of the contracting loop. The interior loop annihilates (or shrinks completely) in the step 6989 ($t = 206.94$ s). The simulation finished in the next step at the time $t = 206.97$ s as the loops on the particle surfaces cannot contract any more.

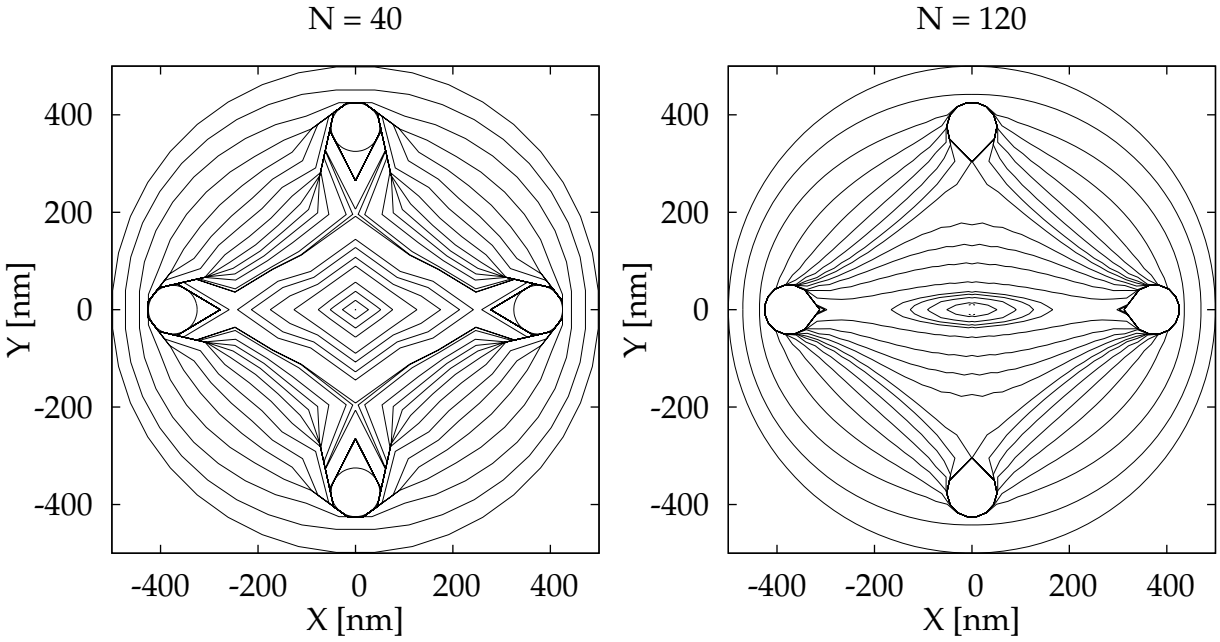

Figure VI.24: An evolution of a single dislocation loop after an interaction with spherical precipitates.

Then the same simulation was carried out second time, but with a finer initial discretisation, $N = 120 + 4$, i.e. with $n = 31$ segments in the first quadrant. The results show that the system of smooth lines was better represented especially after the passing through the particle field. The remaining interior loop keeps an approximately elliptic shape until it annihilates in the step 5086 ($t = 152.58$ s).

Dislocation loop expansion

The next simulation considered a single dislocation loop in a field of precipitates, now under the action of applied shear stress $\sigma_{xz} = 100$ MPa. The simulation parameters were chosen the same as in the Tab. VI.4, except the initial loop radius, which was $R = 750$ nm. Thus the initial dislocation loop was placed inside the precipitate field and started expanding due to the applied stress.

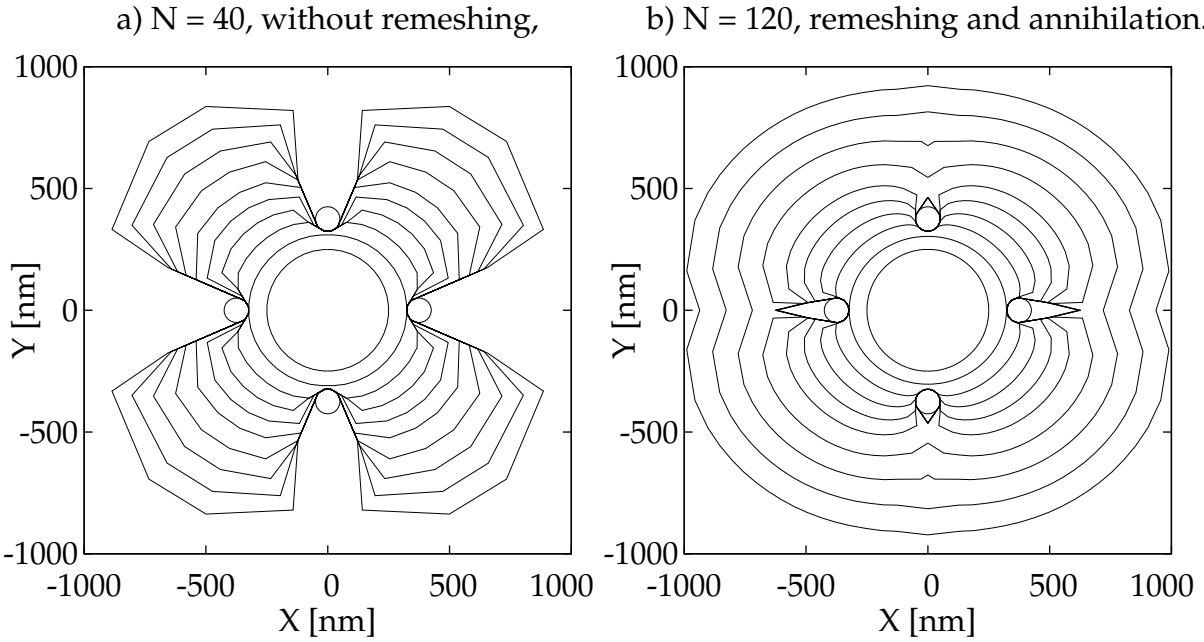

Figure VI.25: An expansion of a dislocation loop in a field of precipitates.

The results are shown in Fig. VI.25. The initial state is a circular dislocation loop in the centre of the figure. In the first simulation (Fig. VI.25a), the remeshing was deliberately switched off. As a result, the discretisation becomes very coarse and the dislocation line reaches an equilibrium state before it would surpass the spherical particles.

The same simulation, but with more fine discretisation in the initial state and with remeshing enabled, yields different results presented in Fig. VI.25b. The dislocation loop surpasses the spherical precipitates and keeps expanding.

VI.8.5 3D simulations with particles

Dislocation loop contraction in a particle field

A true 3D simulation, which demonstrates dislocation climb features incorporated in the model, addressed a dislocation system consisted of 7 coaxial dislocation loops, initially forming a cylinder (Fig. VI.26). The coordinates of the polygon vertices representing the loops are:

$$\begin{aligned} \boldsymbol{N}_{j,i} &= (R\cos\varphi_i, R\sin\varphi_i, jh)\,, \quad \varphi_i = \frac{2\pi[i+i_0-1]}{N} \\ i &\in \{1\ldots N\}, \qquad\qquad i_0 = +\frac{1}{2} \\ j &\in \{-3\ldots 3\} \end{aligned} \tag{VI.47}$$

The loops are situated in planes $Z = jh$, $h = 100$ nm, $j \in \{-3 \dots 3\}$. The simulation parameters are listed in Table VI.5.

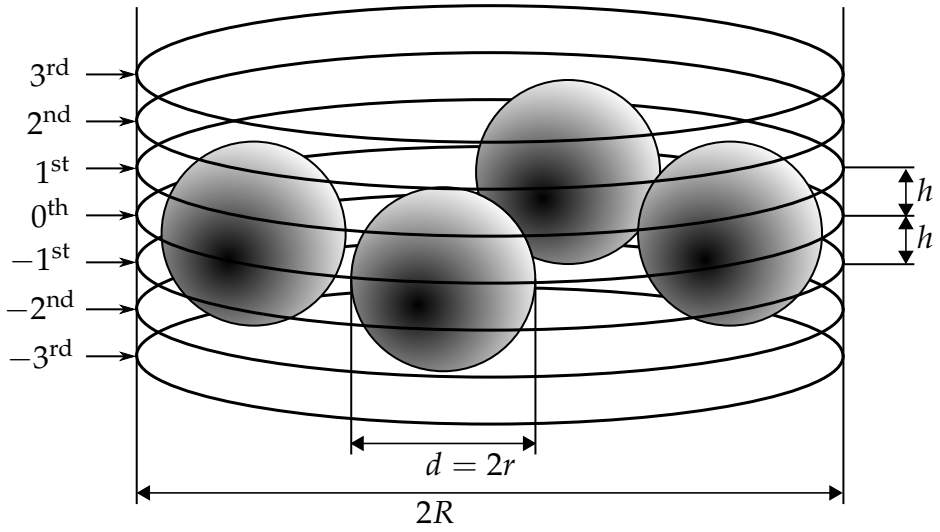

Figure VI.26: Dislocation cylinder with spherical precipitates.

The simulation is performed with the force decomposition based on the stress tensor decomposition. The system has planes of symmetry $X = 0$, $Y = 0$ and $Z = 0$, i.e. it can be represented only by the first octant. This approach is necessary to reduce rounding errors. As a side effect, the simulation has been running to 8 times faster than it would have been without the symmetry operations.

Table VI.5: Evolution of a dislocation loop cylinder – parameters.

μ	$0.8 \cdot 10^{11}$ Nm^{-2}	shear modulus
ν	0.3	Poisson ratio
D_0	$2 \cdot 10^{-4}$ m^{2}s^{-1}	diffusion coefficient for zero Q
Q	240 kJ mol^{-1}	activation energy of self-diffusion
T	873 K	temperature
Ω	$(3.5 \cdot 10^{-10}$ m$)^3$	atomic volume
$\boldsymbol{b}$	$(2, 0, 0) \cdot 10^{-10}$ m	Burgers vector
R	1500 nm	initial dislocation loop radius
N	$120 + 4$	# of line segments
Δt	60 ms	time step
l	$\langle 10, 120 \rangle$ nm	segment length range
d_a	10 nm	critical distance for annihilation
h	100 nm	loop distance
d	600 nm	diameter of the particles
λ	$\sqrt{2}e$	particle distance
$\boldsymbol{c}_i$	$\{[\pm e, 0, 0], [0, \pm e, 0]\}$	coordinates of the particle centers
e	1150 nm	particle eccentricity

Several snapshots of the dislocation system during the simulation are plotted in Fig. VI.27. The positions of dislocation segments are presented in projections into coordinate planes, where each row shows a XY projection followed by XZ and YZ projections. For

simplicity, only a half of the system is plotted, i.e. the dislocation lines with coordinates $Z \geq 0$.

Initially, the loops start contracting. Due to the symmetry of the system, the driving forces acting upon the 0^{th} (central) loop imply only a glide motion. Thus the 0^{th} loop stays in the plane $Z = 0$, and it is visible only in the XY plot, as in the XZ and YZ projections it coincides with the X and Y axes respectively. The outer loops are subjected to both glide and climb forces. The forces acting in the $\pm Z$ direction affect mostly the segments with prevailing screw character (i.e. parallel to the X axis). The climb mechanism drives the outermost $\pm 3^{\text{rd}}$ loops away from the particles. The neighbouring loops ($\pm 2^{\text{nd}}$) do get into contact with the particles only by the segments with prevailing edge character – the screw segments move away. As a result, only the 0^{th} and $\pm 1^{\text{st}}$ loops get pinned by the particles.

As can be seen in the second row ($t = 192$ s), the first annihilation occurs at the particles lying on the X axis for the $\pm 2^{\text{nd}}$ loops, as the outer loops tend to contract more quickly. Then the process repeats also for the inner loops, and they leave new loops on the particle interfaces.

Then the $\pm 3^{\text{rd}}$ loops annihilate without any contact with the particles ($t > 336$ s). Later, the remaining loops encircle also the particles lying on the Y axis and form new loops on their surfaces (this situation is not plotted). Finally, the contraction continues, and also the remaining loops in the center of the particle field annihilate.

Dislocation loop expansion in a particle field

A similar simulation with 7 co-axial loops has been performed with the same parameters as in the Table VI.5. Here, however, the initial dislocation loop radius has been set to $R = 750$ nm and an external shear stress $\sigma_{xz} = 100$ MPa has been applied. Like in the simulation with the single expanding loop in a field of precipitates mentioned in the section VI.8.4, the dislocation loop cylinder was also expanding.

Selected snapshots of the simulation are shown in Fig. VI.28. The central loop is fixed in the plane $Z = 0$ due to the system symmetry. The segments with the prevailing screw character move more quickly, and the $\pm 3^{\text{rd}}$ loops do not get into contact with the particles, whereas the remaining loops do. The applied stress field greatly exceeds the self-stress, so the dislocation loops are not only expanding, but they tend to keep their initial circular shape (in the XY projection) for a long time. The loops are passing through the particle field and leave new loops on the particle surfaces. Later, the dislocation configuration becomes very complex due to the combined glide and climb motion of the segments, as can be seen from the XZ and YZ projections. Suddenly, the stress field of the deformed loops produces such driving forces, that helices are formed on the $\pm 3^{\text{rd}}$ loops, making the configuration even more complex.

VI.9 Symmetry (II.)

Models of dislocation structures may often include a translational symmetry. It corresponds to a situation, when we need to study processes in macroscopic (bulk) samples. The real dislocation densities observed during high temperature plastic deformation are about $10^{13} - 10^{14}$ m^{-2} (see e.g. Fig. I.8 and [1–3]). A real sample thus contains too many dislocations, for which it is not possible to address segment-segment interactions for

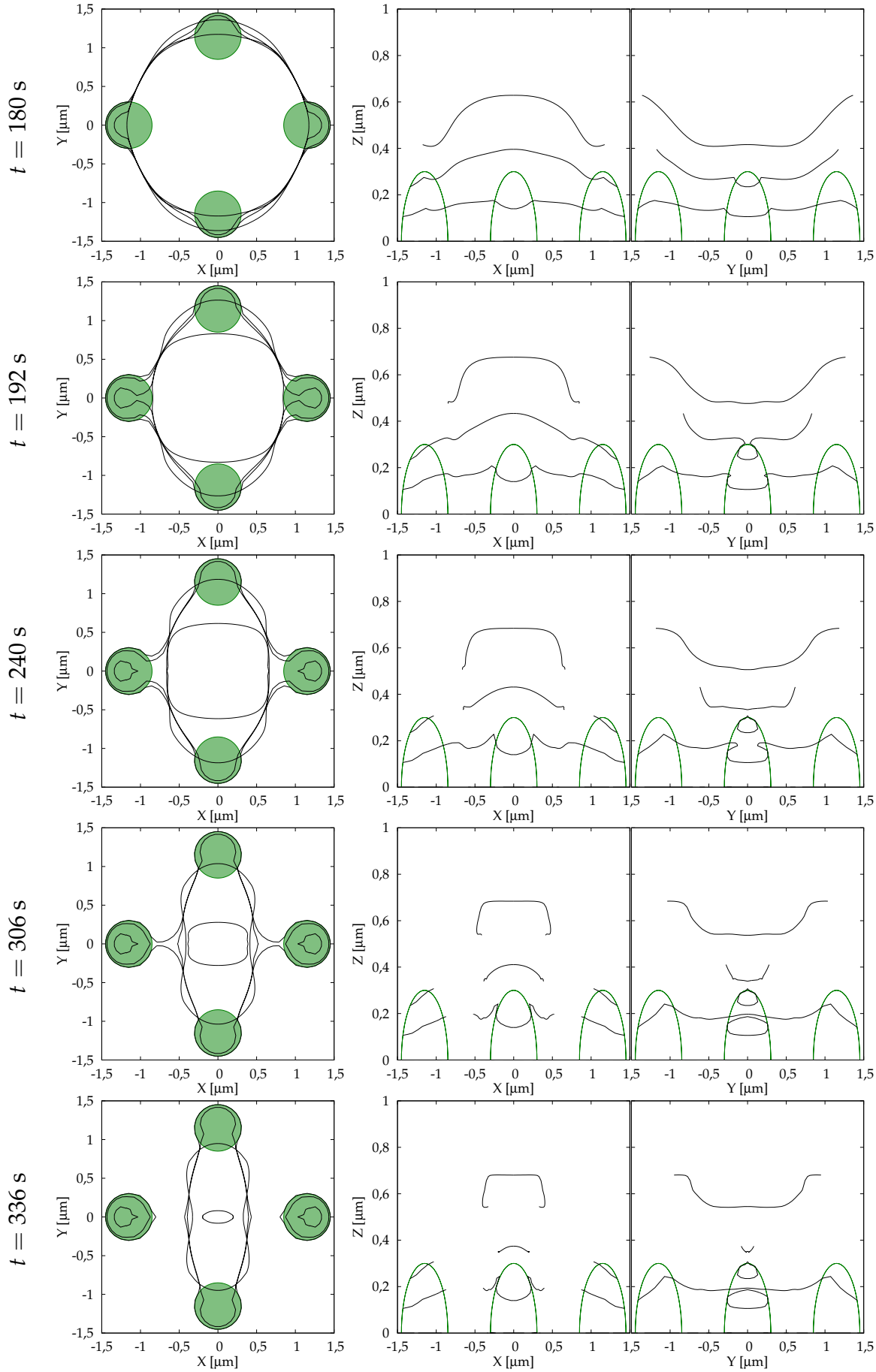

Figure VI.27: A contraction of multiple dislocation loops in a field of precipitates.

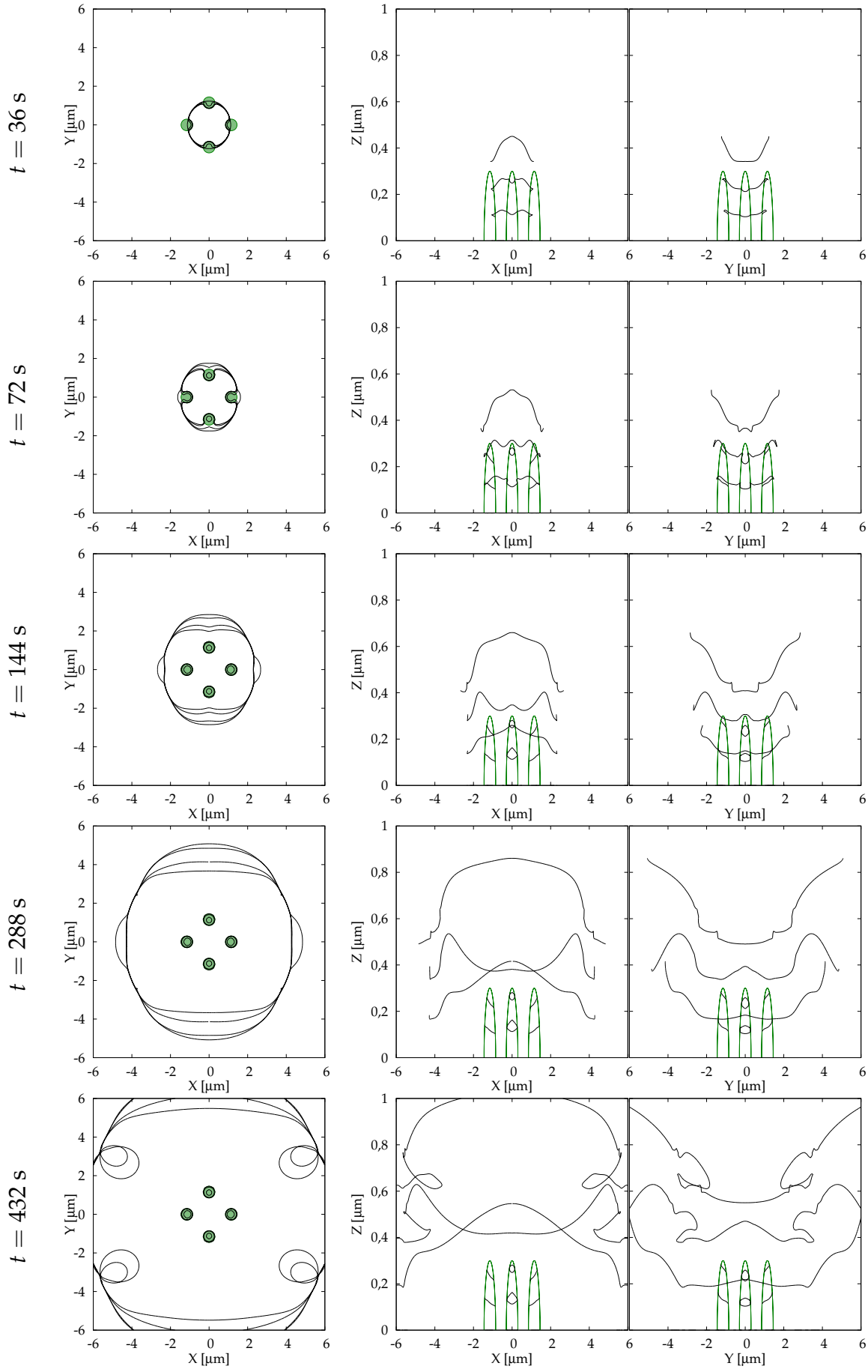

Figure VI.28: An expansion of multiple dislocation loops in a field of precipitates.

every pair of segments. Therefore, periodic boundary conditions are often employed to mimic the behaviour of bulk samples. The periodic boundary conditions build upon a replication of a suitable elementary cell. If we neglect interactions between segments with large mutual distance (i.e. several multiples of the dimensions of the elementary cell), we can use only a finite number of replications of the elementary cell to satisfactorily represent the dislocation system.

VI.9.1 Translational symmetry

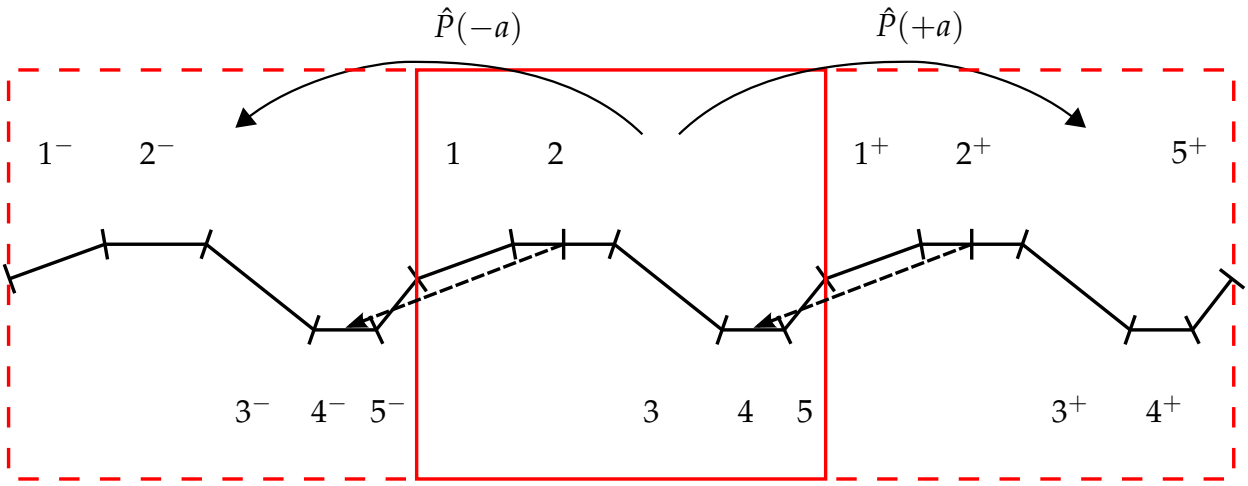

Figure VI.29: Periodic boundary conditions and a translational symmetry.

We consider a periodic system (Fig. VI.29). which can be fully described by the vertices and segments inside the elementary cell bound by the solid frame. The interaction between the segments inside the elementary cell can be directly evaluated. On the other hand, the force contributions from the segments outside the elementary cell cannot be expressed directly, since the corresponding data are not stored in the computer memory. However, the evaluation of forces acting upon the segments outside the elementary cell originating from the segments inside the elementary cell is straightforward. These forces are the same as the forces coming from translationally symmetric segment and acting on the segments in the elementary cell. For example, the force exerted by the segment $i' = i^+$ upon a j^{th} segment can be computed as

$$\begin{aligned} \boldsymbol{F}_{j,i'}(\boldsymbol{R}_{j,i'}, L_i) &= \hat{P}_{\mathrm{L}}^{-1}(-a)\left\{\left[\boldsymbol{b}\cdot\left(\hat{T}_i\tilde{\sigma}(\hat{T}_i^{-1}\boldsymbol{R}_{j',i}, L_i)\hat{T}_i^{-1}\right)\right]\times\left(\hat{P}_{\mathrm{L}}(-a)\boldsymbol{\xi}_j\right)\right\}, \\ \boldsymbol{R}_{j',i} &= \hat{P}(-a)\boldsymbol{R}_j - \boldsymbol{R}_i. \end{aligned} \tag{VI.48}$$

Here a is the cell width, $\hat{P}(-a)$ is a translation by a distance a in the negative (leftward) direction and $\hat{P}_{\mathrm{L}}$ is a linear component of the translation (i.e. an identity). This relation is formally identical to the former relation for the symmetry transformation of forces (VI.40). From this follows, that these operations of symmetry can be combined.

VI.9.2 A comparative simulation

The first system, where the translational symmetry was applied, was a structure consisting of several dislocation loops arranged in a planar lattice. The simulation parameters similar to the preceding calculations with a single dislocation loops are summarized in Table VI.6.

Table VI.6: Simulation parameters for several dislocation loops arranged in a regular planar pattern.

μ	$0.8 \cdot 10^{11}$ Nm^{-2}	shear modulus
ν	0.3	Poisson ratio
D_0	$2 \cdot 10^{-4}$ m^{2}s^{-1}	diffusion coefficient for zero Q
Q	240 kJ mol^{-1}	activation energy of self-diffusion
T	873 K	temperature
Ω	$(3.5 \cdot 10^{-10}$ m$)^3$	atomic volume
$\boldsymbol{b}$	$(2,0,0) \cdot 10^{-10}$ m	Burgers vector
R	500 nm	dislocation loop radius
N	40	# of line segments
n^2	$\{9, 25\}$	# of loops in the lattice
$\boldsymbol{N}_{j,i}$	$C_j + R[\cos\varphi_i, \sin\varphi_i, 0]$	vertex coordinates, $\varphi_i = \frac{2\pi(i-\frac{1}{2})}{N}$
C_j	$\frac{5}{2}R[(j-1) \bmod n - \lfloor\frac{n}{2}\rfloor, \lfloor\frac{j-1}{n}\rfloor, 0]$	coordinates of loop centers, $j \in \{1, \ldots, n^2\}$
Δt	30 ms	time step
l	$\langle 30, 120\rangle$ nm	segment length range

Four simulations were carried out in total: two simulations for two different numbers of dislocation loops arranged in a regular planar pattern. At first, $3 \times 3 = 9$ loops were set up in the system, secondly $5 \times 5 = 25$ loops were considered. In both cases, the simulations were carried out twice: 1) without the translational symmetry (all loops were set up in the system) and 2) with the translational symmetry, where only the central loop had been set up and replicated into the other sites in the regular planar pattern 3×3 or 5×5.

The obtained results are plotted in Fig. VI.30. The initial configuration is denoted by a black line. The final configuration in a step 3500 ($t = 105$ s) is denoted by a red line for the simulation without the translational symmetry and by a blue line for the simulation with the translational symmetry. The results show that the difference between the central loops in the simulations with and without the translational symmetry is rather small – this loop contracts slower than a single dislocation loop, as the loop is attracted by the neighbouring loops, particularly by their nearest segments. The loops near the end of the finite planar pattern contract faster in the simulation without the translational symmetry, because they have less neighbouring dislocations which would attract them. However, the contribution to the slowing down of the contraction of the central loop originating from the farther loops is much smaller. Extension of the pattern to the 5×5 loops leads to an even slower contraction of the central loop, even though the deceleration is small. A similar effect has the replication of the central loop by the operations of translational symmetry – the neighbouring replications slow down the contraction of the central loop, see the positions of the central loop in the last simulation step 3500 in detailed Fig. VI.31.

These results suggest that a sufficient finite number of translational replications of an elementary cell plausibly approximates exact periodic boundary conditions.

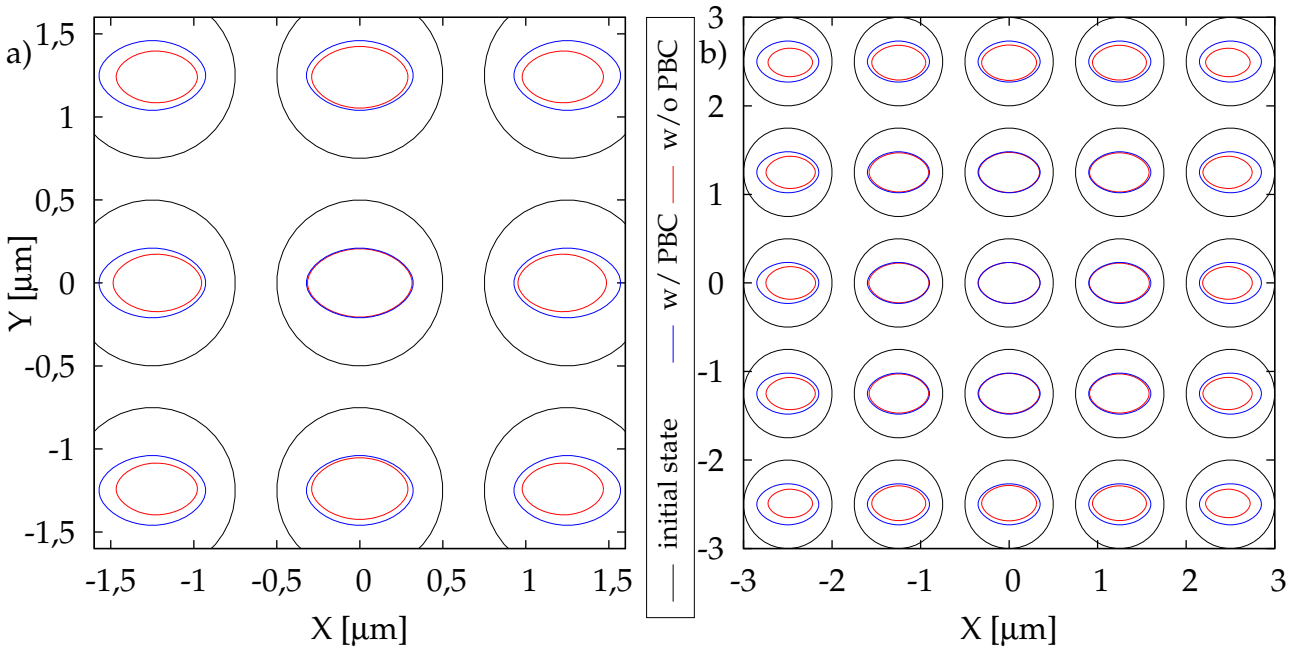

Figure VI.30: A simulation with a planar lattice arrangement of dislocation loops: a) 3×3 loops, b) 5×5 loops. The snapshot is taken in time $t = 105$ s. Positions of the loops in the simulation step 3500 is shown for translational replication (blue curves) and no boundary conditions (red curves).

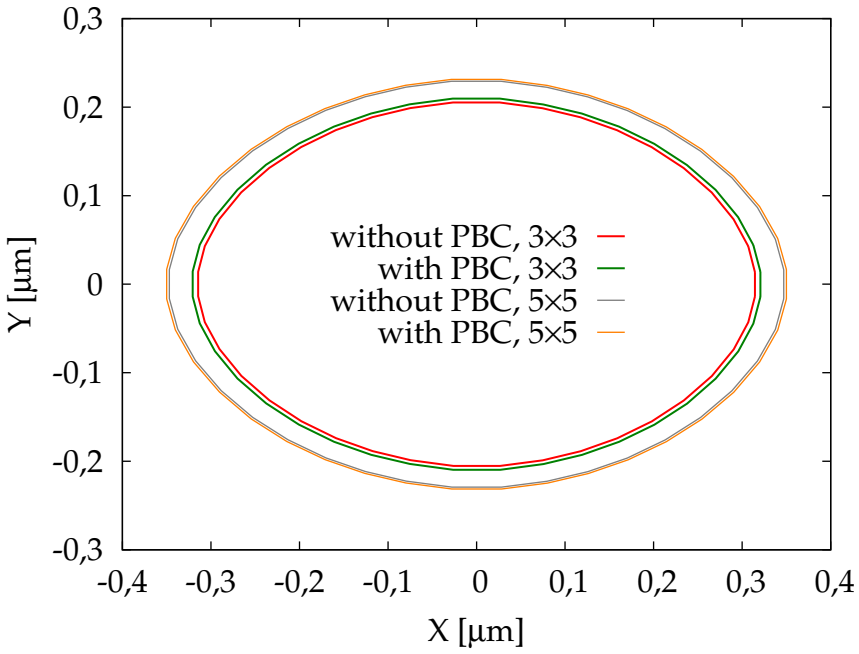

Figure VI.31: A simulation with a planar lattice arrangement of dislocation loops – a detailed view of the central loops in $t = 105$ s, simulation step 3500.

VII. Modelling of low-angle dislocation boundaries

The model presented in the preceding sections has been adapted for a system of fully flexible dislocation lines forming a tilt dislocation boundary. The model addresses the boundary migration under the action of applied stress at high temperatures. The numerical simulations also consider the interactions between the dislocation system and a field of spherical precipitates.

VII.1 Geometry of the low-angle boundary

The low-angle dislocation boundary, in its starting configuration, consists of straight, parallel and equidistant dislocations (see Fig. VII.1). The dislocation line spacing is h, the particle diameter is d and the particle spacing is λ_Y and λ_Z in the direction of Y and Z, respectively.

The calculation is performed on an elementary cell, which is replicated in a 3×3 pattern. The replication is possible due to the translational symmetry (section VI.9), which allows the simplified system to approximate an infinite periodic system. The simulation cell has also two planes of symmetry, $Y = 0$ and $Z = 0$ (section VI.6). This approach greatly accelerates the computation and reduces memory requirements of the simulation.

The geometry of the elementary cell is depicted in Fig. VII.2. The initial coordinates describing the polygonal chains representing the dislocation lines are determined by a relation

$$\boldsymbol{N}_{j,i} = \left(0, a_Y\left(\frac{i}{N} - \frac{1}{2}\right), jh\right), \quad i \in \{0, \ldots, N\}, \quad j \in \left\{-\left\lfloor\frac{n}{2}\right\rfloor, \ldots, +\left\lfloor\frac{n}{2}\right\rfloor\right\}, \tag{VII.1}$$

where n is a number of dislocation lines in the elementary cell and N is a number of dislocation segments per one line. Actually, only coordinates with $i \geq \lceil N/2 \rceil$ and $j \geq 0$ are represented in the computer memory due to the system symmetry. Let us introduce a new coordinate ψ along a single dislocation line:

$$\boldsymbol{N}_j(\psi) = (0, a_Y(\psi - 1/2), jh), \quad \langle 0, 1\rangle \ni \psi = \frac{i}{N} \tag{VII.2}$$

and i, j the same as in (VII.1). The parametric coordinate ψ will be further used in force plots.

The particle distances $\lambda_Y = \lambda_Z = 200$ nm are the same for all of the simulations. Except the section VII.2.3, the particle diameter is always $d = 100$ nm. The parametric study presented in the next sections considers variable number of dislocation lines in the elementary cell n (related to the initial line spacing h) and variable applied shear stress σ_{xz}. All other input parameters are listed in Table VII.1. Considering the values of $\boldsymbol{b}$ and h, the misorientation angle[1] Θ of these low-angle dislocation boundaries lies in a range from 0.3° to 0.9°.

[1] See relation (I.8).

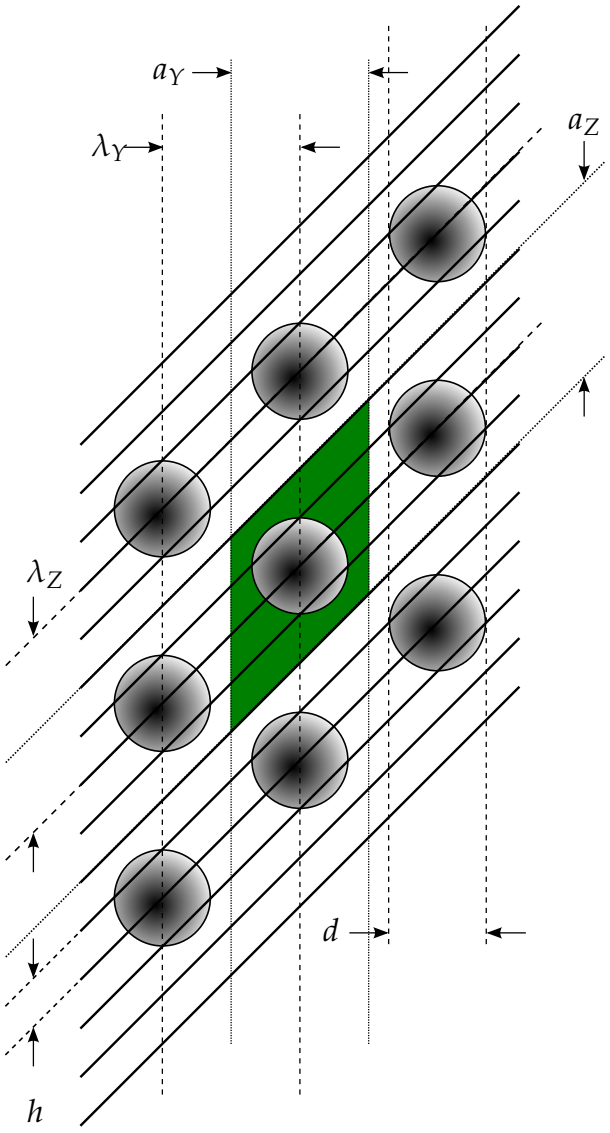

Figure VII.1: A low-angle dislocation boundary with a field of precipitates. The elementary calculation cell is highlighted.

VII.2 Simulations and results

The numerical simulations have been performed with different force decompositions. The very first calculations used the stress tensor decomposition. Later, the same calculations were run with the force decomposition based on crystallographic slip planes. Finally, a decomposition using edge and screw components of the Burgers vector has been used for a detailed parametric study.

VII.2.1 Results based on the stress tensor decomposition

The simulations have been run for line spacings from a range $h \in (12, 34)$ nm with applied shear stress between $\sigma_{xz} \in \langle 20, 100 \rangle$ MPa. The stress tensor decomposition has been used (see section VI.2.2) with the relation between the mobility prefactors $A = 10B$, like in the former simulations.

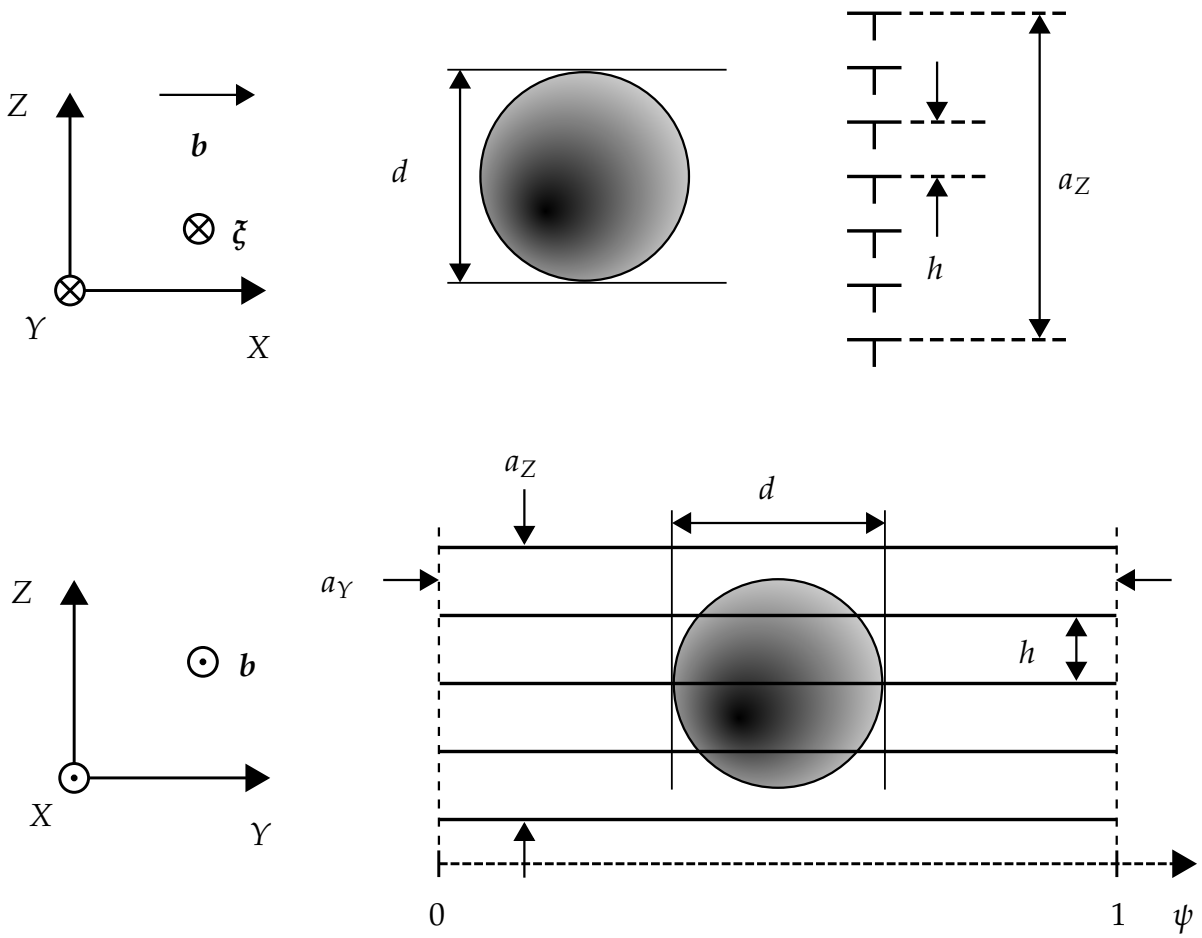

Figure VII.2: 2D projections of the low-angle dislocation boundary.

Table VII.1: Evolution of a low-angle dislocation boundary – input parameters.

μ	$0.8 \cdot 10^{11}$ Nm^{-2}	shear modulus
ν	0.3	Poisson ratio
D_0	$2 \cdot 10^{-4}$ m^{2}s^{-1}	diffusion coefficient for zero Q
Q	240 kJ mol^{-1}	activation energy of self-diffusion
T	873 K	temperature
Ω	$(0.35\text{ nm})^3$	atomic volume
$\boldsymbol{b}$	$(0.2; 0; 0)$ nm	Burgers vector
$a_Y; a_Z$	200 nm	elementary cell dimensions
N	32	# of line segments per line
n	$\{7, \ldots, 17\}$	# of lines in a cell
Δt	3 ms	time step
l	$\langle 3, 8 \rangle$ nm	segment length
d_a	3 nm	critical distance for annihilation
h	$a_Z/(n-1)$ nm	line distance
$\lambda_Y; \lambda_Z$	200	particle distance
d	100 nm	particle diameter
$\boldsymbol{C}$	$[-d; 0; 0]$ nm	particle center position

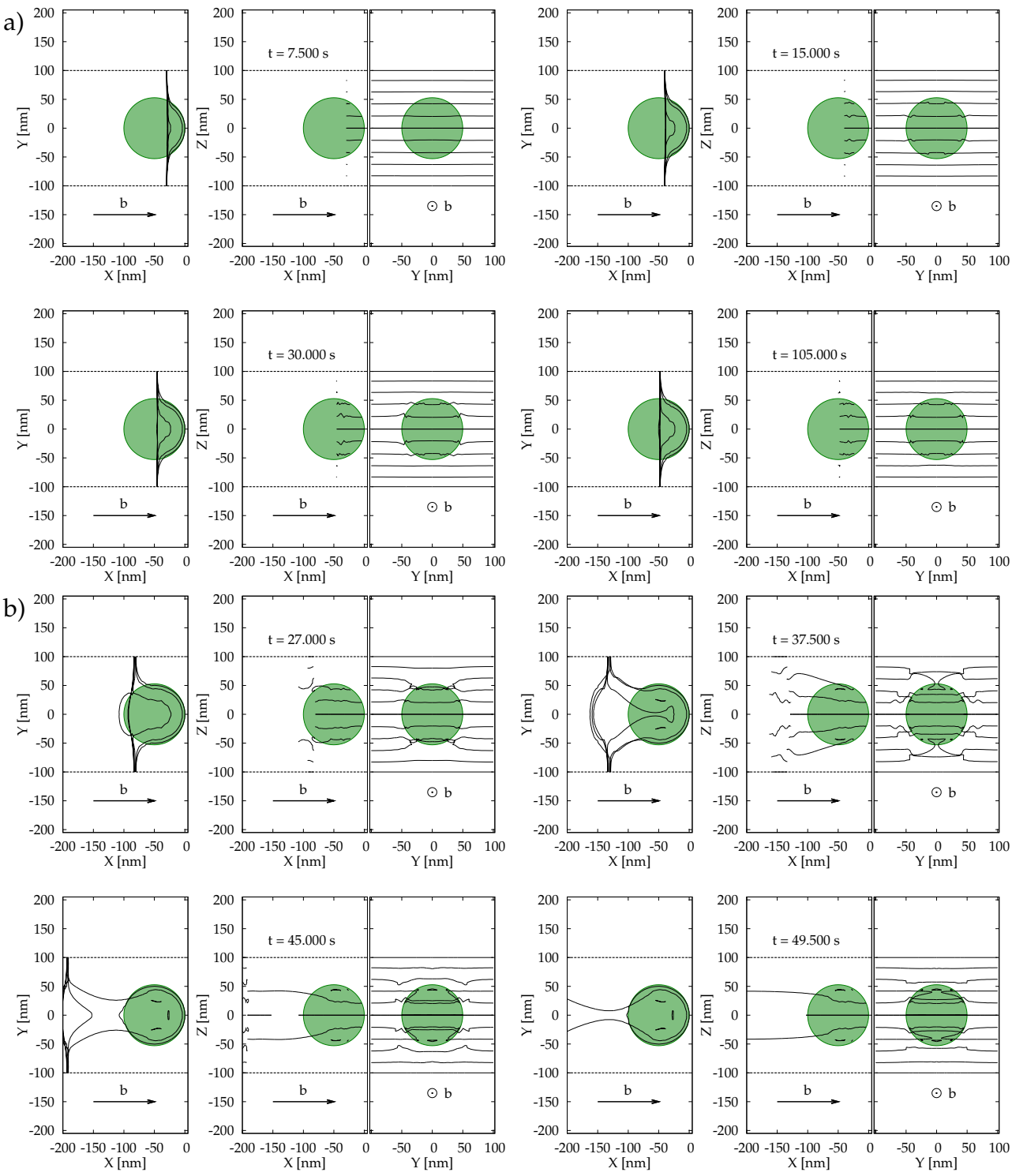

Figure VII.3: An evolution of the low-angle tilt boundary with $h = 20\,\text{nm}$: a) stable configuration with $\sigma_{xz} = 41.2\,\text{MPa}$, b) unstable configuration with $\sigma_{xz} = 54.5\,\text{MPa}$.

The Figure VII.3 shows evolution of the low-angle dislocation boundary with $h = 20$ nm for two different values of the applied stress. The Fig. VII.3a shows a system subjected to the applied stress of 41.2 MPa, which converged to an equilibrium state. The applied stress σ_{xz} is not high enough to make the dislocation pass through the field of precipitates. Therefore, the particle structure immobilizes the dislocation wall. An

important fact is that even the dislocations, which are not in contact with the precipitates, cannot move through the precipitate field. There is an attractive force acting on dislocation segments, which are slightly displaced from the wall structure (see section IV.6.3). However, the attractive forces are in equilibrium with the forces coming from the applied stress, so the total driving forces vanish in the equilibrium state. As an example, the forces along the dislocation line lying in the plane $Z = a_Z/2$, which does not get into contact with the precipitates, are plotted in Fig. VII.4). The initial driving forces come only from the applied stress. These initial forces are the same for every segment in the system and their magnitude is $b \cdot \sigma_{xz}$. Thus the logarithm of the ratio between an actual force and the initial force must be zero in the initial state. At the end of the simulation ($t = 105$ s), the actual driving forces are more than three orders of magnitude smaller than in the simulation start, leaving the system effectively in equilibrium.

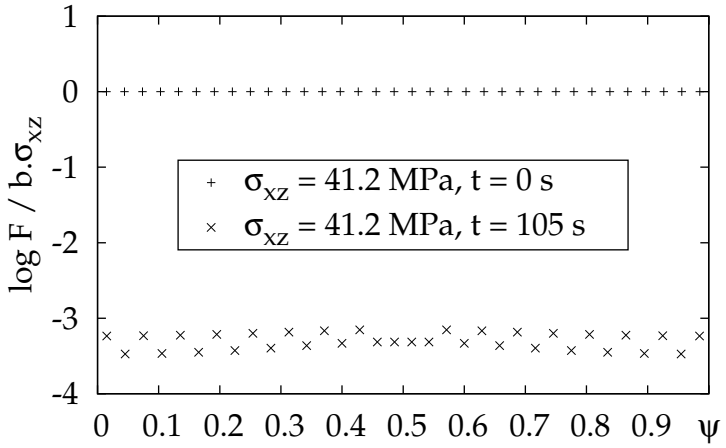

Figure VII.4: Force along the dislocation line in the plane $Z = a_Z/2$, $h = 20$ nm.

On the other hand, higher applied stress allows the dislocation wall to pass through the particle field. Such situation is shown in Fig. VII.3b. The result is a low-angle dislocation boundary migrating further through the crystal. During the passing stage, a series of dislocation loops is stored at the particle interfaces. Here it is obvious, that the forces attracting the "free" dislocation segments back to the regular wall configuration are outbalanced by the applied stress.

The results in Fig. VII.3 suggest that there is a critical stress $\sigma_C(h)$ which must be surpassed to make the dislocation wall pass through the impeding precipitates. However, some combinations of applied stress and the initial wall configuration may lead to a decomposition of the dislocation boundary during the passing process, like the situation shown in Fig. VII.5. Here is the applied stress of 54 MPa still above the critical threshold and just slightly lower than in the case depicted in Fig. VII.3. One of the dislocations does not encircle the precipitate, but it is slowly pulled out of the dislocation boundary. The self-stress due to the high local curvature at the boundary of the elementary cell prevails and the particular dislocation line starts to move in the opposite direction than the passing dislocation wall.

This particular behaviour has been mostly observed for dislocation boundaries with lower density subjected to applied stresses above the critical stress. The evolution regimes are summarized in Fig. VII.6[2].

[2]For stresses above 80 MPa all wall configurations passed through the particle field and the results are not shown in the plot.

The interactions between lines in the dislocation wall become stronger with decreasing line spacing h, i.e. with growing dislocation density. The stronger interactions make the critical stress higher, and also stabilize the dislocation wall, so it is less probable that

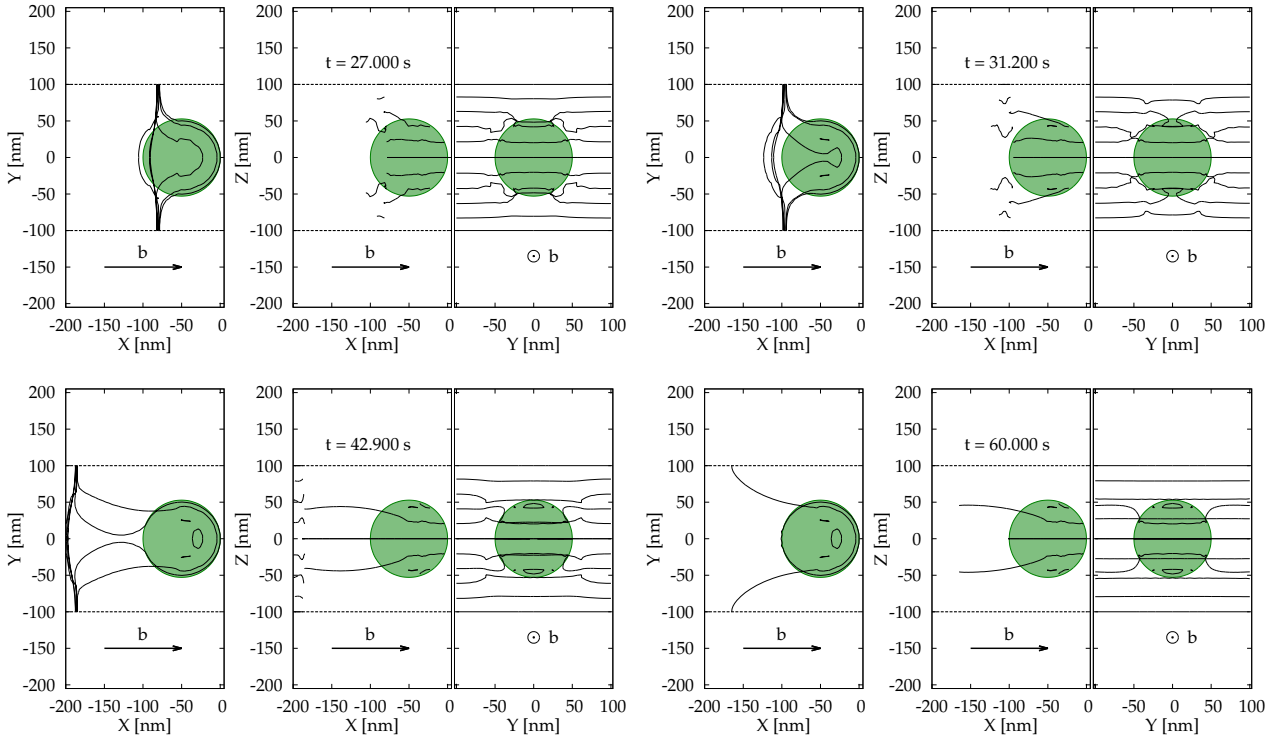

Figure VII.5: An evolution of the low-angle tilt boundary with $h = 20\,\text{nm}$ and $\sigma_{xz} = 54\,\text{MPa}$.

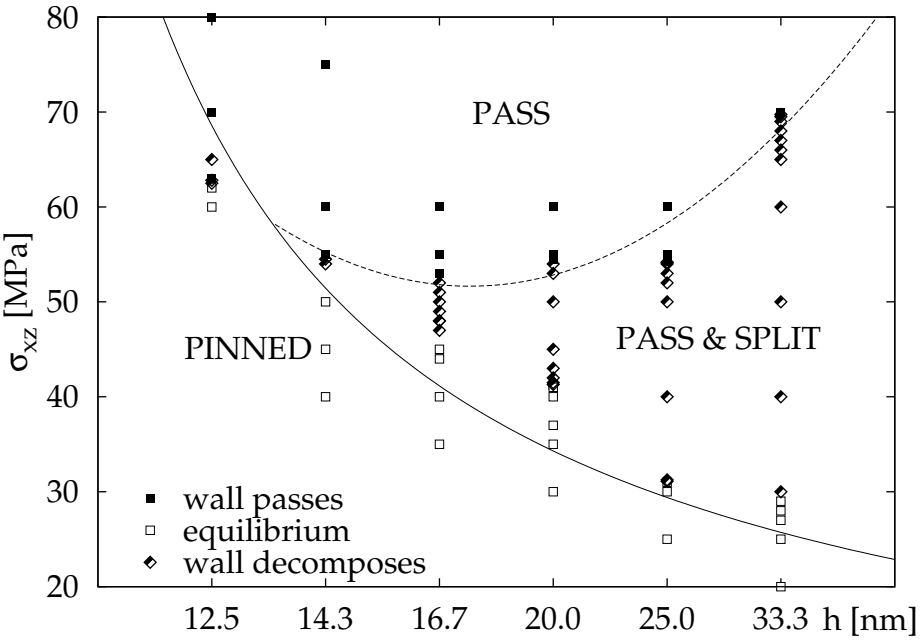

Figure VII.6: Regimes of evolution of the low-angle dislocation boundary – calculated in the stress tensor decomposition regime, see section VI.2.2.

a dislocation line will be pulled out of the wall. The sparse dislocation walls, which correspond to lower misorientation angles, decompose more easily.

The critical stress can be approximated by a relation

$$\sigma_{\mathrm{C}} \sim \frac{1}{h}, \tag{VII.3}$$

and is thus inversely proportional to the dislocation spacing h or proportional to the density of dislocations per unit length of the boundary.

The actual dependence has been fitted by a least square method with a following relation:

$$\sigma_{\mathrm{C}}(h) = \frac{a_\sigma}{h}, \tag{VII.4}$$

where

$$a_\sigma \doteq (770 \pm 20)\ \mathrm{MPa} \cdot \mathrm{nm}, \quad \rho(a_\sigma) \doteq 3\,\% \tag{VII.5}$$

The rather high deviations come from the fact, that the approximation (VII.4) is not exact and does not address a discrete nature of the interaction process. The motion of dislocations at the particle-matrix interface is restricted. A part of a dislocation line, which gets into contact with a precipitate, remains on the particle surface during a considerable portion of the simulation. As a result, the critical stress $\sigma_{\mathrm{C}}(h)$ is to some degree quantised by the number of dislocation lines having a direct contact with the precipitates.

VII.2.2 Results based on the crystallographic force decomposition

The simulations have been performed with the same parameters as before, i.e. with line spacing $h \in (12, 34)$ nm and with applied shear stress $\sigma_{xz} \in \langle 20, 100 \rangle$ MPa. The force decomposition based on crystallographic slip planes has been used (see section VI.2.3). The dislocation kinetics has been controlled by the glide prefactor $A_1 = 10B$ and non-compact glide prefactor equal to the diffusion prefactor, i.e. $A_2 = B$. The slip system is determined by the Burgers vector $\boldsymbol{b} = (0.2, 0, 0)$ nm and the slip planes $N_K = \{(0,1,0), (0,0,1), (0,1,1), (0,1,-1)\}$.

The simulation results exhibit some similarity to those based on the stress tensor decomposition. However, the dislocation velocities are generally lower due to the non-compact glide, since this deformation mode is not included in the former method. This also reduces effects of forces attracting dislocations towards the dislocation boundary. The consequences are demonstrated in Fig. VII.7, which shows a sparse dislocation wall with $h = 33.3$ nm under applied stress $\sigma_{xz} = 100$ MPa. As expected, the dislocation wall passes through the precipitate field, but decomposes. At first, the uppermost (lowermost) line in the simulation cell (lying in plane $Z = \pm a_Z/2$) detaches from the dislocation wall and moves quickly in the negative X direction. Later the same situation happens with the dislocation lying in the central plane ($Z = 0$). Only after this, the remaining lines propagate through the particle field and form even sparser dislocation wall structure. This effect applies generally for the sparse dislocation walls (approx. $h > 20$ nm) under high applied stress. Lower shear stresses ($\sigma_{xz} < 70$ MPa) make the dislocation walls propagate without a decomposition. On the other hand, results presented in Fig. VII.8 suggest that a region just above the critical stress $\sigma_{\mathrm{C}}(h)$ is characteristic for dislocation wall splitting. This result is similar to the outcome yielded by the simulations based on the stress tensor decomposition (see Fig. VII.6).

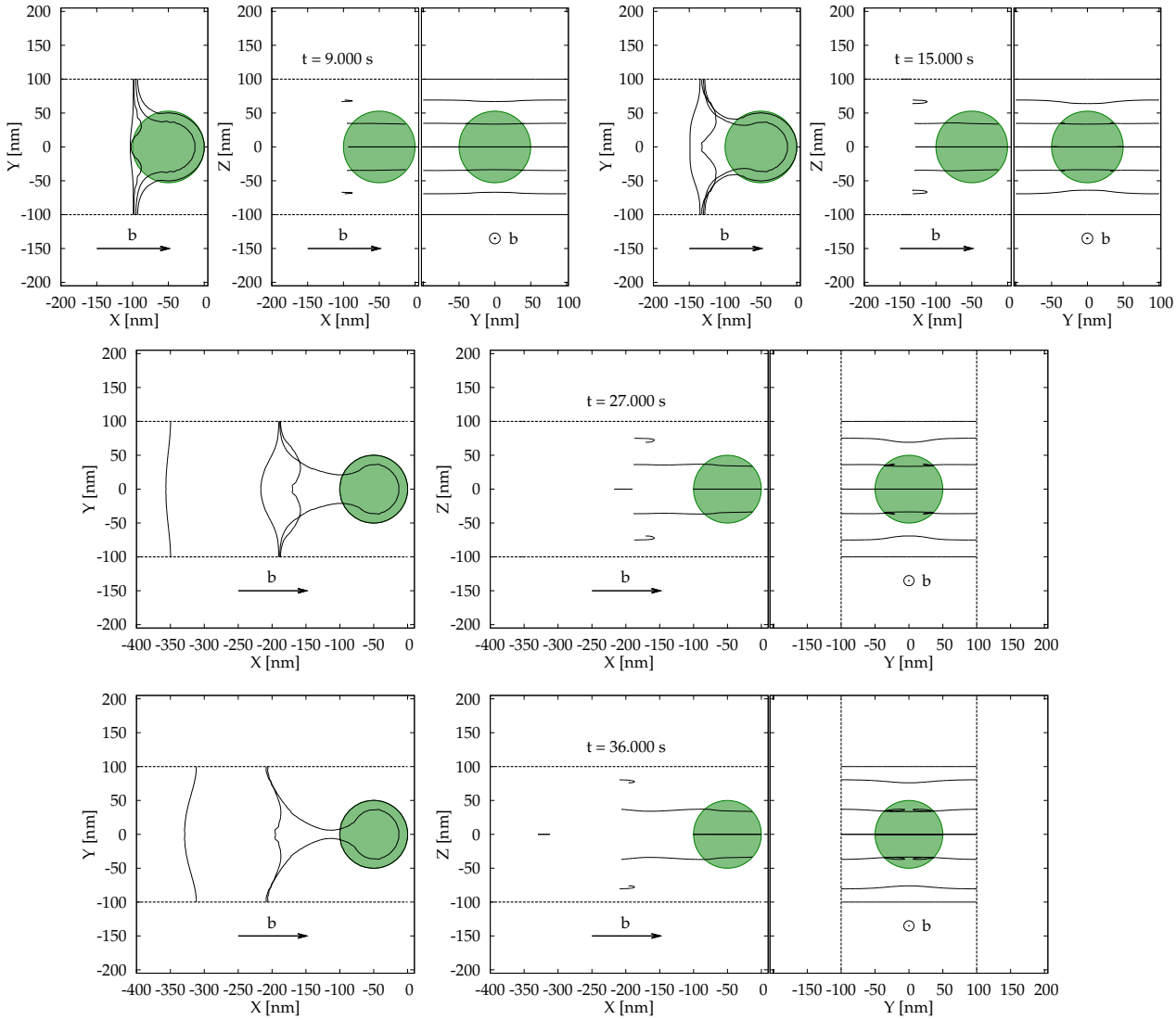

Figure VII.7: An evolution of the low-angle tilt boundary: $h = 33.\overline{3}\,\text{nm}$, $\sigma_{xz} = 100\,\text{MPa}$.

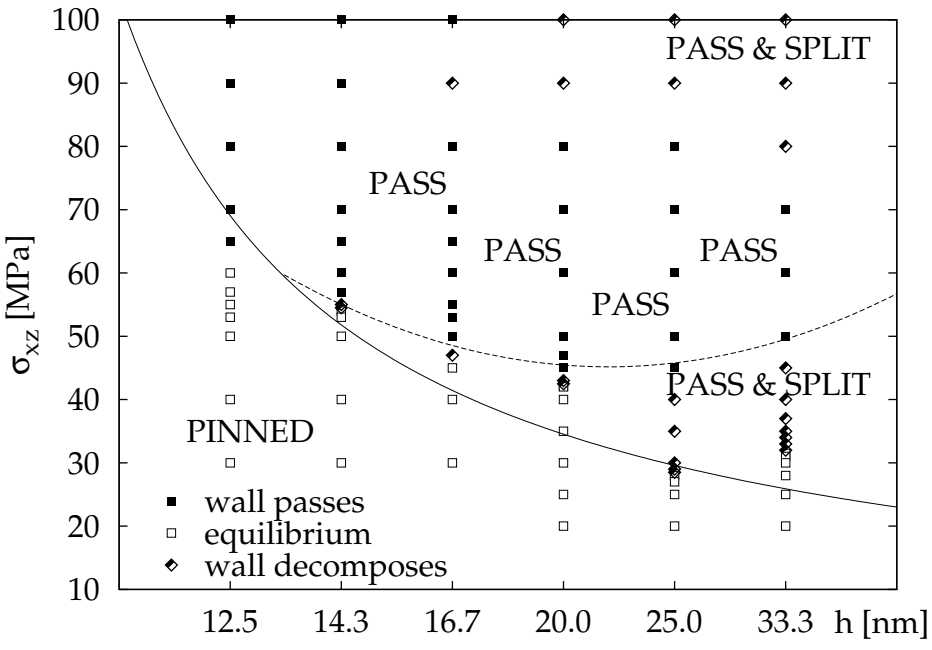

Figure VII.8: Regimes of evolution of the low-angle dislocation boundary – force decomposition based on crystallographic slip planes.

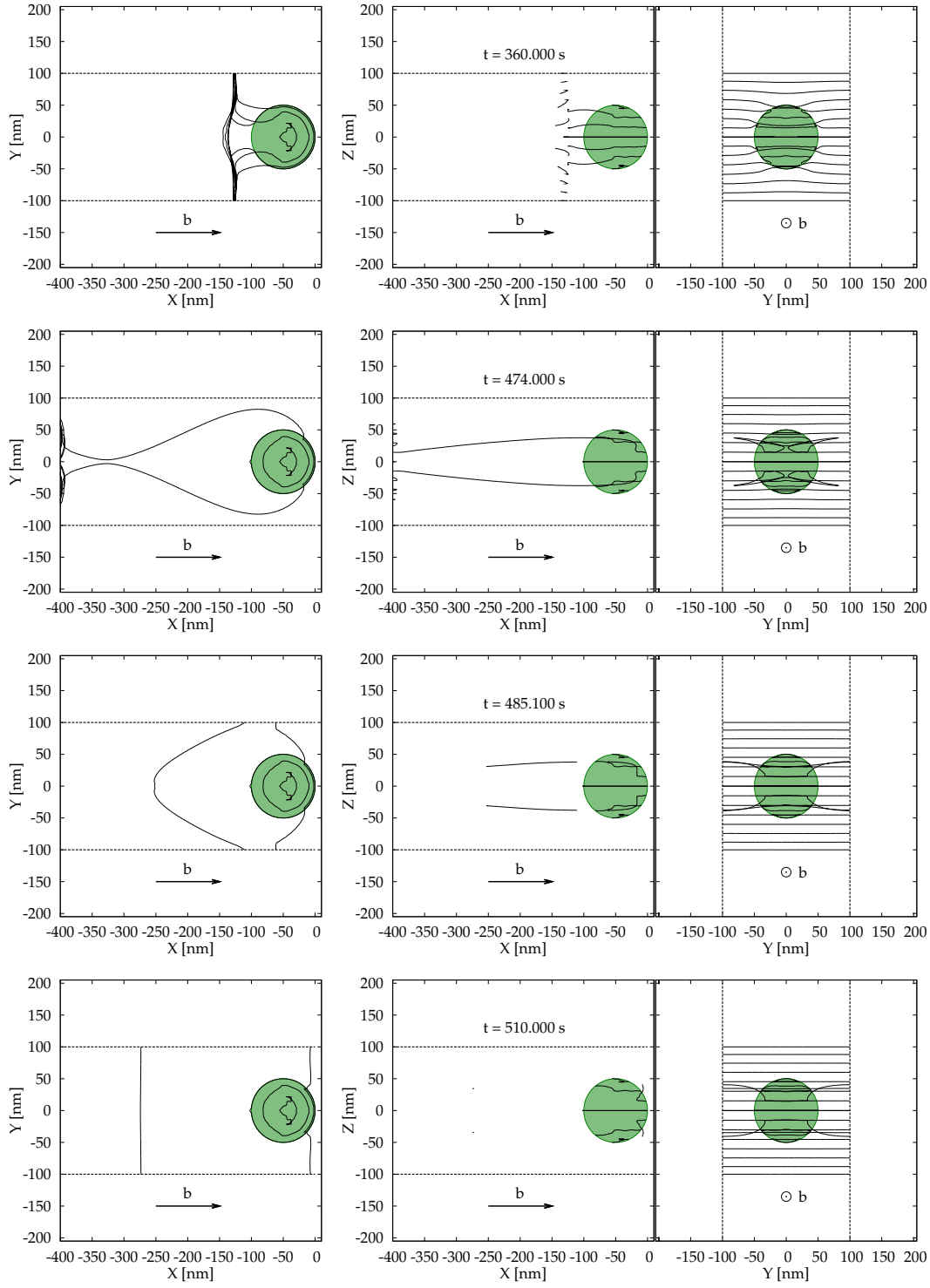

Figure VII.9: An evolution of the low-angle tilt boundary with $h \doteq 14.29\,\text{nm}$ and $\sigma_{xz} = 55\,\text{MPa}$.

The dislocation boundaries with smaller line spacing h are more stable, but their behaviour also changes with the applied variant of mobility approach. In Fig. VII.9 it is possible to see a competition between the forces attracting the dislocation line to the dislocation wall and the forces based on the system periodicity. The dislocation boundary motion slows down, but finally the dislocation line disconnects from the precipitates

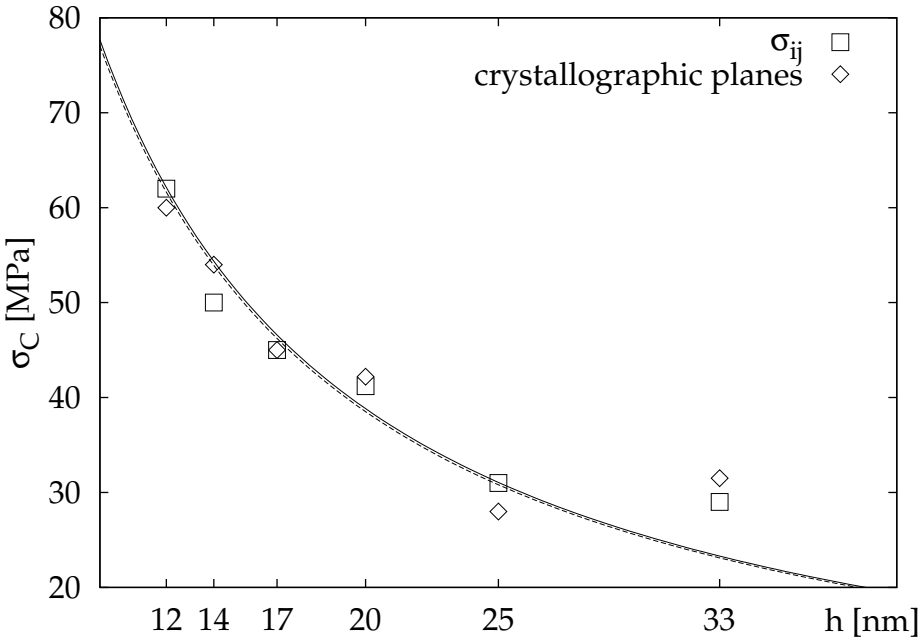

Figure VII.10: Comparison between critical stresses computed using the stress tensor decomposition (dashed line) and the force decomposition to crystallographic planes (solid line).

and propagates further as a part of the dislocation boundary. The remaining loop starts to contract back to the particle surface, but the attractive forces between the neighbouring cells make the dislocation line annihilate one more time, actually forming two new dislocation lines, one propagating in the negative X direction like the original dislocation boundary, and the second in the positive X direction towards the initial position. In contrast to the situation with dislocation wall decomposition, these two new dislocation lines increase dislocation density.

Like in the simulations based on the stress tensor decomposition, the critical stress $\sigma_C(h)$ is an inverse function of the line spacing h (VII.3). The least-squares fit with relation (VII.4) yielded

$$a_\sigma \doteq (780 \pm 30)\ \text{MPa} \cdot \text{nm}, \quad \rho(a_\sigma) \doteq 4\,\% \tag{VII.6}$$

These results closely correspond to the critical stress computed by means of the stress tensor decomposition. This is also reflected in the plot in Fig. VII.10.

VII.2.3 Results based on the force decomposition according to crystallographic slip planes and the components of the Burgers vector

These simulations employed the most advanced method of the force decomposition and related calculations of dislocation velocity. The forces are decomposed according to crystallographic slip planes and also the edge and screw parts of a general mixed dislocation segment. The method is described in detail in section VI.2.4. The segment velocity is cal-

Table VII.2: Critical applied shear stress – parameters and accuracy of the fit.

d [nm]	a_σ [MPa · nm]	$\rho(a_\sigma)$
120	980 ± 30	3 %
100	730 ± 20	3 %
80	500 ± 40	7 %
60	320 ± 24	7 %
50	190 ± 25	13 %

culated using the relation (VI.23), which is recalled here:

$$\boldsymbol{v} = \left(\frac{b_s}{b}\right)^2 A_s \boldsymbol{F}_s + \left(\frac{b_e}{b}\right)^2 \left(A_{e,\mathrm{G}} \boldsymbol{F}_{e,\mathrm{G}} + A_{e,\mathrm{C}} \boldsymbol{F}_{e,\mathrm{C}}\right).$$

The relation involves prefactors for a contribution from the screw component of the force, this is A_s. The edge component has two distinct prefactors $A_{e,\mathrm{G}}$ and $A_{e,\mathrm{C}}$ for the glide and climb contributions, respectively. These prefactors are constructed by scaling the diffusion factor $\beta(b)$, see formula (VI.14). The scale factor for a crystallographic glide is $a_g = 10$, while $a_{nc} = 2$ for the non-compact glide and $a_c = 1$ for dislocation climb. The slip system is the same as in the section VII.2.2.

The purpose of these calculations was a detailed parametric study focused not only on the relation between the critical stress σ_C and the initial dislocation spacing h, but also on the influence of the particle size d. The applied shear stress was in the range $\sigma_{xz} \in \langle 5, 100 \rangle$ MPa. Following particle diameters were selected: $d \in \{50, 60, 80, 100, 120\}$ nm. The dislocation line spacing was $h \in (12, 34)$ nm.

The simulation results are qualitatively similar to the preceding two simulations with stress tensor decomposition (section VII.2.1) and the force decomposition reflecting the crystallography (section VII.2.2). However, in this last approach the dislocation mobility is even more constrained by the crystallography. This further slows down the dislocation motion. Like in the former cases, the LADB was either stopped by the precipitates, or it passed through the precipitate field, possibly decomposing to several dislocation walls with higher line spacing h. Again, the decomposition is more frequent for sparse dislocation walls, from whose the individual dislocation lines can be rejected more easily. The LADB interaction with the precipitates may also lead to formation of kinks on the dislocation lines. This phenomenon is documented in the snapshots in Fig. VII.11. The formation of kinks further reduces the dislocation velocity.

The plot in Fig. VII.12 shows a comparison of critical stresses for simulations with different force decomposition techniques. The results are computed for simulations with precipitate diameter $d = 100$ nm. The results suggest that the separation of force contributions according to the edge $\boldsymbol{b}_e$ and screw component $\boldsymbol{b}_s$ of the Burgers vector does not significantly change the critical stresses.

The maps depicting these the LADB regimes for all investigated precipitate diameters are displayed in Fig. VII.13. The critical stress $\sigma_\mathrm{C}(h)$ has been approximated by the relation (VII.4). The results for individual particle diameters are listed in Table VII.2.

The strong dependence of the critical stress $\sigma_\mathrm{C}(h, d)$ on the precipitate diameter is illustrated in Fig. VII.14. An increase of the precipitate diameter leads to higher critical stress needed for the LADB to overcome the precipitate field. The connection between

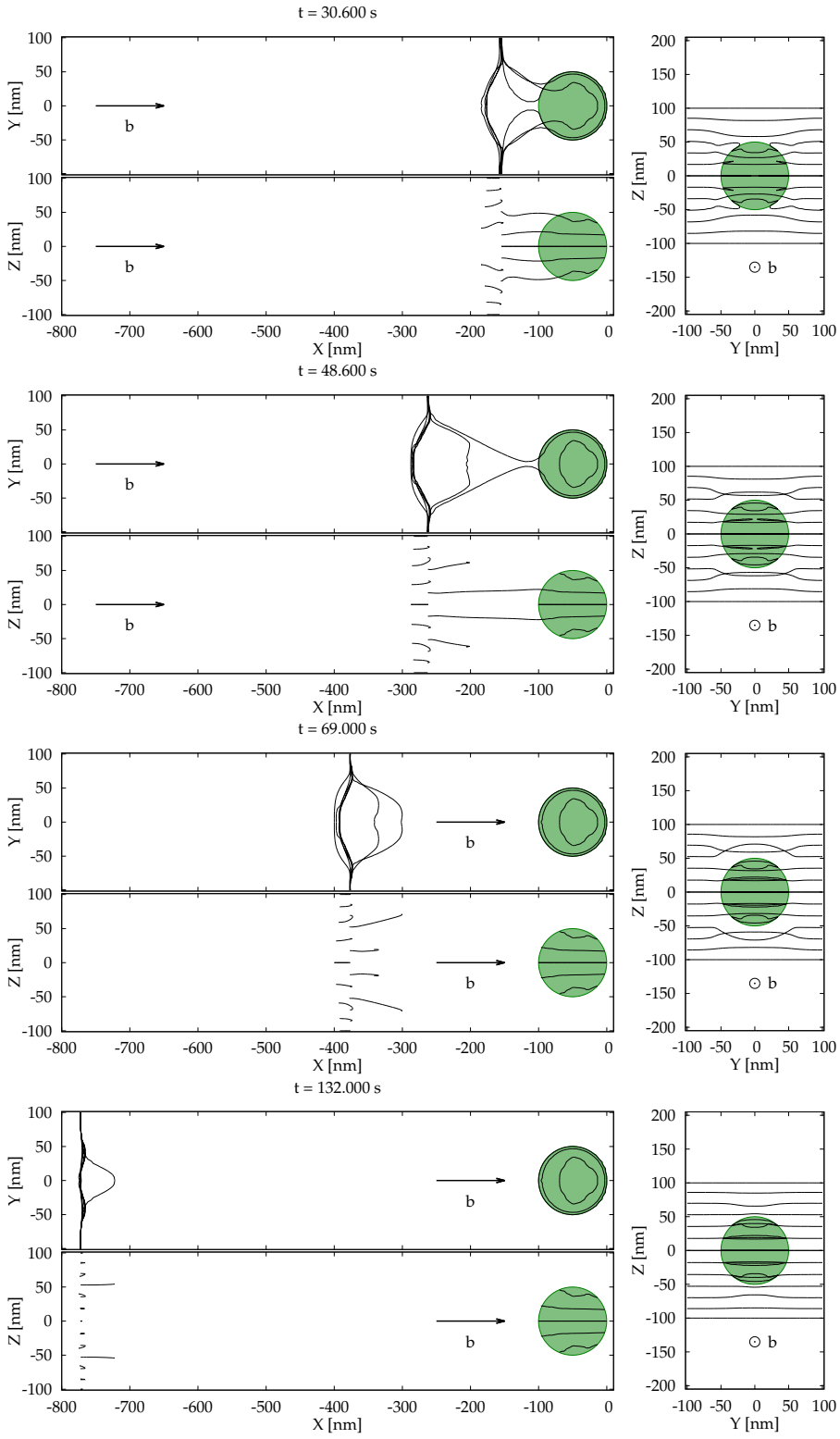

Figure VII.11: An evolution of the low-angle tilt boundary with $h = 16.\overline{6}\,\text{nm}$, $\sigma_{xz} = 80\,\text{MPa}$ and $d = 100\,\text{nm}$.

the precipitate diameter d and the critical stress is determined by the relation (I.9), which is recalled here:

$$\sigma_{\text{Orowan}} = \Gamma \frac{\mu b}{\lambda - d}.$$

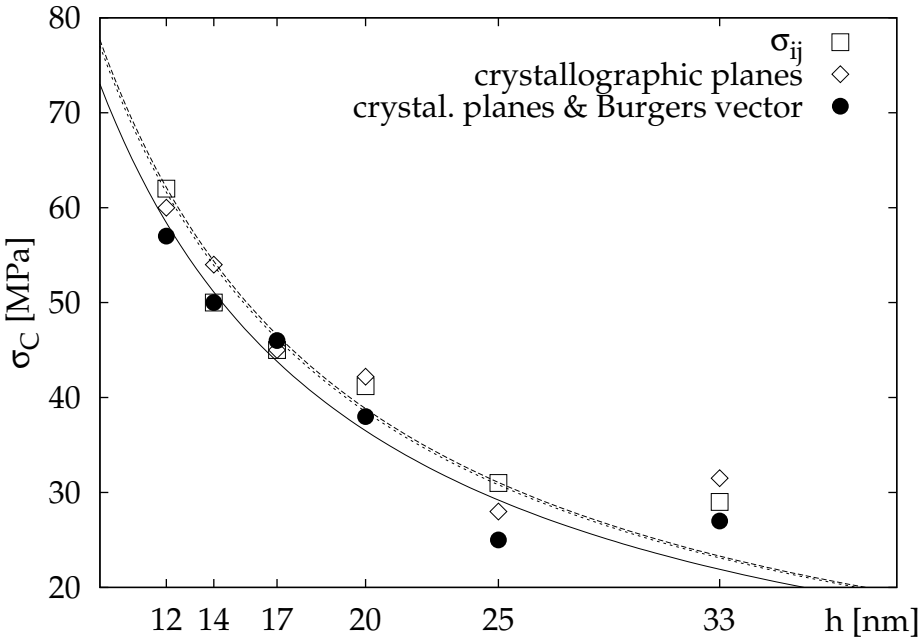

Figure VII.12: Comparison between critical stresses computed using the force decomposition according to crystallographic slip planes and the components of the Burgers vector (solid line) and the two former methods (dashed lines). The precipitate diameter is $d = 100$ nm.

Table VII.3: The Γ factor for different initial dislocation line spacings h.

h [nm]	Γ	$\rho(\Gamma)$
$33.\overline{3}$	0.13 ± 0.02	17 %
25.0	0.17 ± 0.03	15 %
20.0	0.21 ± 0.02	12 %
$16.\overline{6}$	0.25 ± 0.03	13 %
14.3	0.28 ± 0.04	15 %
12.5	0.31 ± 0.04	13 %

The Orowan stress for $\Gamma = 0.8$ (this value is fitted from experimental results, see [28]) is plotted together with the critical stresses σ_C in Fig. VII.15. The plot shows that the critical stresses obtained from the simulations are significantly lower than the Orowan stress. This agrees with experimental results from compression tests by Hausselt and Nix [4]. The results obtained from the simulation have been fitted with the least-squares method using the relation (I.9) with Γ as the fit parameter. The values of the Γ parameter for different initial line spacings h are listed in Table VII.3. These fits are displayed with solid lines in Fig. VII.16. However, the Orowan-type relation (I.9) does not well approximate the dependence of the critical stress σ_C on the particle diameter d. For higher dislocation densities, the critical stress grows almost linearly with the precipitate diameter (see e.g. the points for $h = 12.5$ nm plotted in Fig. VII.16).

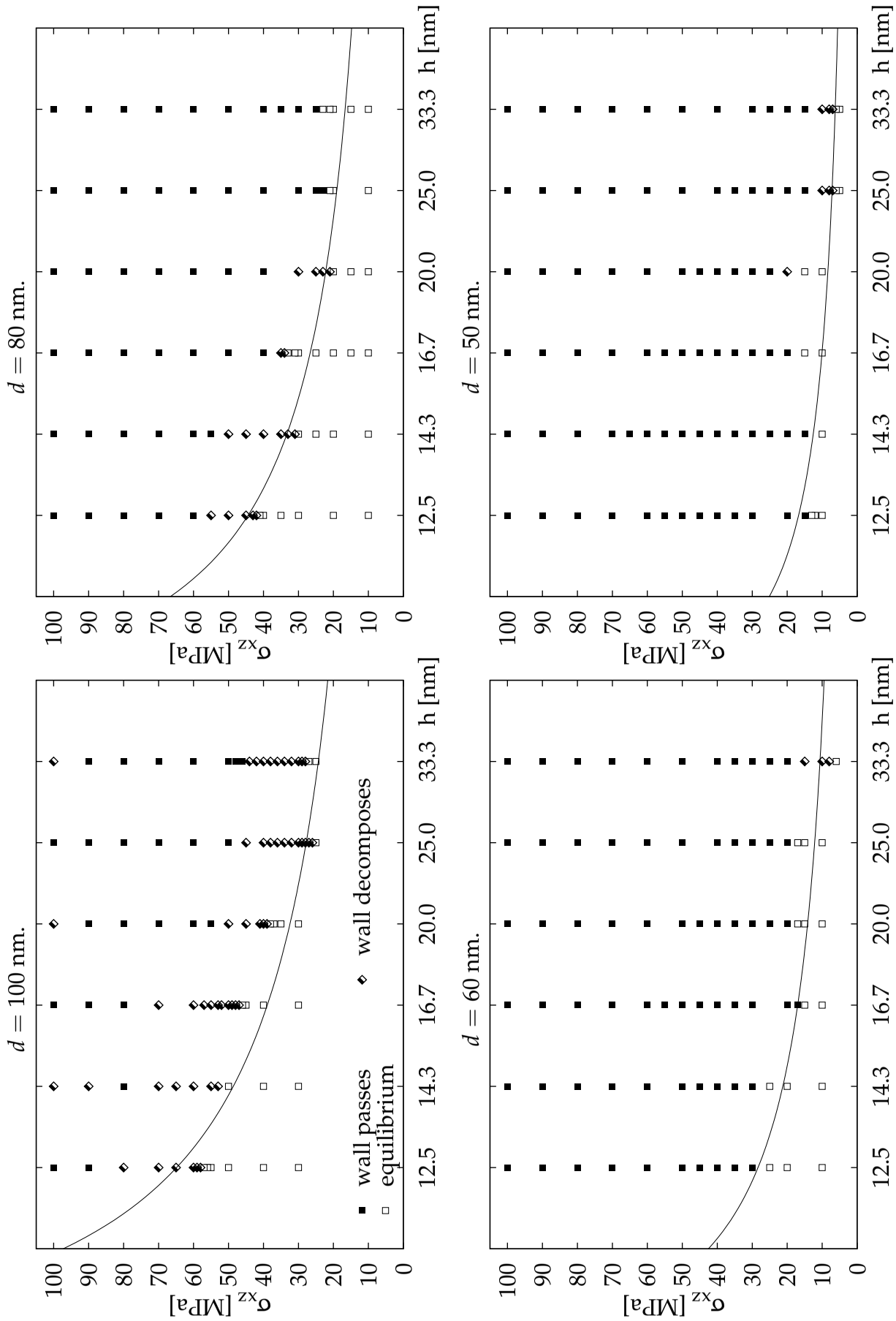

Figure VII.13: Regimes of LADB – force decomposition according to crystallographic planes and the components of the Burgers vector. Particle diameters $d \in \{50, 60, 80, 100, 120\}$ nm.

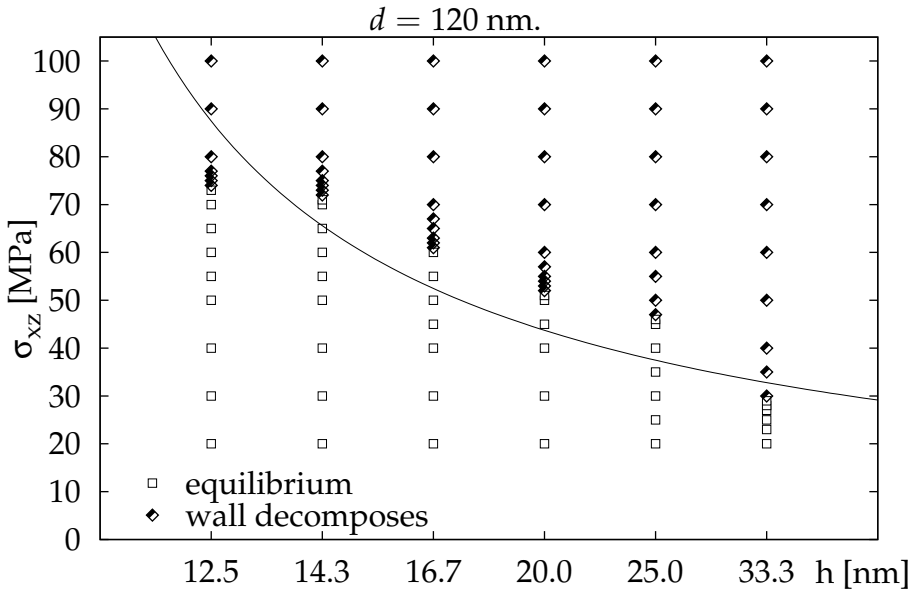

Figure VII.13 cont.: Regimes of LADB – force decomposition according to crystallographic planes and the components of the Burgers vector. Particle diameters $d \in \{50, 60, 80, 100, 120\}$ nm.

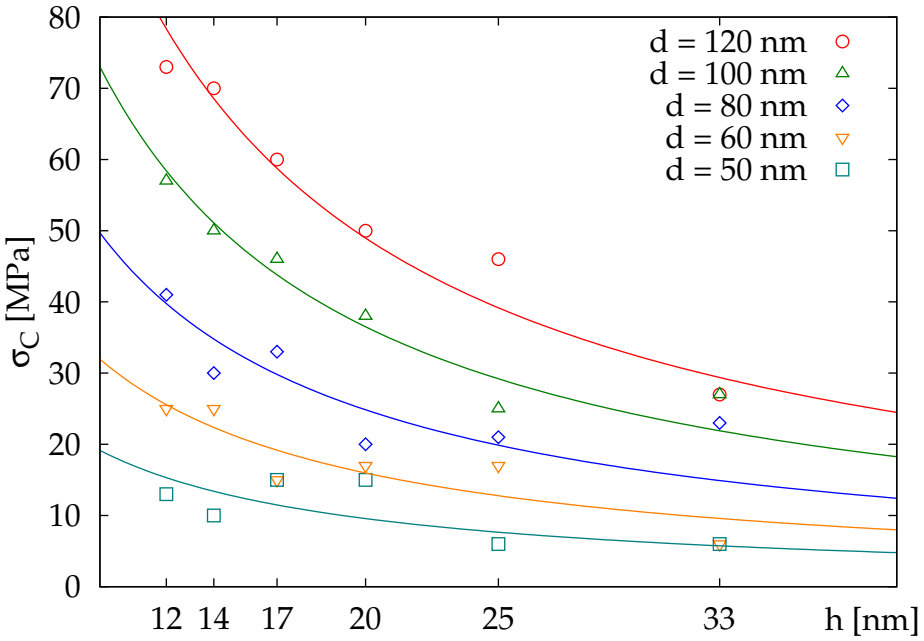

Figure VII.14: Critical stresses for different precipitate diameters.

VII.2.4 Calculation of strain rates

The simulations based on the force decomposition according to crystallography and the components of the Burgers vector were analyzed in order to compute strain rates associated with the LADB migration. The technique used for the strain rate calculations is described in the section IV.7. The preliminary data presented here were obtained only for one diameter of the precipitates $d = 100$ nm. As an example, a time evolution of strain rates for a system with initial dislocation line spacing $h = 16.\overline{6}$ nm is presented in Fig. VII.17.

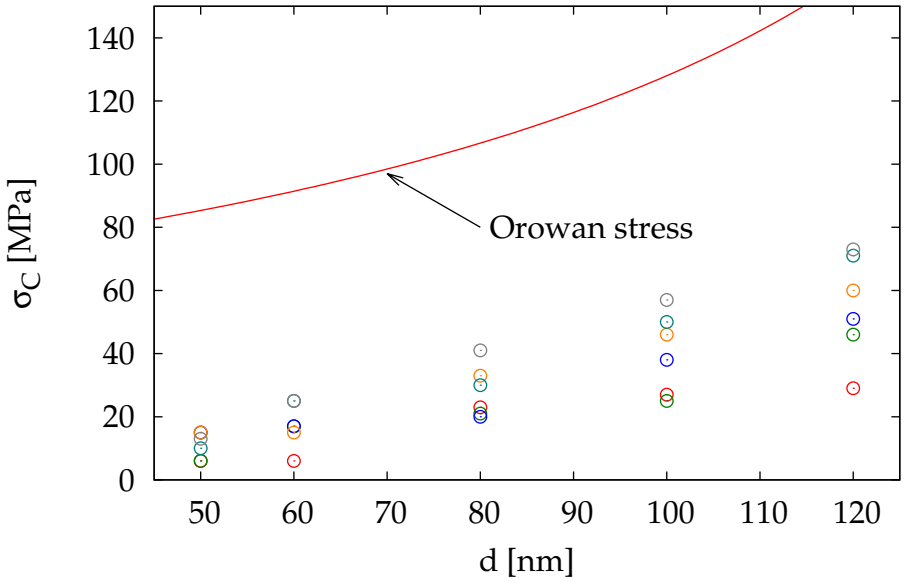

Figure VII.15: Comparison of critical stresses σ_C and the Orowan stress for $\Gamma = 0.8$.

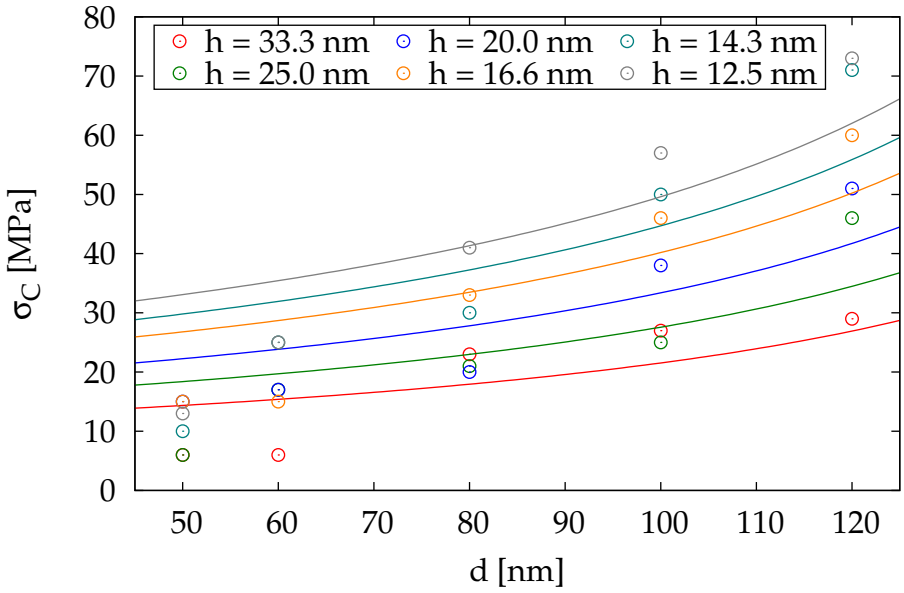

Figure VII.16: Critical stresses for various precipitate diameters d and line spacings h.

The curves shown in Fig. VII.17 indicate that the dislocations initially move with a velocity proportional to the applied stress, until they encounter spherical precipitates. Depending on the magnitude of the applied stress and the dislocation spacing, the dislocation system may or may not overcome the precipitates. For applied stresses below the critical stress, the strain rate approaches zero. For applied stresses above σ_C, the dislocation lines leave loops on the precipitate surfaces and continue their migration through the crystal. Depending on the complex interactions between individual dislocation lines, dislocation kinks may form on some of the lines (see snapshots in Fig. VII.11 for $h = 16.\overline{6}\,\text{nm}$ and $\sigma_{xz} = 80\,\text{MPa}$), which greatly reduces the velocity of the whole dislocation boundary. These structures are unstable, however, they can remain

in the system for thousands of integration steps, even for the rest of the simulation. If the dislocation kinks disappear, a sudden increase of the dislocation velocity is observed, which leads to a significant increase of the strain rate to the original level (see Fig. VII.17).

The strain rates evaluated from the DDD simulation can be analyzed with respect to the magnitude of the externally applied stress. For this purpose, minimum strain rates $\dot{\varepsilon}_{\mathrm{min}}$ observed in the individual simulations are plotted as a function of the applied stress. The corresponding stress exponent n was evaluated, see equation (I.3). Unless the applied stress is below the critical stress σ_{C}, the minimum value of $\mathrm{d}\varepsilon/\mathrm{d}t$ is nonzero and is observed shortly after the onset of the DDD simulation, when the dislocation boundary comes into contact with the spherical precipitates. Taking the logarithm of the relation (I.3) gives

$$\log \dot{\varepsilon}_{\mathrm{min}} = \log B(T) + n \log \sigma. \tag{VII.7}$$

Thus, in a bilogarithmic plot of the minimum strain rate $\dot{\varepsilon}_{\mathrm{min}}$ vs. applied stress σ, the stress exponent n determines the slope of a straight line.

The plots in Fig. VII.18 show that the stress exponent n changes with decreasing applied stress. If the applied shear stress is far above σ_{C}, the precipitates are quickly surpassed by the dislocation boundary. In this case, the minimum strain rate is not sensitive to changes in the applied stress and the stress exponent has the order in a range $n \in (1, 3)$. In this stress range, the stress exponent approaches a value $n = 1$ typical for diffusion creep in pure metals (section I.1.3 and [1]). On the other hand, for low values of the applied shear stress, the dislocation boundary moves slowly and the dislocation velocity changes rapidly with the shear stress. The stress exponent changes rapidly as the shear stress approaches σ_{C}. Some of the stress exponents are indicated in Fig. VII.18, like $n \approx 17$ for the LADB with the initial line spacing $h = 12.5\,\mathrm{nm}$. This result is in a good agreement with experimental data obtained by Hausselt and Nix [4]. In their work, they observed a threshold stress type behaviour with n as large as 40 for a dispersion strengthened NiCr alloy just above the critical stress.

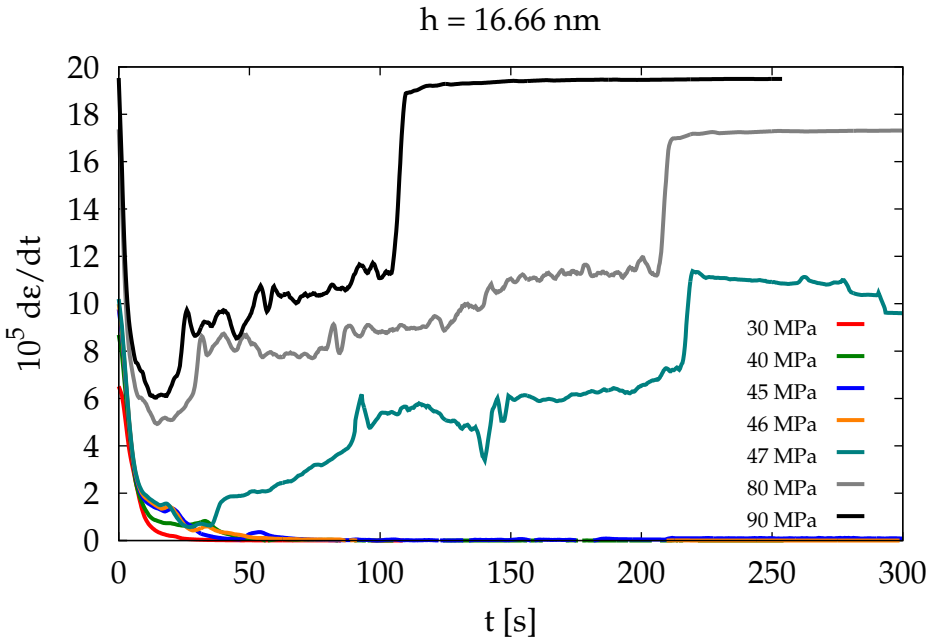

Figure VII.17: Strain rates due to migration of a LADB with initial dislocation line spacing $h = 16.\overline{6}$ nm. Precipitate diameter is $d = 100$ nm.

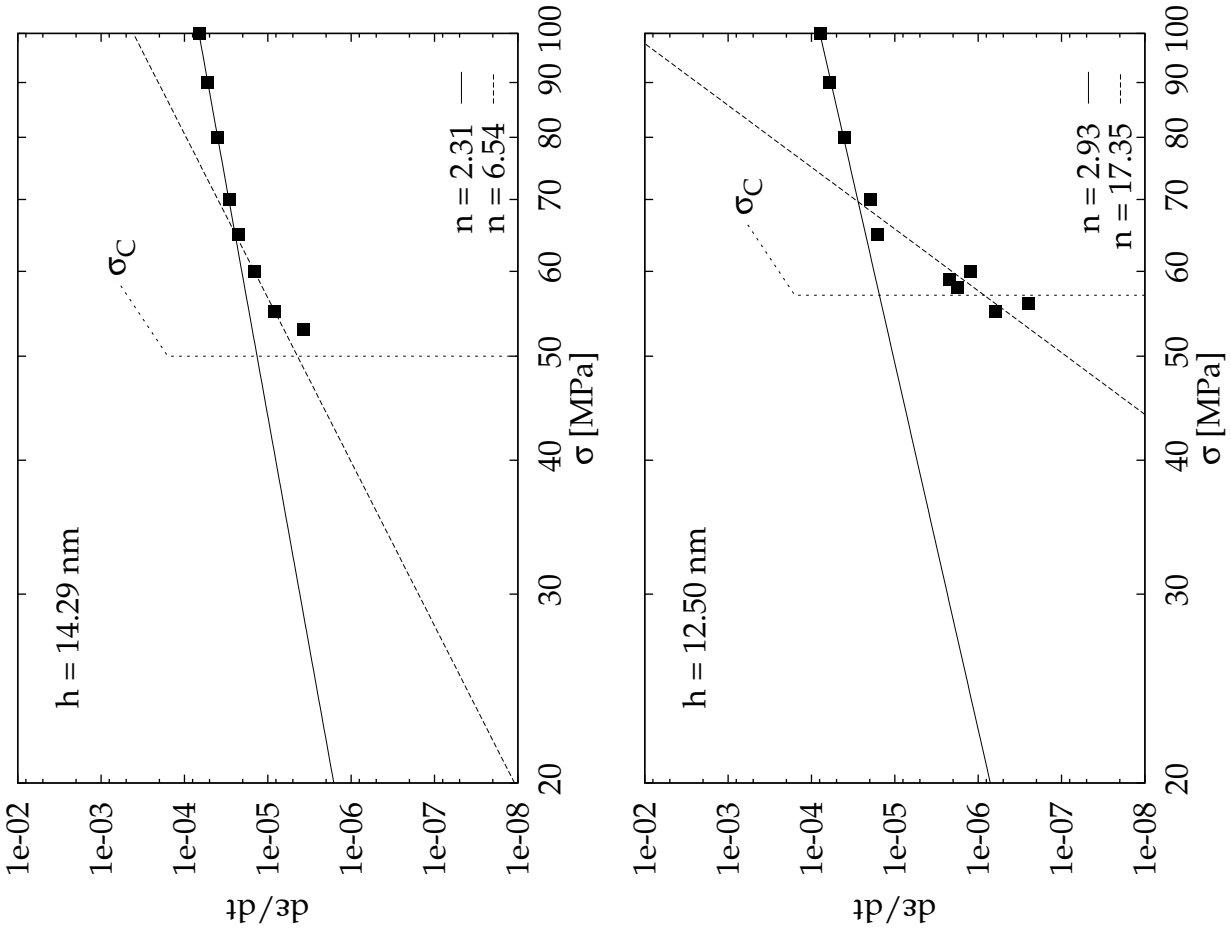

Figure VII.18: Minimum strain rates for precipitate diameter $d = 100$ nm and dislocation line spacings $h \in \{14.3, 12.5\}$ nm.

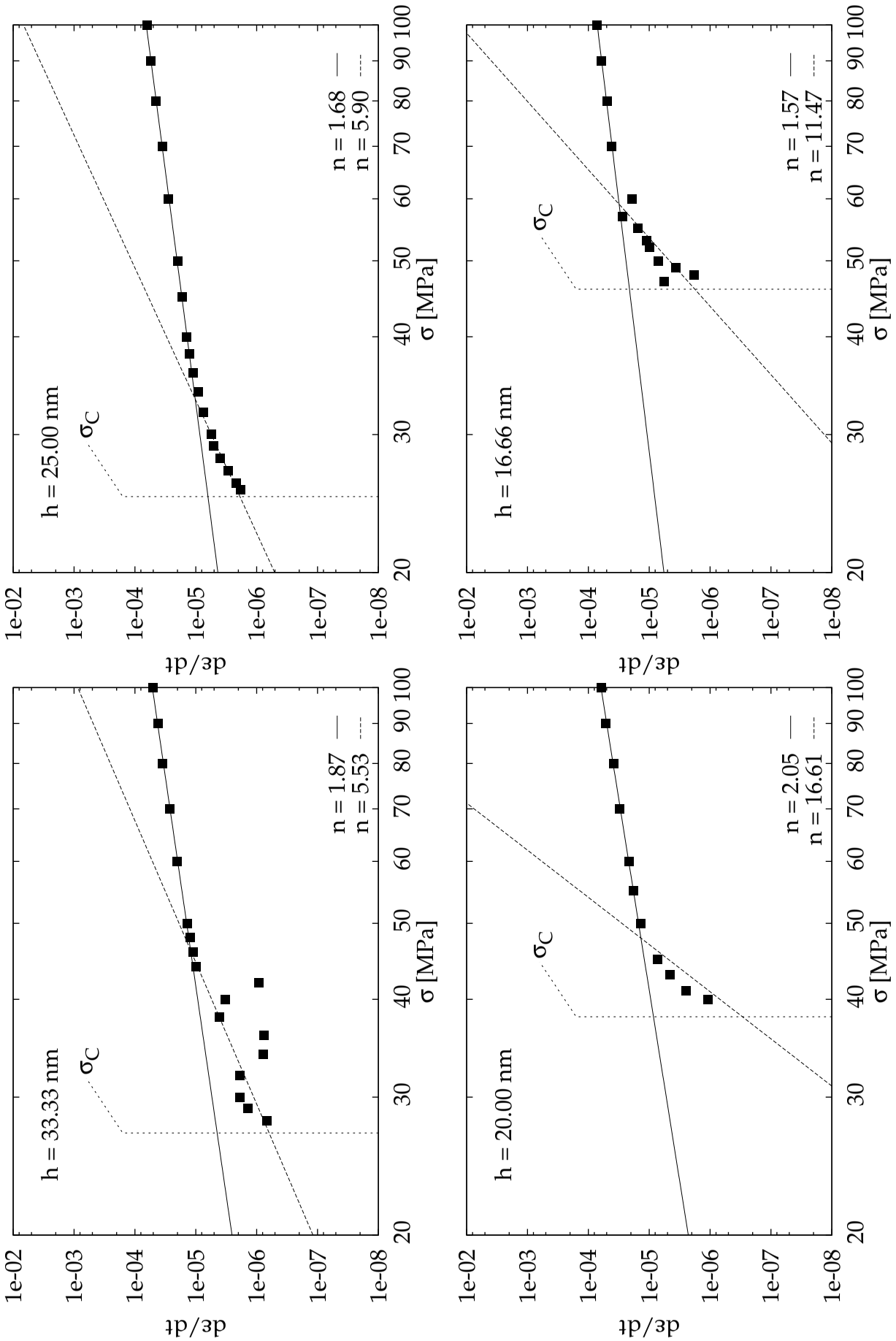

Figure VII.18 cont.: Minimum strain rates for precipitate diameter $d = 100\,\text{nm}$ and dislocation line spacings $h \in \{33.\overline{3}, 25, 20, 16.\overline{6}\}$ nm.

VIII. Summary and conclusions

VIII.1 The 3D DDD model

This work focuses on a design of a 3D discrete dislocation dynamics (DDD) model applicable to study of plastic deformation in a temperature regime where a contribution due to diffusion cannot be neglected. A numerical implementation of the model represents a considerable part of this work.

The Chapter I introduces a brief review of high temperature deformation processes and their microstructural background. The connection between the plastic deformation and crystal defects is summarized, with emphasis on the importance of dislocations. The state-of-art 2D and 3D DDD methods are briefly reviewed.

The Chapter III summarizes necessary knowledge from the theory of elasticity. This is the fundament of the theory of dislocations discussed in the Chapter IV. The potential of the model is demonstrated in Chapters V, VI and VII, particularly, its application on a system of infinite parallel dislocations forming a dislocation boundary is elaborated in detail.

VIII.2 Benchmark simulations

The model is introduced in Chapter V. It is tested and demonstrated on benchmark dislocation systems. The very first is a single dislocation loop contracting due to its self-stress. This simple dislocation configuration is used to study influences of the time integration step, discretisation and remeshing of the dislocation structure. There is also a parametric study of the dependence of the driving forces on the discretisation and on the initial radius of the dislocation loop. The dislocation loop is used also for the first simulations with rigid spherical precipitates. The second system is a Frank-Read dislocation source, which produces new dislocation loops under the application of shear stress.

The more complex benchmarks involved two or more dislocation loops at a presence of spherical precipitates. These configurations were studied both with and without an externally applied stress. The corresponding simulations revealed a complicated behaviour, especially when the dislocation structure evolved under the action of the externally applied stress. The complexity of the system also resulted in the introduction of several optimizations of the model, which allow to address the physical symmetry. This significantly increased the performance of the numerical implementation of the model. These benchmarks are described in Chapter VI. The dislocation annihilation and the symmetry optimizations are still a subject of the same chapter.

VIII.3 Low angle tilt boundary

The model has been used to study a behaviour of a low-angle tilt boundaries subjected to an applied shear stress at high temperatures (Chapter VII). The dislocation system consisted of initially equidistant edge dislocations of an infinite length. To represent such a large-scale structure, an approximation based on periodic boundary conditions has been adopted, effectively replacing an infinite system with an elementary simulation cell. The single simulation cell is replicated using a translational symmetry (section VI.9), which transforms the simulation cell into the large-scale structure. The simulation cell is initially set up with a symmetric structure of dislocations and precipitates, which is also considered in the model (section VI.6).

The evolution of the dislocation boundary is studied using three different approaches that treat differently a relation between the driving forces and the dislocation velocity (section VI.2). Depending on the initial dislocation line spacing h, the diameter of the precipitates d and the magnitude of the applied shear stress σ_{xz}, the dislocation boundary may reach an equilibrium state, when it is held back by the precipitates, which thus strengthen the material. An important fact is that even the dislocations, which are not in contact with the precipitates, are in this range of applied stresses prevented from further motion (see a force plot in Fig. VII.4). Low-angle tilt boundaries attract dislocations near the equilibrium position into the wall, see section IV.6.

Otherwise, if the applied stress is higher than critical stress $\sigma_C(h, d)$, the dislocation boundary may pass between the precipitates and leave dislocation loops on their surfaces. The results show that the value of the critical stress σ_C does not depend much on the selected equations of motion. On the other hand, the behaviour of the dislocation boundary after the passing through the precipitate field is strongly dependent on the kinetic relation between a segment velocity and the driving force. For higher initial distances h between the dislocations, which correspond to smaller misorientation angles between two neighbour subgrains, the interactions between the individual dislocations are not strong enough to hold all of the dislocations in the boundary, which thus may decompose into two or more even less dense boundaries. A subgrain boundary may be even completely eliminated by this process and only individual dislocations remain.

The existence of certain threshold stresses has been reported from creep experiments [4]. Threshold stresses between 20 and 60 MPa (Chapter VII) correspond to misorientation angles from 0.3° to 0.9°. This well agrees with misorientation angles observed by TEM after high temperature deformation [56–58].

The dependence of $\sigma_C(h, d)$ on the particle diameter d for $h = \text{const.}$ has been also studied. The results have been compared with theoretically predicted Orowan stress (section I.3 and [28]), which is inversely proportional to the distance between the precipitate surfaces, i.e. $\lambda - d$. The results show that the critical stress σ_C obtained from the DDD simulations is far below the Orowan stress. The same observation is known from creep experiments with dispersion strengthened alloys [4]. Furthermore, the Orowan stress is not a good approximation of the critical stress σ_C obtained from the DDD simulations.

The dislocation displacement is connected with strain (section IV.7). Thus the dislocation velocity has been used to calculate the strain rate. The recorded data have been used to calculate the stress exponent n from the dependence of the minimum strain rate on the applied stress. The results show that the stress exponent is low for applied stresses much higher than the critical stress. In this stress range n approaches

1. On the other hand, the stress exponent is very high for stresses just above the critical stress, which corresponds to experimental results obtained for dispersion strengthened alloys [4].

VIII.4 Final summary

This work presents a 3D discrete dislocation dynamics (DDD) model, which is based on the linear theory of elasticity. The model demonstrates its potential in studies of motion of dislocations at high temperatures subjected to both the internal stress of the dislocation structure and an externally applied stress. The model addresses also an interaction between the dislocation lines and rigid spherical precipitates, as well as the annihilation of dislocations. At first, the model is applied to benchmark systems, such as a single dislocation loop contracting due to its self-stress and a Frank-Read dislocation source. The loop simulations were carried out also with a presence of spherical precipitates. Secondly, the model was used to study a behaviour of a set of two or more coaxial dislocation loops in a field of spherical precipitates, at first for a case when no external stress was applied. In the second case, a shear stress was applied to make the loops expand in the precipitate field. This more complex benchmark brought a need to address the symmetry of the simulated structure to improve the overall performance of the model. Finally, the model was applied to a moving low-angle tilt boundary interacting with equidistant spherical precipitates. This situation was studied for different applied shear stresses, misorientation angles (i.e. dislocation spacing) of the tilt boundaries and also for various diameters of the precipitates. The results of the 3D DDD simulations are: 1) an existence of a critical stress, under which the motion of the tilt boundary is stopped by the spherical precipitates, 2) a dependence of the critical stress on the dislocation spacing and the precipitate diameter, 3) an evolution of the strain rate during the creep process. The model prediction of the critical stress which is considerable lower than the theoretically calculated Orowan stress is in agreement with known experimental results. Also the stress exponents calculated from the minimum strain rate are in agreement with the experimental findings.

BIBLIOGRAPHY

[1] Čadek, J. *Creep kovových materiálů*. Academia, Praha (1984).

[2] Kassner, M. E., Pérez-Prado M.-T. *Fundamentals of Creep in Metals and Alloys.* Elsevier, Amsterdam (2004).

[3] Hausselt, J. H., Nix, W. D. Dislocation structure of Ni-20Cr-2ThO_2 after high-temperatore deformation. *Acta Metall.* **25** (1977) 595–607.

[4] Hausselt, J. H., Nix, W. D. A model for high temperature deformation of dispersion strenghtened metals based on substructural observations in Ni-20Cr-2ThO_2. *Acta Metall.* **25** (1977) 1491–1502.

[5] Čadek, J., Šustek, V., Pahutová, M. An analysis of a set of creep data for a 9Cr-1Mo-0.2V (P91 type) steel. *Mater. Sci. Eng. A* **225** (1997) 22–28.

[6] Hirth, P., Lothe, J. *Theory of dislocations*. 2nd edition, Krieger Publishing Company, Malabar (1992).

[7] Brdička, M., Samek, L., Sopko, B. *Mechanika kontinua*. 2. opravené vydání, Academia, Praha (2000).

[8] Landau, L. D., Lifšic, E. M. *Teorija uprugosti*. izdanie 4, Nauka, Moskva (1987).

[9] Seeger, A., Diehl, J., Mader, S., Rebstock, H. Work-hardeing and work-softening of face-centered cubic metal crystals. *Phil. Mag.* **2** (1957) 323–350.

[10] Saxl, I., Kroupa, F. Relations between experimental parameters describing steady-state and transient creep. *Phys. stat. sol. (a)* **11** (1972) 167–173.

[11] Kratochvíl, P., Lukáč, P., Sprušil, B. *Úvod do fyziky kovů I*. SNTL/ALFA, Praha (1984).

[12] Schoeck, G. Activation energy of dislocation movement. *Phys. stat. sol.* **8** (1965) 499–507.

[13] Hirth, J. P., Nix, W. D. Analysis of the thermodynamics of dislocation glide. *Phys. stat. sol.* **35** (1969) 177–188.

[14] Kocks, U. F., Argon, A. S., Ashby, M. F. Thermodynamics and Kinetics of Slip. *Progress in Materials Science* **19** (1975) 1–281.

[15] Nabarro, F. R. N. (ed.) *Dislocations in Solids*. North-Holland, Amsterdam (1980).

[16] Peierls, R. E. The size of a dislocation. *Proc. Phys. Soc.* **52** (1940) 34–37.

[17] Vítek, V. Intrinsic stacking faults in body-centered cubic crystals. *Phil. Mag.* **18** (1968) 773–786.

[18] Caillard, D., Martin, J. L. Thermally Activated Mechanisms in Crystal Plasticity. In: *Pergamon Materials Series*. Ed.: R. W. Cahn, Pergamon, Amsterdam (2003).

[19] Cottrell, A. H., Jaswon, M. A. *Distribution of solute atoms round a slow dislocation. Proc. Roy. Soc. A* **199** (1949) 104–114.

[20] Haasen, P. In: *Dislocations in Solids*. vol. 4, chapt. 15, Ed.: F. R. N. Nabarro, North-Holland (1979).

[21] Norton, F. H. *The creep of steel at high temperatures.* McGraw-Hill Book Company, New York (1929).

[22] Cannon, W. R., Sherby, O. D. *Metallurgical and materials transactions B*. **1** 4 (1970) 1030–1032.

[23] Píšek, F., Jeníček, L., Ryš, P. *Nauka o materiálu I - Nauka o kovech, 1. svazek*. 2. rozšířené vydání, Academia, Praha (1966).

[24] Blum, W. In: H. Mughrabi (Ed.), *Materials Science and Technology, Vol. 6*: Plastic Deformation and Fracture of Materials, VCH Verlagsgesellschaft, Weinheim (1993) 359.

[25] Exell, S. F., Warrington, D. H. Sub-grain boundary migration in aluminium. *Phil. Mag.* **26** (1972) 1121–1136.

[26] Lagneborg R. Bypassing of dislocations past particles by a climb mechanism. *Scripta Metall.* **7** (1973) 605–613.

[27] Brown, L. M., Ham, R. K. In: A. Kelly, R. B. Nicholson (Eds.), *Strengthening Methods in Crystals*. Applied Science Publishers Ltd., London (1971) 9.

[28] Repich, B. In: H. Mughrabi (Ed.), *Materials Science and Technology, Vol. 6*: Plastic Deformation and Fracture of Materials, VCH Verlagsgesellschaft, Weinheim (1993) 311.

[29] Holt, D. L. Dislocation cell formation in metals. *J. Appl. Phys.* **41** (1970) 3197–3201.

[30] Weygand, D., Friedman, L. H., van der Giessen, E., Needleman, A. Discrete dislocation modelling in three-dimensional confined volumes. *Mater. Sci. Eng. A* **309-310** (2001) 420–424.

[31] Devincre, B., Kubin, L., Hoc, T. Physical analyses of crystal plasticity by DD simulations. *Scripta Mat.* **54** (2006) 741–746.

[32] Liu, B., Raabe, D., Eisenlohr, P., Roters, F., Arsenlis, A., Hommes, G. Dislocation interactions and low-angle grain boundary strengthtening. *Acta Mat.* **59** (2011) 7125–7134.

[33] Verdier, M., Fivel, M., Groma, I. Mesoscopic scale simulation of dislocation dynamics in fcc metals: Principles and applications. *Model. Simul. Mater. Sci. Eng.* **6** (1998) 755–770.

[34] Schwarz, K. W. Simulation of dislocations on the mesoscopic scale. I. Methods and examples. *J. Appl. Phys.* **85** (1999) 108–119.

[35] Faradjian, A. K., Friedman, L. H., Chrzan, D. C. Frank-Read sources withing a continuum simulation. *Model. Simul. Mater. Sci. Eng.* **7** (1999) 479–494.

[36] Schwarz, K. W. Local rules for approximating strong dislocation interactions in discrete dislocation dynamics. *Model. Simul. Mater. Sci. Eng.* **11** (2003) 609–625.

[37] Monnet, G., Devincre, B., Kubin, L. P. Dislocation study of prismatic slip systems and their interactions in hexagonal close packet metals: application to zirconium. *Acta Mat.* **52** (2004) 4317–4328.

[38] Tang, M., Cai, W., Guanshui, X., Bulatov, V. V. A hybrid method for computing forces on curved dislocations intersecting free surfaces in three-dimensional dislocation dynamics. *Model. Simul. Mater. Sci. Eng.* **14** (2006) 1139–1151.

[39] Arsenlis, A., Cai., W., Tang, M., Rhee, M., Oppelstrup, T., Hommes, G., Pierce, T. G., Bulatov, V. V. Enabling strain hardening simulations with dislocation dynamics. *Model. Simul. Mater. Sci. Eng.* **15** (2007) 553–595.

[40] Bako, B., Weygand, D., Samaras, M., Chen, J., Pouchon, M. A., Gumbsch, P., Hoffelner, W. Discrete dislocation dynamics simulations of dislocation interactions with Y_2O_3 particles in PM2000 single crystals. *Phil. Mag.* **87** (2007) 3645–3656.

[41] Motz, C., Weygand, D., Senger, J., Gumbsch, P. Initial dislocation structures in 3-D discrete dislocation dynamics and their influence on microscale plasticity. *Acta Mater.* **57** (2009) 1744–1754.

[42] Vattré, A., Devincre, B., Roos, A. Dislocation dynamics simulations of precipitation hardening in Ni-based superalloys with high γ' volume fraction. *Intermetallics* **17** (2009) 998–994.

[43] Holec, D. *Pohyb dislokačních hranic v precipitačně zpevněných systémech.* Bakalářská práce. Masarykova unverzita. Brno (2003).

[44] Holec, D., Dlouhý, A. Interactions between particles and low-angle dislocation boundaries during high-temperature deformation. *Z. Metallkd.* **96** (2005) 558–565.

[45] Bulatov, V. V., Cai, W. *Computer Simulations of Dislocations*. Oxford University Press (2006).

[46] Devincre, B., Condat, M. Model validation of a 3D simulation of dislocation dynamics: discretization and line tension effects. *Acta metall. mater.* **40** (1992), 2629–2637.

[47] Devincre, B., Kubin, L. P. Mesoscopic simulations of dislocations and plasticity. *Mater. Sci. Eng. A* **234–236** (1997) 8–14.

[48] Devincre, B., Kubin, L. P., Lemarchang, C., Madec, R. Mesoscopic simulations of plastic deformation. *Materials Science and Engineering A* **309-310** (2001) 211–219.

[49] Ghoniem, N. M., Sun, L. Z. Fast-sum method for the elastic field of three-dimensional dislocation ensembles. *Physical Review B* **60** (1999) 128–140.

[50] Ghoniem, N. M., Tong, S. H., Sun, L. Z. Parametric dislocation dynamics: A thermodynamics-based approach to investigations of mesoscopic plastic deformation. *Physical Review B* **61** (2000) 913–927.

[51] Mordehai, D., Clouet, E., Fivel, M., Verdier, M. Introducing dislocation climb by bulk diffusion in discrete dislocation dynamics. *Phil. Mag.* **88** (2008) 899–925.

[52] Allnatt, A. R., Lidiard, A. B. *Atomic transport in solids*. Cambridge University Press (2003).

[53] Cai, W., Arsenlis, A., Weinberger, Ch.R., Bulatov, V. V. A non-singular continuum theory of dislocations. *Journal of the Mechanics and Physics of Solids* **54** (2006) 561–587.

[54] Hliněný, P. *Diskrétní matematika, skripta VŠB TU*. Ostrava (2006).

[55] Horová, I., Zelinka, J. *Numerické metody, 2. rozšírené vydání*. Masarykova univerzita. Brno (2004).

[56] Dronhofer, A., Pešička, J, Dlouhý, A., Eggeler, G. On the nature of internal interfaces in tempered martensite ferritic steels. *Z. Metallkd.* **94** (2003) 511–520.

[57] Sauzay, M., Brillet, H., Monnet, I., Mottot, M., Barcelo, F., Fournier, B., Pineau, A. Cyclically induced softening due to low-angle boundary annihilation in a martensitic steel. *Mater. Sci. Eng. A* **400–401** (2005) 241–244.

[58] Sauzay, M. Modelling of the evolution of micro-grain misorientations during creep of tempered martensite ferritic steels. *Mater. Sci. Eng. A* **510–511** (2009) 74–80.